Investigation of Al thermal diffusion in SixGe1-x alloy nanowires using in-situ transmission electron microscopy

Minh Anh Luong

Communauté
UNIVERSITÉ Grenoble Alpes

THÈSE

Pour obtenir le grade de
DOCTEUR DE LA COMMUNAUTÉ UNIVERSITÉ GRENOBLE ALPES
Spécialité : **NANOPHYSIQUE**
Arrêté ministériel : 25 mai 2016

Présentée par

Minh Anh LUONG

Thèse dirigée par **Eric ROBIN** et **Martien den HERTOG**

préparée au sein du **CEA/IRIG/DEPHY/MEM/LEMMA et Institut Neel CNRS**
dans **l'École Doctorale Physique**

Etude de la diffusion thermique de l'Aluminium dans des nanofils de Germanium et en alliages de Si_xGe_{1-x} en utilisant la microscopie électronique en transmission in situ

Investigation of Al thermal diffusion in Ge and Si_xGe_{1-x} alloy nanowires using in-situ transmission electron microscopy

Thèse soutenue publiquement le **5 Novembre 2019**,
devant le jury composé de :

M. Gilles PATRIARCHE
Directeur de Recherche CNRS ÎIe-de-France Gif-sur-Yvette, Rapporteur
M. Dinh Phong TRAN
Professeur Assistant USTH – Vietnam, Rapporteur
Mme Catherine BOUGEROL
Directrice de Recherche CNRS Delegation Alpes**,** Président
M. Alois LUGSTEIN
Professeur Associé Universite Technique de Vienne Autriche, Examinateur

To my parents,

Acknowledgements

Before going through all the stressful, but passionated scientific works, I would like to express my gratitude to all the people who have been consistently supporting me out throughout three years of my PhD. First and foremost, I would like to specially thank my two amazing supervisors, Dr. Martien den Hertog and Dr. Eric Robin for your expertise and continuous support. Dr. Martien, discussing with you always bring me lots of motivation and encouragement. Your pedagogical way of teaching and limitless patience helps me a lot in tackling problems and inspiring me in learning new subjects. Dr. Eric, thank you for spending your valuable time teaching me how to use the microscopes, for all the knowledge and your daily support. On a more personal note, my wife and I appreciate very much your lovely gifts for our marriage.

Besides, I would like to send my sincere respect to all the members in CEA/IRIG-DEPHY/MEM/LEMMA lab: Dr. Nicolas, Laure, Jean-Luc and Hanako for your technical helps and giving me a friendly working atmosphere. Sincere thanks to all my colleagues in CEA Minatec: Carlos, Dipankar, Andrea, Ahmed, Praveen and Zahra for daily funny jokes and constructive conversations in research experiences. Without you guys, I could never have many wonderful memories in Grenoble city. Additionally, I would like to thank LANEF funding, for give me a chance to come to France, immerse in a professional scientific work and start my future.

Finally, I would like to thank my family, my wife and all my lovely non-physicist friends for always sticking up with me, giving me daily inspiration and energy to finish this work.

Minh Anh

Abbreviations and Symbols

List of Abbreviations

Abbreviation	Full Meaning
NWs	*Nanowires*
1D	*One Dimensional*
ALD	*Atomic Layer Deposition*
CVD	*Chemical Vapour Deposition*
VLS	*Vapor–Liquid–Solid*
VSS	*Vapor–Solid- Solid*
TA	*Template-Assisted*
EBL	*Electron Beam Lithography*
QCM	*Quartz Crystal Microbalance*
CMOS	*Complementary Metal Oxide Semiconductor*
FETs	*Field Effect Transistors*
LEDs	*Light-Emitting Diodes*
HF	*Hydroflouric Acid*
HI	*Hydroiodic Acid*
PMMA	*Poly(methyl methacrylate)*
MIBK	*Methyl Isobutyl Ketone*
IPO	*Isopropanol*
BOE	*Buffered Oxide Etch*
DIW	*Deionized Water*
Al_2O_3	*Aluminium oxide*
Si_3N_4	*Silicon nitride*
LaB_6	*Lanthanum hexaboride*
W	*Tungsten*
TMA	*Al(CH3)3 [Trimethylaluminum]*
TEM	*Transmission Electron Microscopy*
STEM	*Scanning Transmission Electron Microscopy*
HAADF	*High-Angle Annular Dark-Field*
HRTEM	*High Resolution Transmission Electron Microscopy*
FT	*Fourier Transformation*
DP	*Diffraction Pattern*
SEM	*Scanning Electron Microscope*
EDX	*Energy-Dispersive X-Ray Spectroscopy*

EELS	*Electron Energy Loss Spectroscopy*
RTA	*Rapid Thermal Annealing*
SDD	*Silicon Drift Detectors*
TMP	*Turbo Molecular Pump*
RP	*Rotary Pump*
QCM	*Quartz Crystal Microbalance*
TLM	*Transfer Length Measurement*
CB	*Conduction Band*
CV	*Valance Band*

List of Symbols

Symbol	Full Meaning
Å	*Angstrom*
eV	*Electron Volt*
nm	*Nanometer*
s	*Second*
E_g	*Bandgap Energy*

Table of Contents

Chapter 1

Introduction

This PhD is about transmission electron microscopy using in-situ observation of a thermally induced reaction between a metal and a semiconducting nanowire. Before going to the objectives of the PhD thesis, we would like to present a brief history of microelectronic development with respect to the mainstream of Si(Ge)- based nanotechnologies and the reasons behind this work.

1.1 Historical Context of Semiconductor Devices

In 1926, Julius Edgar Lilienfeld first patterned a three-electrode structure using copper-sulfide semiconductor material [1], which is nowadays considered as a field-effect transistor, the fundamental building block of electronic devices. About 28 years later, in 1954, the first full transistorized computer named "The TRADIC (TRAnsistor DIgital Computer or TRansistorized Airborne DIgital Computer) was made in Bell Labs (USA) lead by Jean Howard Felker [2]. At that time, the machine was a mere three cubic feet and contained almost 800 point-contact transistors and 10,000 germanium crystal rectifiers. Since then, the world has witnessed a rapid technological innovation, especially with the replacement of germanium by silicon due to its abundant resources, novel mechanical-electrical properties and stable SiO_2. Due to the continuous technological developments, the size of electrical components is shrinking down to nanoscales, giving a tremendous density of electrical components in an integrated circuit. Stated in the paper published in 1957, Gordon Moore predicted that the number of the transistors in an integrated circuit would double every two years [3]. This statement remains more or less valid until today as chip manufacturers (e.g. Intel and Samsung) continue shrinking the transistor's size with the 10- and 7 nm nodes [4,5]. Nowadays, high-tech devices are exponentially introduced, and are present in most of the aspects of our life. It is a matter of fact that people are familiar with the technological term "nanotechnologies" rather than "micro-technologies". According to the announcement of Apple company in 2018 [6], they have introduced the A12X octa-core processor with the 7 nm technology and the ability to compact 10 billion transistors per 122 mm^2 unit area. Other companies are also joining the aggressive race of producing the most powerful processing chips in recent years.

On the other hand, the miniaturization of conventional MOSFET structures is coming to a halt due to several challenges such as the leakage current through the gate oxide layer and limited doping control: in short channel transistors statistical variations in doping can lead to large variability and degradation of on/off switching characteristics [7]. Due to the integration of a high density of electrical components on a limited chip area, the temperature rise causes problems of the power consumption and operation efficiency. At the annual American Physical Society meeting at Caltech on December 29, 1959 [8], Richard Feynman had given a famous speech: "*There's Plenty of Room at the Bottom*". This sentence might be no more valid for the next ten years. Therefore, besides trying to shrink down the electrical components, people are also looking for new materials and architectures to satisfy the growing demands of fast performance and higher efficiency. Germanium returns to interest due to its excellent carrier mobility (having the highest hole mobility among semiconductors and the electron mobility is 2.5 times larger than in silicon) and the compatibility with the existing Si platform. Furthermore, for optical applications, the indirect bandgap of Ge (E_g = 0.66 eV) is just 140 meV below its direct band gap (0.80 eV). Therefore, it is possible to transform its indirect bandgap to direct bandgap by tensile strains (1.8 - 1.9%) or doping (7×10^{19} cm^{-3}) [9,10]. Si_xGe_y alloy is also attracting attention as its bandgap energy can be tailored with the compound stoichiometry, which can bring promising applications for near-infrared (NIR) detection [11]. Compared with the conventional planar bulk MOSFET channel, new architectures such as nanowires (NWs), carbon nanotubes (CNTs), nanoparticles (NPs) or quantum dots (QDs) are getting more interests due to their confinement effects.

1.2 Objective of this PhD Thesis

Since the last decade, the protruding of metals in semiconductor NWs has become a well-known process to reduce the contact resistance at the metal/semiconductor interface. The advantage of this approach is that upon heating the metal enters the semiconducting NW at both ends, creating intermetallic regions in the NW. If the process is well controlled and stopped at the right moment, only a thin section of semiconductor is left between metallic contacts, allowing to fabricate electrically contacted quantum-dot in a wire structures in a single fabrication step. The Al/Ge system in NWs appears very promising since, in contrast to other metal-semiconductor combinations, no intermetallic phase is formed and a pure monocrystalline Al NW is created with a very sharp interface with the remaining Ge NW. Moreover, the combination of the intrinsically

strong spin−orbit coupling in Ge and the superconducting properties of Al make this system a promising platform to study hybrid superconductor-semiconductor devices [12]. Previously, the diffusion behavior and kinetics of the thermal exchange reaction of the Al/Ge binary system have been carefully studied by El Hajraoui [13]. However, the real-time observation of the exchange reaction at the nucleation stage and the control of the growth rate at an atomic scale is still under-investigated. In addition, when studying the diffusion behavior of the Al/Ge reaction interface, he incidentally observed the presence of a thin Si layer between the reacted and unreacted part. Since the investigated NWs are pure Ge NWs, the presence of Si is attributed to contamination. It would be interesting to protrude Al metal in Si_xGe_{1-x} alloy NWs, expecting to produce Al/Si/Si_xGe_{1-x} nanowire heterostructures, which have shown a great potential for near infrared (NIR) or mid-wave infrared (MWIR) photodetectors [11,14].

To these above interests, the PhD thesis is set up with two targets: (i) to study the thermally induced solid state reaction of the Al/Ge binary system with the aim to deterministically fabricate Ge QDs with atomic size control between perfectly sharp metal contacts, (ii) to exploit the thermal reaction of Al metal in Si_xGe_{1-x} alloy NWs, which has not been reported in literature. To these goals, ex-situ and in-situ heating experiments are carried out for observing the formation and real time propagation of the reaction interface.

(i) For the Al/Ge binary material combination, it has been reported in the work of El Hajraoui [13] that the intrusion of Al in Ge NWs will result in the formation of a monocrystalline Al core with face-centered cubic (FCC) structure. The pure Al core is surrounded by a thin pure Ge (∼2 nm), Al_2O_3 (∼3 nm), and Ge containing Al_2O_3 (∼1 nm) layer, respectively. Combining kinetic studies of the reaction interface with three dimensional chemical modelling, he proposes a surface diffusion mechanism in the Al/Ge binary nanowire system where Ge atoms diffuse through a surface diffusion channel on the created Al NW into the Al contact pad, while Al atoms are supplied to the reaction interface by Al self-diffusion and exchange with Ge atoms at the interface. The electrical and optical transport properties of Al/Ge/Al heterostructures were elucidated in the work of Sistani et al [15] and Staudinger et al [16], where they showed quantum ballistic transport as well as quantum ballistic photo-detection at room temperature. Following these results, in our work, in-situ TEM Joule heating experiments are conducted to follow the reaction interface from the initial stage of nucleation underneath the metal/nanowire contact pad to the end of the exchange

process. Then, we investigate different parameters that can affect the diffusion rate, aiming to control the diffusion process with atomic scale precision and produce ultra-small Ge segments. The in-situ heating experiments are performed using home fabricated Si_3N_4 membrane chips flowing a current through a metal strip defined on the NW by electron beam lithography, that will heat up due to Joule heating. The electrical transport properties through the small Ge segments will also be investigated. Finally, we verify if the thermally-induced propagation of the metal phase along the NW may lead to the modification of the doping concentration next to the contact due to the so-called "doping pile-up", i.e. the dopant atoms are not integrated in the metallic phase but pushed forward into the semiconducting region [17].

(ii) For the Al-(Si, Ge) ternary system, there are a number of studies on the thermal diffusion of Al-Si, Al-Ge and Al-(Si, Ge) in bulk and thin film materials [18–20]. However, in a 1D system, the understanding of the thermal reaction is still limited. While Al can easily diffuse into Ge NWs at low temperature (< 300 ^{o}C), there is no report of Al thermal diffusion in Si NWs. This is mainly due to the low solubility of Si in Al and vice versa [21]. Therefore, to initiate the exchange reaction in Si_xGe_{1-x} alloy NWs, it is expected that higher temperatures are needed than in Ge NWs, that can't be reached using direct Joule heating. Therefore, ex-situ heating via rapid thermal annealing (RTA) and in-situ TEM heating using commercial chips (from DENSsolutions company [22]) will be used to study the Al-(Si, Ge) ternary system in a NW. The structure and composition of the generated heterostructures will be studied via geometrical phase analysis (GPA) and quantitative EDX for an understanding of the diffusion behavior and kinetics. Different factors such as NW diameter, surface quality and annealing conditions are also investigated for the interpretation of the diffusion mechanism. Finally, the transport measurement on the propagated NWs will be conducted to evaluate the potential for device applications.

1.3 Thesis Outline

In **chapter 2**, we present a literature review of the thermally activated solid-state reaction of metals in Si/Ge semiconductor nanowires with a highlight on the diffusion mechanisms. Some typical examples for state of the art nanowire applications are also demonstrated, showing a promising future for metal-silicide (germanide) for applications in modern technology. Then, the basic theory of bandgap alignments in a metal/semiconductor junction is described, which is useful for understanding the electrical transport property of electronic devices.

In the **chapter 3**, we present the detailed protocol of the sample fabrication process, including the interest of low dimensional nanowire materials, NW growth, processes of NW contacting via electron beam lithography and basic principle of ex-situ heating via the rapid thermal annealing technique (RTA).

In **chapter 4**, basic principles of electron microscopy techniques (SEM and TEM) used in this study and their subsequent applications for the structure and composition analyses such as GPA and quantitative EDX (with the 3D reconstruction) are presented. Finally, we explain the principle and electrical set-up for in-situ Joule heating experiments.

In the **chapter 5**, we present results on the thermally assisted solid state exchange reaction in the Al/Ge binary NW system. The thermal diffusion behaviors in the Al/Ge binary couple are studied with real time observations from the initial stage to the end of the diffusion. Importantly, we show the influence of electron beam radiation, surface quality and nanowire diameter on the diffusion rate. We demonstrate that an additional step of ex-situ heating by rapid thermal annealing (RTA) is preferable to initiate the reaction prior to in-situ propagation by direct Joule heating (where a current is passed through a metal line defined on the NW), since the contacts can damage due to electron migration effects. Having mastered all facets of this exchange reaction, we demonstrate a reliable control of the diffusion interface to produce a sub- 10 nm Ge QD.

In **chapter 6**, we present a study on the thermal exchange reaction in the Al/(Si-Ge) ternary NW system. The exchange reaction results in the formation of a Si-rich region, sandwiched between the reacted and unreacted NW part. The structure and stoichiometry of the created Al/Si/Si_xGe_{1-x} heterostructures were examined by GPA and quantitative EDX analyses. Ex-situ and in-situ heating

results are discussed to propose a hypothesis on the diffusion mechanism. Finally, we present electrical measurements on the created Al/Si/Si_xGe_{1-x} heterostructures.

In **chapter 7**, we summarize the findings on Al/Ge binary and Al-(Si, Ge) ternary NW systems and discuss the potential research directions on the created Al/Si/Si_xGe_{1-x} heterostructures for opto-electrical applications. In addition, we discuss about the extension of the research topic to core shell NWs, which are interesting systems to produce axial and radial metal−semiconductor nanowire heterostructures for novel applications.

1.4 Author Contributions

In this study, the sample fabrication and characterization process were done with the help and advice from different people. For the experiments, the nanowire growth was carried out by Dr. Pascal Gentile (CEA-SiNaPS) and Dr. Bassem Salem (CNRS-DRT/LETI/DCOS/LTM). The Si_3N_4 membrane fabrication was performed by Dr. Bruno Fernandez (CNRS/Institute NEEL/Nanofab) and Maria Spies (CNRS/Institute NEEL/Nanofab). Besides, Dr. Bruno Fernandez also helped in the buffered HF etching process. The Al sputtering process was performed by Dr. Stephane Auffret (CEA- DRF/IRIG/DEPHY/SPINTEC). The initial training on ALD machine was given by Dr. Laurent Cagnon (CNRS). The photocurrent measurement was done by Dr. Nicolas PAUC (CEA-SiNaPS). In chapter 5 (section 5.10) and Appendix, specimens were prepared by Dr. Masiar Sistani (TU-Wien, Austria).

For characterization, the training on the SEM machine was given by Dr. Nicolas MOLLARD. TEM training for in-situ heating experiments was given by Dr. Martien Den Hertog (CNRS/Institute NEEL). EDX mapping and quantification process was done with the training and assistance of Dr. Eric Robin (CEA/ IRIG-DEPHY/MEM/LEMMA). Moreover, the results of this study were frequently discussed within the meetings with our collaborators, Dr. Alois LUGSTEIN (TU-Wien, Austria) and later also with Dr. Olivier Buisson (CNRS/Institute NEEL) in low temperature transport measurement group.

Chapter 2

Introduction to Silicide and Germanide Phases

Silicide/Germanides are compounds consisting both of a metal and silicon or germanium. In modern microelectronics, silicide/germanide processing is a well-known technique. The silicide/germanide phase (or intermetallic phase) forms by a solid-state reaction between a metal deposited on the Si/Ge substrate induced by an annealing procedure. The introduction of an intermetallic phase between the metal-semiconductor contact benefits to a good electrical connection with low contact resistance and good adhesion, thereby reducing energy dissipation and on/off switching times [23]. In low dimensional systems like NWs, the thermal protruding of metals into the semiconductor NW can extend the intermetallic insertion from the metal contact along the NW axial direction, while maintaining the NW dimension, which interestingly brings up the possibility to produce ultra-scaled channel devices like quantum dot (QD) transistors. Due to its simplicity and versatility, numerous metals have been employed to protrude into Si/Ge NWs in the last decade, providing a large source of references. This section will briefly sum up some typical results on the thermal propagation of metal/Si and metal/Ge NWs. The thermodynamics of the diffusion process and novel applications of these investigated couples are also highlighted.

2.1 Background

In bulk and thin film materials, when two materials are brought in contact, depending on the thermal equilibrium of the system, inter-diffusion can take place at the contact interface due to the thermal vibration of atoms. The driving force can be the concentration gradient in inhomogeneous materials or self-diffusion in homogeneous materials due to the presence of vacancies. In order to exchange positions with adjacent atoms, the diffusive atom should have a minimum energy which is larger than the bonding energy with its neighbor atoms. The thermodynamics of the diffusion (in steady or non-steady state) can be described by the Fick's first and second law, respectively [24]. The temperature dependence of the diffusion coefficient is expressed by Arrhenius's equation [25]:

$$D = D_o \times \exp(\frac{-E_a}{k_B T}) \qquad (1)$$

Where: D is the diffusion coefficient at the temperature T (in Kelvin)

D_o is the pre-exponential factor

E_a is the activation energy for the reaction

k_B is the Boltzmann constant ($1.38064852 \times 10^{-23}$ m^2 kg s^{-2} K^{-1})

The thermal reaction in NWs can be different from the bulk or thin film materials due to the unique geometry and high surface to volume ratio. In such a semi 1D system, surface and interfacial energy can become more important than the thermal vibration or concentration gradient, governing the diffusion process. Since the last decade, the study of metal thermal diffusion in semiconductor NWs has been attracting a considerable interest due to great benefits of low dimensional confinement and possibilities of producing ultra-scaled devices below the spatial dimensions of traditional electron beam lithography process [26–28]. Table 2.1 presents a summary of different metals that have been used as the diffusion source for the solid-state reaction in different NW systems. The thermal reaction is often generated by ex-situ heating via rapid thermal annealing (RTA) or in-situ heating in TEM environment. Depending on the annealing conditions, the exchange reaction often results in the formation of different intermetallic phases in the propagated structure. The stoichiometry of the firstly formed intermetallic phase in a NW can be often well predicted based on the phase diagram of the couple whereas other phases formed at higher temperature are more difficult to predict. In general, the nucleation temperature for the metal phase in Ge NWs is often lower than in Si NW due to the low melting temperature of Ge (664 ^oC) compared to Si (1139 ^oC). Ni and Pt are the two metals that receive special interest in silicide or germanide processes for electrical applications. This is because of the good electrical properties of the materials and especially the epitaxial relation of the reaction products to the unreacted NW channel. Some promising applications have been proposed such as high performance field-effect transistors (FETs) [29,30]. In another system, the incorporation of Cu in Si or Ge NWs shows interesting diffusion phenomena where the reacted region shows an expansion in volume and the growth of multiple crystal branches nucleating on the NW surface [31,32]. Mn, Fe, and Co are well known substances for ferromagnetic properties. From the studies presented in refs [33–35], the thermal advancement of these metals in Si (or Ge) NWs gives interesting structures for electrical spin injection and detection. Other metal/semiconductor alloy NWs such as TiSi [36] and CrSi [37] have been characterized as good materials for field-emission and thermoelectricity, respectively.

Table 2.1: A summary of different phase formation on metal-silicide and germanide process in Si and Ge NWs.

Materials	Nucleation Temperature (°C)	Phases	References
Ni - Si	280	Ni_2Si (first phase formation), NiSi (epitaxial, Ohmic contact), $NiSi_2$, Ni_3Si, $Ni_{31}Si_{12}$, Ni_3Si_2	Ref [29,38,39]
Ni - Ge	300	Ni_2Ge (first phase formation), NiGe, Ni_5Ge_3, Ni_3Ge_2	Ref [40,41]
Pt - Si	250	Pt_2Si (first phase formation), PtSi (epitaxial, Ohmic contact)	Ref [30]
Cu - Si	350	Cu_3Si (volume expansion)	Ref [32]
Cu - Ge	310	Cu_3Ge (volume expansion), Cu_5Ge (crystal growth on reaction surface)	Ref [31]
Mn - Si	650	MnSi (epitaxial interface, ferromagnetism)	Ref [42]
Mn - Ge	450	Mn_5Ge_3 (Schottky contact, ferromagnetism)	Ref [34]
Co - Si	800	$CoSi_2$ (epitaxial, ferromagnetism)	Ref [35]
Fe - Si	540	Fe_3Si (ferromagnetism)	Ref [33]
Ti - Si	800	$TiSi_2$ (field emission)	Ref [36]
Cr - Si	….	$CrSi_2$ (thermoelectric)	Ref [37]

2.2 Kinetics of Thermal Exchange Reaction

In literature, several diffusion mechanisms have been proposed for metal-silicide and germanide processes. In fact, the diffusion behavior of different metals in Si NWs, for instance, is quite inhomogeneous. In the study of Chou et al [35] when investigating the thermal diffusion of Ni/Si and Co/Si, they observed that the length of the reacted region extends linearly as a function of time. However, looking at the length of the reacted region on smaller time scales, they noticed that the interface moves with steps corresponding to the nucleation time and radial growth across the metal/Si interface of each atomic layer. The nucleated position on the reaction interface was observed starting from the center and moving toward the edges. Importantly, they claimed that the energy difference between the oxide/Si and oxide/silicide interfaces allowed to explain the interface shape and radial kinetics of a nucleated layer. An interesting diffusion behavior of the solid-state reaction is reported in the work of Lu et al [30], where they study the Pt/Si couple when using Si NWs with and without an oxide shell. Without oxide shell, the reaction occurs as usual from the metal contact pad, resulting in the formation of PtSi/Si/PtSi heterostructures. However,

with an oxide shell, the intermetallic phase grows un-usually from the middle of the contacted NW between the two Pt contact pads, resulting in Si/PtSi/Si heterostructures. In-situ observations are therefore precious to understand such complicated diffusion mechanisms. From theoretical works presented in refs [38,39], they proposed diffusion models describing the exchange reaction of a metal/semiconductor NW taking into account different potential rate limiting steps. It is possible to gain information on the kinetics of the exchange reaction by studying the metal propagation length as a function of time and NW radius. The potential rate limiting steps and expected kinetic behavior of the reaction interface are summarized in table 2.2.

Table 2.2: Different rate limiting steps for the thermal reaction between metal and semiconductor NW where the length of the reacted region (***L)*** will behave as a function of time (***t***) and NW radius (***R***). Ref [38,39].

Rate limiting step of Silicide/Germanide formation	**L**
Interface at the NW/metal contact pad	~ $\mathbf{R^{-1}t}$
Silicide/Si or germanide/Ge interface	~ **t** (Independent of **R**)
Volume diffusion	~ $\sqrt{\boldsymbol{t}}$ (Independent of **R**)
Surface diffusion	~ $(\sqrt{\frac{\boldsymbol{t}}{\boldsymbol{R}}})$

The table 2.2 gives us a cue to identify what factors limit the diffusion process. The surface area between the NW and metal reservoir can be a limiting factor as it determines the diffusion flux of metal atoms into the NW, which is defined as the number of diffusive atoms per unit area. Other potential rate limiting factors can be either volume or surface diffusion, which have been introduced in the work of Yaish et al [39]. While both show a square root dependence of the metal propagation length on the reaction time, surface diffusion shows an inverse influence of the NW radius (R) on the silicide/germanide reacted length, while volume diffusion is independent of the NW size. Then, the rate limiting step in the reaction can occur at the silicide/Si interface, which should theoretically lead to a linear dependence of the silicide length on the propagation time, while being unaffected by the NW size (Ref [43]). Besides, the size of the metal reservoir can also influence the reaction. If the metal contact pad is small, the reaction may stop due to the saturation of the semiconductor content in the metal reservoir [44].

The silicide/germanide process in 1D system often results in the formation of metal/semiconductor axial heterostructures. For the device application, the transport property through the created heterojunctions should be fully investigated. In the coming section, we would like to give a brief introduction to the band energy alignments when bringing a metal and semiconductor into contact.

2.3 Band Alignment of Metal/Semiconductor Junction

In solid-state physics, described by the Rutherford–Bohr model, electrons in a single atom have discrete energy levels with respect to their atomic orbital. Electrons close to the nucleus have the lowest energy level whereas in the outermost orbit, electrons have the highest energy level. In materials, atoms are linked together in a specific arrangement forming lattices. Due to the enormous number of atoms in the material (about 6.023 x 10^{23} atoms per mol) and small distance between the atoms, the electron energy levels overlap forming a continuum. As inner and outer electron shells have different energy levels, the inner shells which are fully filled by electrons are referred to as the valance band (VB). The outer shell which is partially filled is called the conduction band "CB". The gap between the VB and CB is technically named as the bandgap energy of the material. Bandgap energy can be used to identify whether a material is an insulator, semiconductor or metal. In insulators and semiconductors, electrical charges cannot move freely within the lattice. They are confined in specific energy levels and require a certain energy to move from the VB to the CB. Normally, materials which have the bandgap smaller than 3.2 eV are considered as semiconductors. Larger bandgap energy materials are characterized as semi-insulators and insulators. Figure 2.1 shows the bandgap energies of different semiconductors versus their lattice constant.

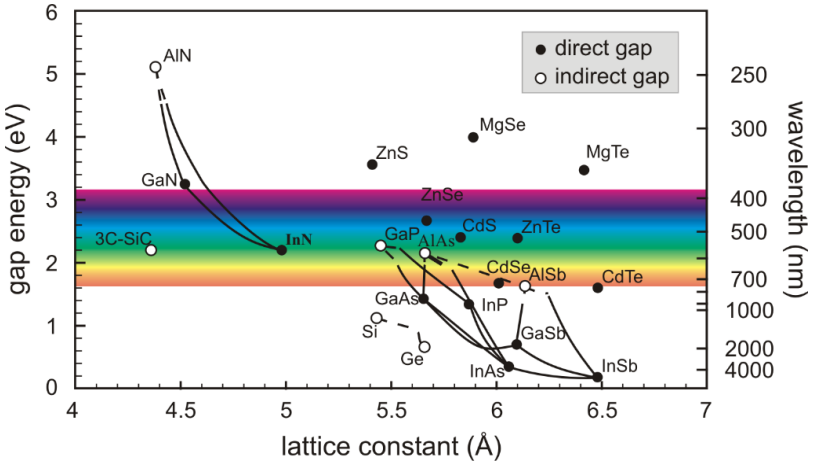

Figure 2.1: Bandgap energies of different semiconductors versus their lattice constant. Ref [45].

In metals, the VB is either not fully filled by electrons or overlaps with the CB. Electrons in metals are thus free to move within the lattice (so-called Fermi gas). Different from semiconductors, when raising the temperature, the thermal vibration of metal atoms increases, preventing the movement of free electrons. Therefore, the conductivity of metal decreases with an increase of the temperature. The highest energy state of electrons in a substance at zero temperature is called the "Fermi level". In intrinsic semiconductors (pure element), excited electrons will jump from the VB to the CB and release holes in the VB (positive charges) upon excitation, for example with light of the right energy. These electrons will then relax to lower energy levels and recombine with holes in the VB, giving the neutral state of the semiconductor. As the number of electrons and holes is equal, the Fermi level stays in the middle of the bandgap. The introduction of impurities into intrinsic semiconductors is called doping (see figure 2.2). If a dopant has 3 valence electrons, it will add a positive charge to the semiconductor (p-type) whereas if the dopant has 5 valance electrons, it donates an electron to the material (n-type). The fermi level is therefore shifted up or down depending on the doping impurities.

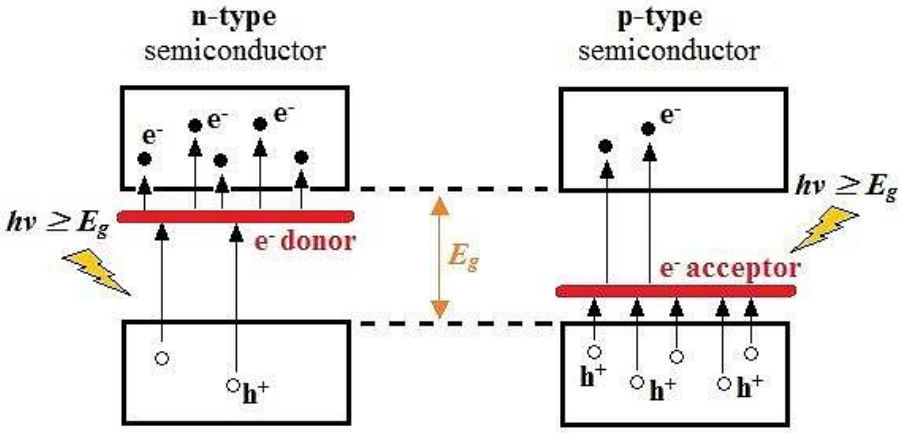

Figure 2.2: Illustration of n-and p-type doping in a semiconductor. Ref [46]

In metal and semiconductor, the minimum energy required to remove an electron from the surface to a vacuum level is called the work function (ϕ), defined as the difference between the vacuum level $\mathbf{E_0}$ and the fermi level of the metal ($\mathbf{E_F}$):

$$\phi = E_0 - E_F \qquad (2)$$

Whereas, the variation of the energy when adding an electron in a semiconductor is called the electron affinity χ_s, which is defined as the difference between the vacuum level E_0 to the bottom of the conduction band (E_{Cs}):

$$\chi_s = E_0 - E_{Cs} \quad (3)$$

A summary of the work functions and electron affinities of some metals and semiconductors is presented in table 2.3.

Table 2.3: A summary of the work functions and electron affinities of some metals and semiconductors [47,48].

Metal		Semiconductor	
Element	**Work function (eV)**	**Element**	**Electron affinity (eV)**
Ag	4.26	Ge	4.13
Al	4.28	Si	4.01
Au	5.1	GaAs	4.07
Cr	4.5	GaN	4.1
Mo	4.6	AlAs	3.5
Ni	5.15		
Pd	5.12		
Pt	5.65		
Ti	4.33		
W	4.55		

When bringing a metal and semiconductor into contact, in the absence of an external potential, the band energies of the metal and semiconductor realign in such a way that the Fermi levels will line up and the vacuum level is continuous. Figure 2.3 demonstrates the band alignment of a metal and n-type semiconductor before and after making contact. Since the initial Fermi energy in the metal differs from that in the semiconductor, electrons in the n-type semiconductor can lower their energy and move from the semiconductor to the metal. This movement results in a polarization of the contact interface where positive charges are generated on the semiconductor side while more electrons are incorporated on the metal side. An internal electric field is consequently created within the polarized interface. When the electron diffusion from the semiconductor to the metal as described in the first step and the electron attraction from the metal to the semiconductor due to the

induced electric field have reached an equilibrium, the interface is depleted by a depletion width, *W*.

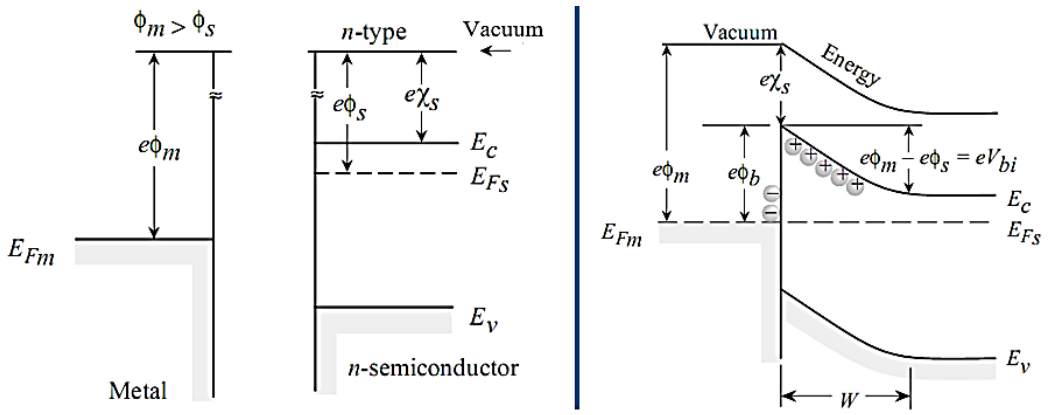

Figure 2.3: Band alignments of metal and n-type semiconductor before and after making contact. Ref [49]

The difference between the Fermi energy of the metal and that of the semiconductor is called the built-in potential (**V_{bi}**), which is calculated by equation (**4**):

$$V_{bi} = \phi_m - \phi_s \qquad (4)$$

For the case of metal and p-type semiconductor contact, the band energy alignment can be demonstrated as shown in figure 2.4.

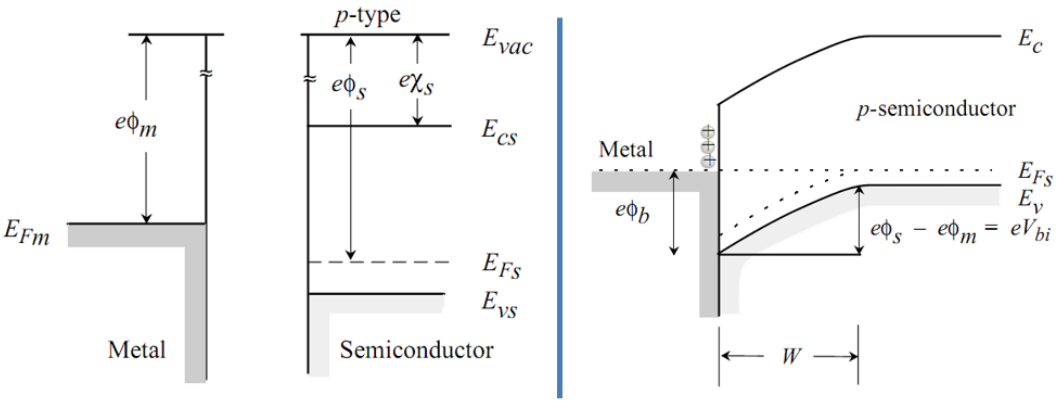

Figure 2.4: Band alignments of metal and n-type semiconductor before and after being contacted. Ref [49]

The depletion region can be narrowed or expanded with an external bias potential. If the internal electric field between the metal/semiconductor junction has the same direction as the external field, carriers are more separated expanding the depletion region. This process is called “the reverse bias”

with almost no current existing across the junction. In contrast, when the internal and external field have opposite directions and the applied voltage is comparable to the built-in potential, the two electric fields may cancel each other. The depletion region is narrowed and carriers are able to move across the junction, giving a current (the forward bias). The contact interface is said to be Ohmic if only a small bias potential is needed to transfer carriers across the interface. In this case, the IV characteristic across the junction shows a linear relation. On the other hand, the contact is called rectifying when a sufficiently high potential is required for transporting carriers through the interface. The above theories are true in the case of perfect crystal structure of the semiconductor interface. However, in practice, surface states can exist at the semiconductor surface due to the missing bonds of the surface atoms with their neighbors, defects or impurities. Then, the semiconductor Fermi level will align with respect to these states ($\boldsymbol{\phi_o}$) without the influence of the metal work function. Figure 2.5 presents the band alignment of metal and semiconductor energy levels in the presence of such defect states.

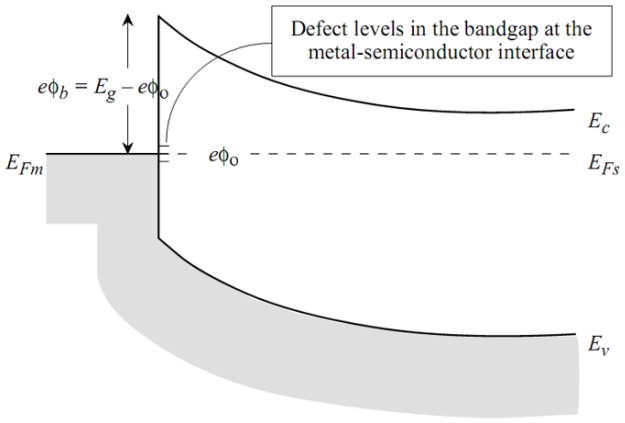

Figure 2.5: Band energy alignment of the metal and semiconductor in the presence of defect states. Ref [49]

Due to the large number of defect states that can be present on the semiconductor surface, the contact between the metal and semiconductor often has a rectifying behavior, and the characteristics of such a junction are determined by the Schottky barrier height.

Chapter 3

Sample Fabrication

In this chapter the sample fabrication process will be described step by step. After a rapid description of the interest of nanowires, the metal catalyst-assisted vapor–liquid–solid (VLS) mechanism for the NW growth will be briefly discussed as it is of relevance for the growth of both n-doped Ge NWs as well as Si_xGe_{1-x} alloy NWs that were studied. Then a detailed protocol of the NW contacting process will be presented sequentially, including the pre-steps of nanowire surface treatment to remove the native oxide shell, the patterning process using electron beam lithography and the different Al metal deposition techniques. Finally, the ex-situ heating process via rapid thermal annealing (RTA) will be discussed for the initiation of the thermal exchange reaction between the Al metal and the semiconductors. In this study, in-situ TEM heating is also used, which will be discussed in section 4.4: In-situ (S)TEM Heating Techniques.

3.1 Potential of Nanowires

In recent years, the study of NW-based devices attracted a huge interest as NWs possess unique electrical, chemical and optical properties. The NW diameter [50] can be as small as 1 nm, and the length [51] can be in range of a few μm to hundreds of μm. Different types of nanowires can be synthesized and are investigated such as superconducting [51], metallic [52], semiconducting [53], insulating or molecular nanowires [54]. Among these, semiconductor NWs are important building blocks for the development of modern technologies. Owing to the radial confinement, semiconductor NWs can exhibit an interesting physical property of “diameter-dependent band gap” [55]. With the unique property of the high aspect ratio and large surface to volume ratio, NWs promise great benefits to advanced optoelectronics applications for their emission or absorption behavior. Various applications of nanowire-based optoelectronic devices have been developed such as light-emitting diodes (LEDs) [56], photodiodes [57], lasers [58] and photovoltaic cells [59]. Furthermore, it is possible to modify the composition, doping level or defect concentration in a NW structure for electronic applications such as nanowire transistors (FETs) [53], bipolar transistors [60] or p-n diodes[61].

3.2 Semiconductor Nanowire Growth

NWs can be grown by several techniques such as the metal-catalyst-assisted vapor–liquid–solid (VLS) mechanism [62], the vapor–solid- solid (VSS) mechanism [63] or the template-assisted (TA) [64] method. The VLS growth mode is often used in combination with the chemical vapor deposition (CVD) technique for growing semiconductor nanowires, due to its relative simplicity and versatility.

In our study, n-doped Ge NWs and Si_xGe_{1-x} alloy NWs grown by VLS mechanism using gold colloids as catalyst on Ge (111) substrate are being investigated. The NWs were grown in the SiNaPS laboratory and LETI/DCOS/LTM laboratory in CEA-Grenoble. For Ge NWs, the diameter of the as-grown NWs varies from 100 nm to 160 nm with about 8 μm length. The growth of Ge NWs was performed by an Au-catalyzed process in a CVD chamber using GeH_4 gas as precursor. For Si_xGe_{1-x} alloy NWs, the as-grown NWs have a strong fluctuation in diameter, ranging from 65 to 250 nm. Silane (SiH_4) and GeH_4 gases were used as precursors and Au colloids as catalyst. The growth of Si NWs via the VLS mechanism using Au catalyst can be described by the following steps:

i. Solid Au nanoparticles of a specified diameter are dispersed on a cleaned Si substrate. As the NW will grow epitaxially on the provided substrate, the growth direction of the NWs is influenced by the substrate crystallography and orientation.
ii. The Au dispersed substrate is heated above the eutectic temperature of the Au-Si system (363 °C) in inert atmosphere. Then, a vapor phase of Si precursor (SiH_4) will be continuously introduced to the Au particles and the Si precursor is decomposed at the catalyst surface.
iii. The Si concentration in the liquid Si-Au alloy droplets increases and reaches the supersaturation state. Then Si in solid form will precipitate at the bottom of the liquid droplet, nucleating the Si NW. The length of the grown NW will be controlled by the growth time and the diameter will be designed by the Au catalyst diameter.

As an example, the Si-Au phase diagram and the schematic illustration of the VLS mechanism for the growth of Si NWs are presented in figure 3.1.

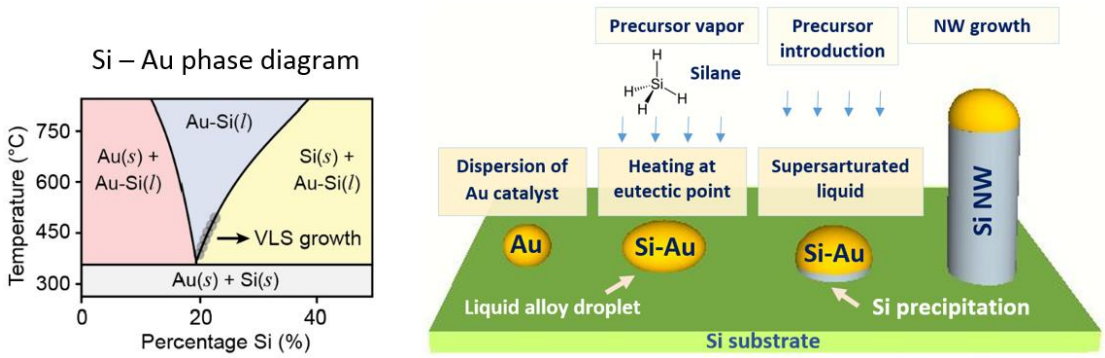

Figure 3.1: Si-Au phase diagram [65] (**left**) and the VLS method of growing Si NWs using gold as catalyst (**right**).

The growth of Ge or Si_xGe_{1-x} NWs will proceed in a similar fashion, only the heating temperature for the Ge and Si_xGe_{1-x} NW growth were changed to 380 ^oC and 450 ^oC, respectively. For both type of NWs, hydrochloric acid (HCl) was used to control the NW shape and also reduce the gold surface migration effect [66]. Figure 3.2 shows the SEM images of the $Si_{0.05}Ge_{0.95}$ alloy NWs fabricated by the VLS mechanism using Au colloids as catalyst. The NWs were grown on the Ge (111) substrate with low density. The NWs have a non-uniform shape with increasing diameter from the top to the bottom. This is due to the effect of uncatalyzed surface deposition during the growth process.

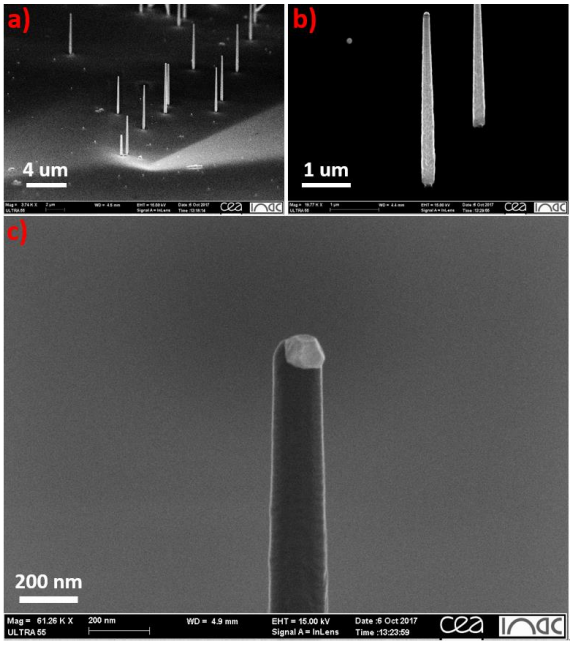

Figure 3.2: **a-b**) SEM images of the $Si_{0.05}Ge_{0.95}$ NWs fabricated on the Si (111) substrate. **c**) Zoom on the top part of the NW showing the size and shape of the gold catalyst.

3.3 NWs Preparation

It is a matter of fact that silicon or germanium NWs are always covered by a native oxide layer (about 2~3 nm thickness) when they have been exposed to an atmospheric environment [67]. To obtain a high contact quality between the NW and the metal contact, the insulating oxide layer must be removed before depositing the metal contact. A wet chemical process is a common method for surface preparation prior to subsequent growth processes such as epitaxial growth or atomic layer deposition (ALD). Since the GeO_2 is water soluble, we have removed this oxide layer by HI acid etching and deposited Al_2O_3 by ALD technique for the NW protection. In the next sections we first describe the observation of a highly n-doped shell around the n-doped NW's, followed by the different surface treatments that were done.

3.3.1 Detection of Highly n-doped Shell

The initial target of this PhD was to determine the diffusion behavior of phosphorous dopants in a doped (10^{19} atoms/cm^3) Ge NW influenced by an Al exchange reaction where Al propagates into the n-doped Ge NW. For a reliable examination, the dopant distribution within the NW cross-section should be uniform in both the radial and axial direction. However, from the EDX analysis on the as-grown NWs, we have observed the presence of a thin highly n-doped Ge shell (about 10 nm) around the NW. Figure 3.3a presents the HAADF STEM image of the as-grown n-doped Ge NW dispersed on a lacey carbon TEM grid. The EDX mapping and the integrated analyzed spectra obtained on the blue box1 (on the shell) and red box2 (in the core) are shown in figure 3.3b-c. The background normalization of the two spectra illustrates the non-uniform distribution of P content across the NW cross-section (P peak is highlighted by the orange arrow in figure 3.3c). Indeed, the non-uniform radial distribution of phosphorus in VLS grown Ge NWs has been reported in the study of Perea et al [68]. It has been pointed out that phosphorus incorporation in the NW core through the catalyst is lower than the phosphorus deposition and incorporation at the surface via an uncatalyzed process. In an effort to remove the highly n-doped shell in p-i-n junction Ge NWs, Guilloy [69] has proposed to use diluted 10% hydrogen peroxide solution (H_2O_2) for etching the shell. After the etching process, the current−voltage (I-V) measurement was done on the NW, showing a transition from Ohmic to rectifying behavior.

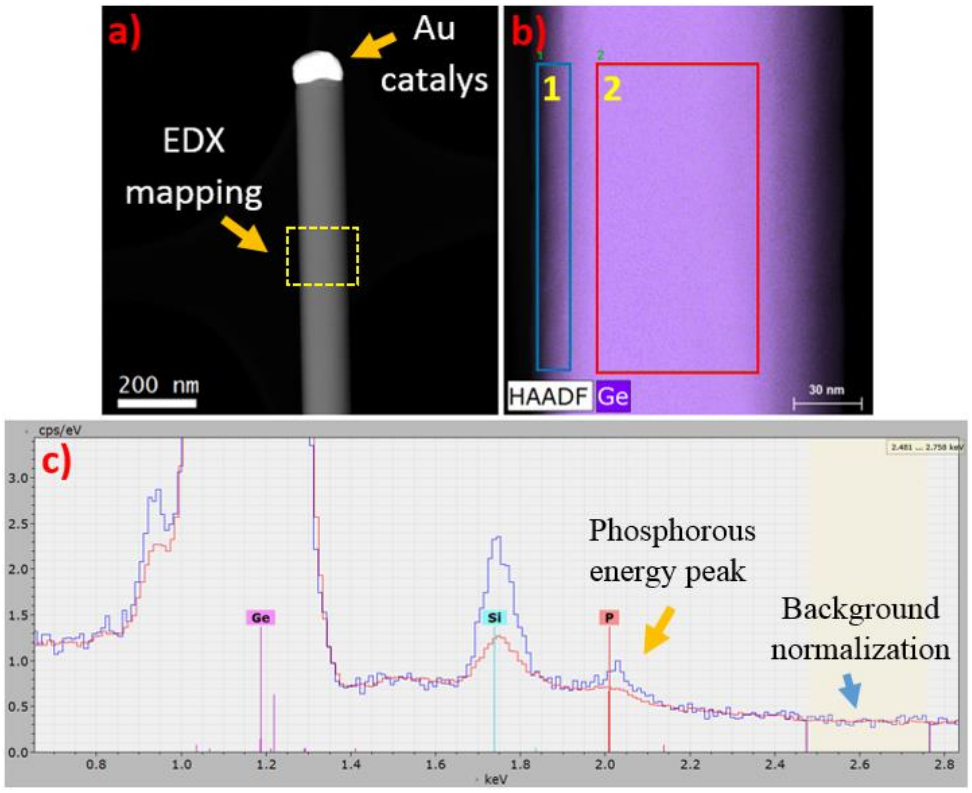

Figure 3.3: a) HAADF STEM image of the n-doped Ge NWs fabricated by VLS mechanism using gold as catalyst. **b**) EDX hyper-map taken at the dash yellow box (shown in Fig. 3.3a) and **c**) spectrum analysis taken on the blue and red boxes (Fig. 3.3b). The blue and red line spectra correspond to the spectrum of the shell and the core of the NW.

3.3.2 Hydro Peroxide (H_2O_2) Etching of n-doped Ge Shell

In our experiments, hydrogen peroxide solution 30% (H_2O_2 - Carlo Erba [70]) was used to remove the n-doped Ge shell. The hydrogen peroxide has a high etching rate, and therefore was first diluted with deionized water (DIW) to reduce its reactivity. The ratio of the H_2O_2 to the DIW is 1:2. To proceed, the as-grown NWs on Si (111) substrate was dipped in the etchant for 20 s and then rinsed in DIW for 20 s, followed by N_2 blow dry. Figure 3.4 shows SEM images of the n-doped Ge NWs before and after the hydrogen peroxide etching process. As can be observed at the gold catalyst position, about 20 to 30 nm of Ge shell was removed from the NW.

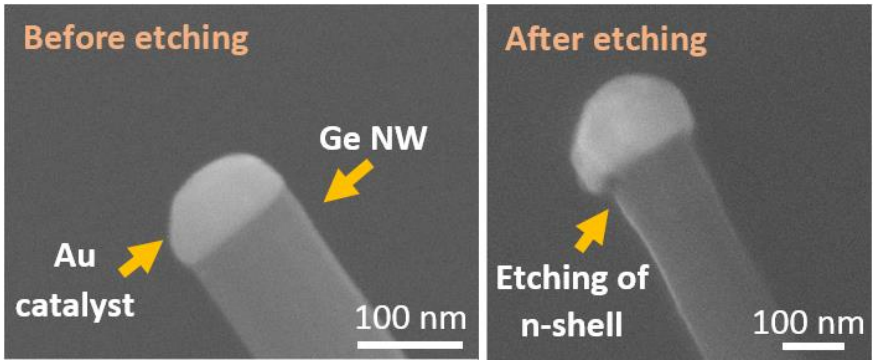

Figure 3.4: SEM images of the n-doped Ge NWs before and after the hydrogen peroxide (H_2O_2) etching process. The etching process was done by dipping the sample in diluted H_2O_2/DIW as ratio of 1:2 for 20 s and then DIW for 20 s, followed by N_2 gas blow. After the etching, about 20-30 nm of the n-doped shell was removed.

3.3.3 HI Acid Etching of GeO_2 Shell

Unlike the stable SiO_2 shell, which is typically removed by buffered HF acid, GeO_2 is water soluble. In practice, GeO_2 is often removed by hydrohalogenic acids such as HCl, HBr or HI. From the study of Onsia et al [71], it has been shown that HBr and HI are the best solutions for etching GeO_2. Figure 3.5 shows the XPS spectrum of the Ge wafer surface after a treatment by different hydrohalogenic acids for 5 min. The peak at 30 eV shows the binding energy of Ge bulk. The peak around 33 eV shows the presence of the germanium oxide GeO_2. Clearly, there is still GeO_2 remaining after HF and HCl acid etching while HBr and HI acid show a good etching result.

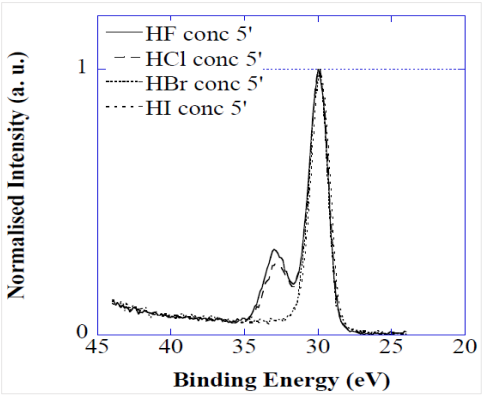

Figure 3.5: The XPS spectrum [71] of the Ge wafer surface after being etched by different hydrohalogenic acids for 5 min. The peak at 30 eV indicates the binding energy of Ge while the peak at 33 eV corresponds to the position of GeO_2.

In our experiments, hydriodic acid (HI acid, >57%, Sigma-Aldrich-MERCK [72]) was used for removing the GeO_2 shell around the NW. The sample was dipped in diluted HI/DIW with the ratio of 1:5 for 5 s and then rinsed in DIW for 20 s to remove all the residual chemicals and subsequently dried by blowing N_2 gas. After the etching process, the sample should be transferred immediately to the deposition chamber that is then pumped to create a vacuum to avoid re-oxidation.

3.3.4 Atomic Layer Deposition (ALD)

The downscaling of modern technologies has led to the requirement for atomic scale control of thin film deposition. Compared with the common physical deposition processes like evaporation or sputtering, which have a high growth rate, atomic layer deposition (ALD) is a chemical vapor deposition technique with high accuracy and repeatability [73]. The depositing process is electrically controlled with the growth rate of Å/cycle. It is possible to deposit on different types of thermally fragile substrates such as inorganic, polymeric, or biological materials by using low-temperature ALD [74]. As the mainstream of modern microelectronics is shifting to nanoscale devices, ALD is thus highly required for depositing ultrathin high-k dielectric materials [75] such as Al_2O_3, HfO_2 or ZrO_2. ALD offers an excellent step coverage and conformal deposition on high aspect ratio structures based on sequential, self-limiting reactions. The process is based on alternate pulsing of the precursor gases and vapors onto the substrate surface and subsequent chemisorption or surface reaction of the precursors. A Quartz crystal microbalance (QCM) is used to examine the deposition processes.

In our experiments, we have deposited 5 nm or 20 nm of Al_2O_3 shell on the n-doped Ge NWs and $Si_{0.67}Ge_{0.33}$ NWs, respectively, to passivate the NW surface. The Al_2O_3 coating process was performed using H_2O and $Al(CH_3)_3$ [trimethylaluminum (TMA)] based on two reactions:

(A) $\quad Al\text{-}OH^* + Al(CH_3)_3 \rightarrow Al\text{-}O\text{-}Al(CH_3)_2^* + CH_4$

(B) $\quad Al\text{-}CH_3^* + H_2O \rightarrow Al\text{-}OH^* + CH_4$

The mechanism of Al_2O_3 growth based on self-limiting reactions is illustrated by the schematic in figure 3.6.

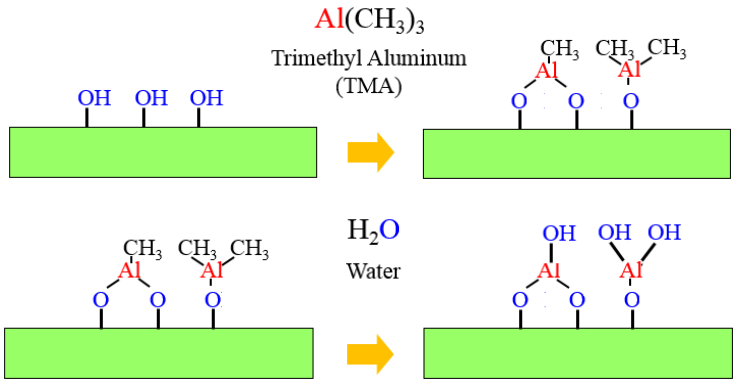

Figure 3.6: Schematics of self-limiting reactions in ALD technique for Al_2O_3 deposition using H_2O and $Al(CH_3)_3$ [trimethylaluminum (TMA)].

The deposition process is repeated for several cycles to obtain the desired thickness. Figure 3.7 shows the HAADF STEM image of the passivated $Si_{0.67}Ge_{0.33}$ NW covered by 20 nm Al_2O_3 shell. For the ALD deposition, the substrate temperature was kept at 250 ^oC and the peak pressure of H_2O and TMA pulse were set at 2 Torr and 0.8 Torr respectively, giving 20 nm of Al_2O_3 thickness after 200 cycles.

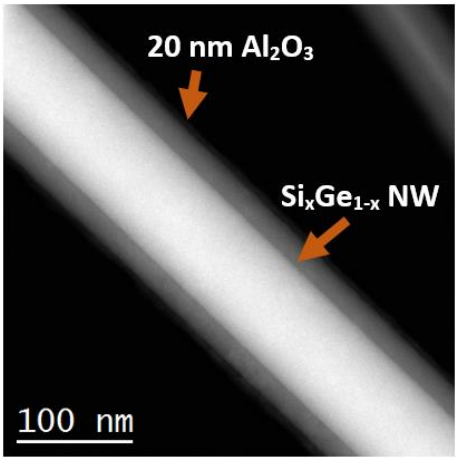

Figure 3.7: HAADF STEM image of a $Si_{0.67}Ge_{0.33}$ NW with 20 nm Al_2O_3 shell deposited by ALD technique. The arrows show the positions of the Al_2O_3 shell and the $Si_{0.67}Ge_{0.33}$ core of the core-shell NW.

3.4 Ebeam Lithography

Electron Beam Lithography (EBL) is a fundamental technique in nanofabrication, allowing to transfer a two dimensional (2D) electronic pattern to a substrate using subsequent processes. The NW contacting process contains four main steps, including the dispersion of the NWs on the Si_3N_4 membrane, spin coating of a photoresist, the exposure of the resist and the development step. An extra step of plasma cleaning is also useful to remove residual resist after the development step. After metal deposition the 'lift off' step removes all the resist, including the metal deposited on the resist. Only the metal deposited directly on the sample surface should remain.

3.4.1 NWs Dispersion

The EBL process starts with the transfer of the as-grown NWs to a substrate. In our experiments, for the TEM investigation, we have dispersed the NWs either on the home-made 200 nm thick electron transparent Si_3N_4 membrane (Fig. 3.8a) or the temperature calibrated heater chips from DENSsolutions company (Fig. 3.8b) [22]. Rectangular holes are present in both types of membrane. Additionally, NWs were also dispersed on home-made 40 nm thick electron transparent Si_3N_4 membranes without holes, to which we refer as 'flat' membranes. The fabrication process for the home-made Si_3N_4 membrane was described in ref [76]. Particularly shown in figure 3.8a, the membrane has 6 large gold or platinum electrodes for outer electrical connection and a 200 μm x 200 μm electron transparent Si_3N_4 window at the center of the membrane (see Fig. 3.9a) used for the TEM observation. The NWs are randomly dispersed on the Si_3N_4 window and connected to outer electrodes via the thin gold inner electrodes using electron beam lithography. For the temperature calibrated heater chips (Fig. 3.8b), a buried metal spiral of well-defined dimensions is present in the center of a 400 nm SiN_x membrane that is commercialized by DENSsolutions. The membrane chip can raise the heating temperature up to 1300 ^oC within a few seconds.

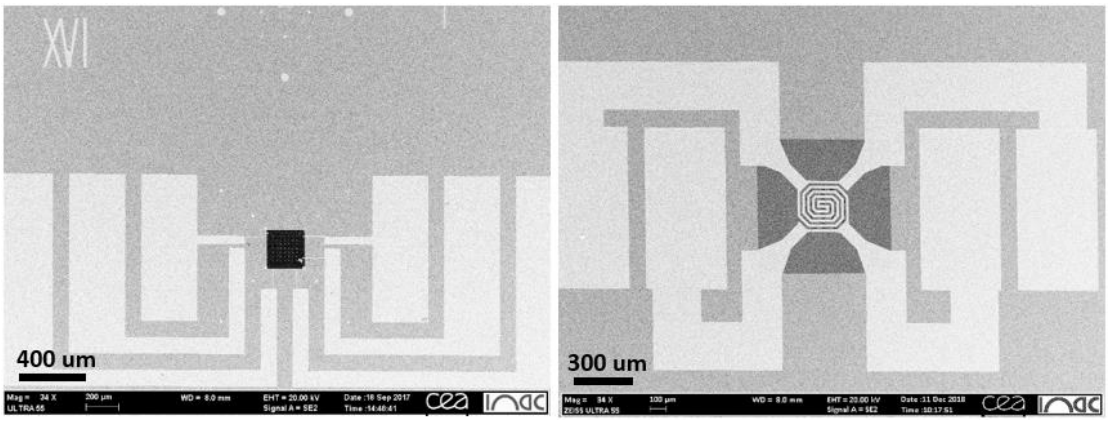

Figure 3.8: SEM images of **(a)** home-made 200 nm thick electron transparent Si_3N_4 membrane and **(b)** the temperature calibrated heater chips from DENSsolutions company.

To begin the NW contacting process, the substrate containing the as-grown NWs is first separated into around 3 mm x 3 mm pieces and immersed in ethanol solution (in a small plastic container). A moderate sonication step is applied to the plastic container for about 20 s to break the NWs from the substrate. Droplets of the NW solution taken by a micropipette are spread on the Si_3N_4 membrane followed by N_2 blow-drying. Depending on the density of the as-grown NWs on the growth substrate, the dispersion step can be repeated one or several times. The NW density is verified by optical microscope observation until the expected NW position and density on the membrane is achieved. If there are holes on the membrane (shown in Fig. 3.9), the NWs are attracted to move into the holes giving higher NW density of suspended NWs. It is very interesting to obtain suspended NW structures, to get rid of the influence of the Si_3N_4 substrate. This is beneficial both for EDX measurements as well as field mapping techniques such as electron holography [77]. However, the non-uniform coating of the resist layer caused by the holes can increase the risk of lift-off problems. For the NW dispersion on the calibrated heater chip, since the size of the chip is quite small, it is advised not to use N_2 gas for blow-drying, but letting the membrane dry gradually on a hot plate (at ~70 ^oC) to achieve high NW density on the membrane. After that, SEM images of the dispersed NWs are made to localize the NWs and making the designed patterns using Klayout [78] or Elphy software.

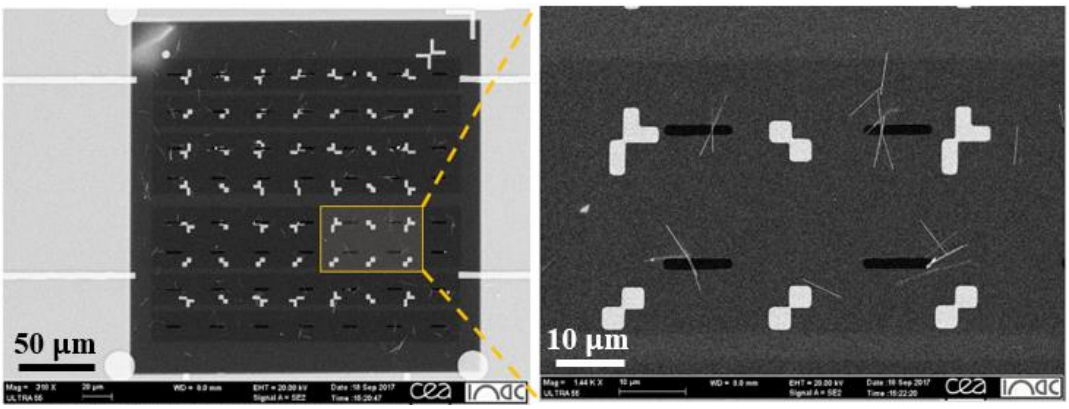

Figure 3.9: (**a**) SEM image of NW dispersion on the Si_3N_4 window and (**b**) a zoom on the yellow rectangular box showing the 2 µm x 8 µm holes and markers with Ge NWs lying over the holes.

3.4.2 Spin Coating of Resist

To facilitate the spin coating of the resist and also to avoid the breaking of the thin Si_3N_4 membranes by the vacuum pressure, it is advised to glue the membranes on top of a Si wafer using orange Kapton tape. The sample is then spin coated by PMMA 4% (positive photoresist) and baked at 180 ^oC for 5 min. Depending on the thickness of the deposited metal, the thickness of the photoresist should be adjusted to have a good lift-off. Normally, the thickness of the deposited metal should be less than 1/3 of the resist thickness for a good lift-off. In our experiments, in order to perform the Al metal contacts to 100 nm n-doped Ge NWs, we have deposited 150 nm Al metal layer. The resist thickness required for a good lift-off is about 500 nm, which could be done by two times of the PMMA 4% spin coating with the recipe presented in the table 3.1.

Table 3.1: Recipe for the spin coating process using PMMA 4% as photoresist

Resist	Spin coating			Bake		Thickness (nm)
	Velocity (rpm)	Acceleration (rpm/s)	Time (s)	Bake (^oC)	Time (min)	
PMMA 4%	4000	4000	30	180	5	250

To contact larger NW diameters (for instance, $Si_{0.67}Ge_{0.33}$ alloy NWs with the diameter ranging from 65 to 250 nm), the metal thickness should be large enough to assure a good coverage of the NW surface. In this case, we have performed three times of PMMA 4% spin coating for 750 nm resist thickness, and then deposited 300 nm of Al metal.

3.4.3 Exposure of Resist

The exposure of the resist is performed on the ZEISS LEO1550 SEM working at 20 kV. First, the drawings made using the Klayout software are loaded in the machine and opened (with Elphy software) for the 2D patterning. Then markers pre-patterned on the Si_3N_4 are used for doing a calibration of the writing field and correction of the shift and rotation of the writing field. Then the focused electron beam raster scans the field of 300 µm x 300 µm on a membrane with a beam current of ~30 pA and deposits an electron dose of 375 µC/cm^2. The step size of the scanning should be below 2 nm/s. Since the exposure to the electrons of the photoresist will influence its properties, it is advised not to expose the membrane by focusing directly on the writing field or taking images at slow scan-speed.

3.4.4 Development

After the exposure, the sample is dipped in MIBK/IPA 1:3 [methyl isobutyl ketone/isopropyl alcohol] for 55 s (for 500 nm thick photoresist) and then IPA for 1 min to remove the developer. If the thickness of the photoresist is about 750 nm, the development time should be about 80 s. Since the resist is sensitive to white light, it is advised to cover the samples by aluminum foil for transferring to the metal deposition step (that is performed in another cleanroom). Figure 3.10 illustrates four basic steps for NWs contacting using electron beam lithography.

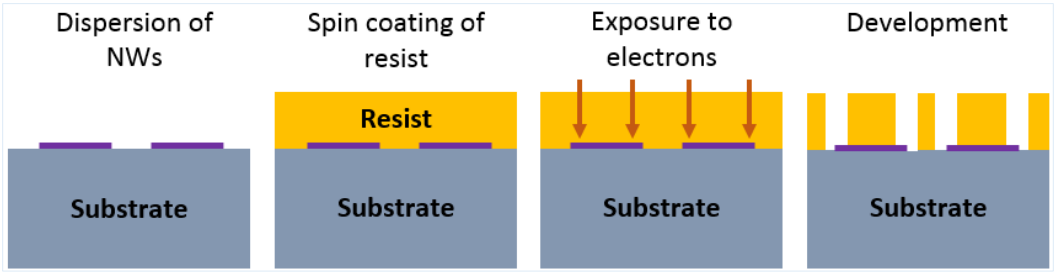

Figure 3.10: four basic steps of NWs contacting process including the dispersion of NWs, the spin coating of resist, the exposure of the resist at well-defined locations and the development step removing the resist where it has been exposed to the electron beam.

3.5 Buffered Oxide Etching (BOE)

Buffered oxide etch (BOE), also known as buffered HF or BHF, is a commonly isotropic etchant in nanofabrication used to remove amorphous SiO_2, Al_2O_3 or Si_3N_4 [79]. Buffered HF is a strong acid, highly corrosive and toxic. Due to the risks of BOE appropriate safety measures need to be taken for handling: wearing full protective clothing including boots, safety goggles and/or a full face-shield and gloves of PVC or neoprene is recommended. In our experiments, buffered hydrofluoric acid [80] - BOE 7:1 (HF : NH_4F = 12.5 : 87.5%) was used to remove the protecting Al_2O_3 shell that covered the NW surface at the location where the Al contact pad would be deposited in a subsequent fabrication step. The recipe for Al_2O_3 etching is presented in table 3.2.

Table 3.2: Information for Al_2O_3 etching using buffered hydrofluoric acid

Al_2O_3 thickness (nm)	Time (s)	DIW (s)	Air blow
5	10	20	N_2
20	50	20	N_2

Buffered HF has a negative side effect on the etching process that the F^- ions diffuse underneath the layer of resist and etch the substrate causing 'resist peeling' or 'under-etching' effects as demonstrated in figure 3.11.

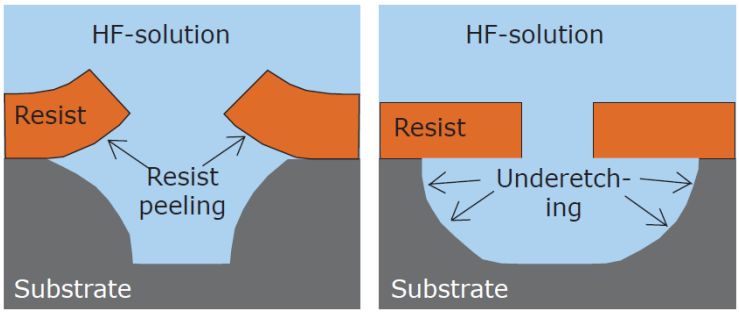

Figure 3.11: Demonstrations of poor adhesion of the resist (**left**) and isotropic etching of the substrate (**right**) by using HF acid solution.

Figure 3.12 shows the HAADF STEM image of the contacted $Si_{0.67}Ge_{0.33}/Al_2O_3$ core shell NW etched by buffered hydrofluoric acid. As indicated by the orange arrows, not only the Al_2O_3 shell but also the $Si_{0.67}Ge_{0.33}$ core has been etched by the buffered HF acid. The HF etching was also extending underneath the resist layer over a distance of around 500 nm. In addition, due to the use

of a Si_3N_4 membrane, the buffered HF etching process thins down the membrane increasing the risk of breaking the membrane during the lift off process. To reduce these negative effects, it is advised to rinse the sample with DIW carefully to remove the HF residual acid and also reduce the HF etching time by depositing a thinner Al_2O_3 shell (<10 nm).

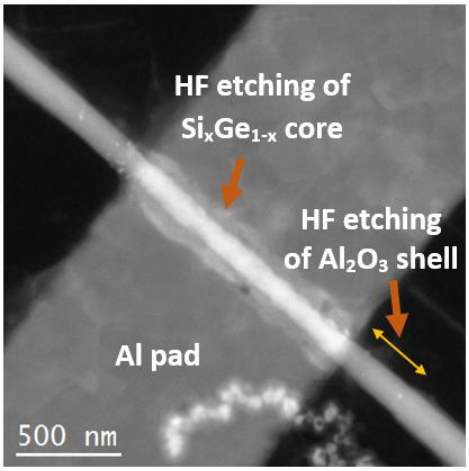

Figure 3.12: HAADF STEM images of the Al contacted $Si_{0.67}Ge_{0.33}$ NWs with 20 nm Al_2O_3 shell showing the etching of SiGe NW underneath the Al contact pad and the extension of Al_2O_3 etching below the resist.

3.6 Al Deposition

In this section, we will describe the process of Al metal deposition using sputtering and electron beam evaporation techniques. Some typical characteristics of the two methods are also given. Besides, prior to the metal deposition process, an additional step of soft plasma cleaning will be applied and discussed for the removal of impurities and contaminants on the contact surface.

3.6.1 Ar Plasma Cleaning

Ar plasma cleaning is a common technique used to remove organic contaminations via ion bombardment without causing a chemical reaction or oxidation on the surface of the substrate [81]. The plasma is created using high frequency voltages (typically kHz to >MHz) to excite gas atoms to higher energy states and become ionized. The atoms are then relaxed to lower energy levels and emit photons resulting in the characteristics "glow" or "purple – blue" light associated with plasma. The cleaning process is considered as environmentally friendly since there are no harsh chemicals involved. During our sample fabrication process, after installing the specimen in the evaporation or sputtering chamber for vacuum protection (10^{-6} Torr), a soft Ar plasma cleaning (250 V) is

applied for 15 s. The chamber is then pumped to 10^{-6} Torr to remove the Ar gas, preparing for the Al deposition step.

3.6.2 Al Deposition by Sputtering and Electron Beam Evaporation

Sputtering and electron beam evaporation are common physical thin film deposition techniques in nanofabrication [82]. A wide range of materials such as metals, insulators, alloys and composites can be used as the target [83]. For the sputtering technique, gas atoms (commonly argon) are excited by a high bias voltage and directed to make collisions to the target (cathode - negative electrode). Since the ions carry high energy, they can transfer their energy and knock out the target atoms, which are then deposited on the substrate arranged in the opposite direction. The ejected target atoms that have received energy from the ion bombardment, will deposit on the substrate with good adhesion and uniform stoichiometry. However, during the sputtering process, the plasma must be maintained in the chamber causing also some deposition of the gas atoms in the thin film. For electron beam evaporation, the electron beam emitted from a hot filament is directed to the target by a magnetic field. The electron beam heats up the target vaporizing atoms, which then precipitate on the substrate placed opposite to the target. For both techniques, the substrates are usually rotated for a uniform coverage and can be heated or tilted to obtain the desired deposition. Figure 3.13 illustrates the mechanisms of the sputtering and electron beam evaporation techniques.

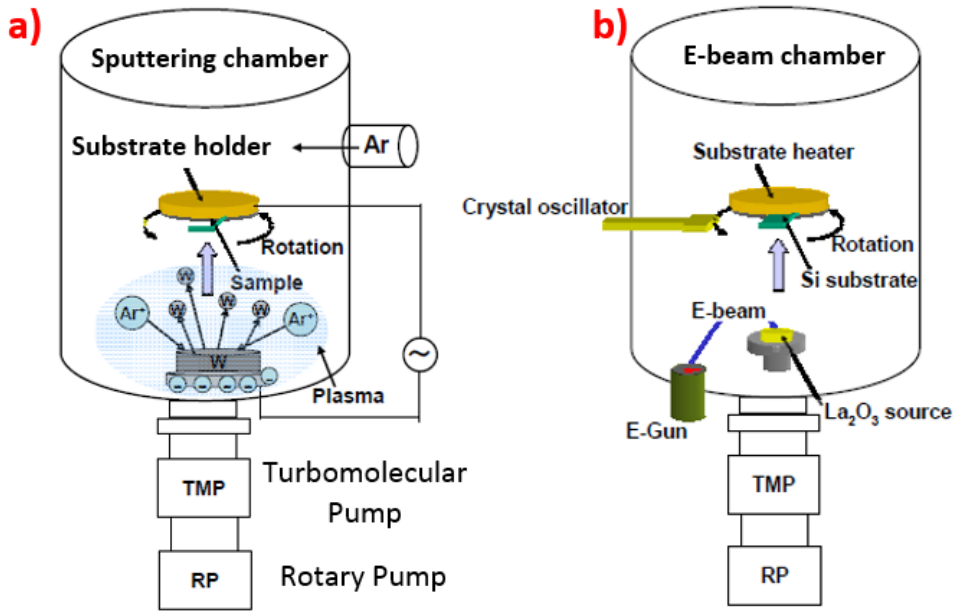

Figure 3.13: (**a**) Schematic illustration for W- deposition using sputtering technique. Ar plasma is excited and directed to make collision with a W target. W atoms are ejected from the target and sputter towards the rotating substrate for the deposition. (**b**) La_2O_3 deposition using electron beam evaporation technique. Ref [82].

❖ Some typical characteristics of sputtering and electron beam evaporation are listed in table 3.3.

Table 3.3: Typical characteristics of sputtering and electron beam evaporation technique

Sputtering	Evaporation
High energy atoms/ions (1-10 eV)	Low energy atoms (~ 0.1 eV)
Short mean free path of sputtered atoms	Long mean free path of evaporated atoms
Gas in thin film	Little gas in thin film
Small grain size	Large grain size
Good adhesion	Poor adhesion
Good step coverage	Poor coverage
Uniform deposition rate	Uniform deposition rate
Same stoichiometry	Poor stoichiometry
Expensive	Low cost

In this work, Al metal was deposited either by the sputtering technique for direct in-situ Joule heating experiments in the TEM (applied for the Al/Ge binary system) or electron beam evaporation for ex-situ RTA experiments (applied both for Al/Ge binary as well as Al/(Si-Ge)

ternary system). For both techniques, the pressure of the chamber is maintained at ~10^{-6} Torr before the Al metal deposition (high purity source, 99.995%). Figure 3.14 shows the SEM images of the 150 nm thick Al contacted n-doped Ge NWs on the 40 nm flat Si_3N_4 membrane. The bright markers are made of gold, used for the electron beam lithography alignment process. The exchange reaction between Ge and Al starts more easily if the Al is applied by sputtering, as will be shown in section 5.3 of chapter 5.

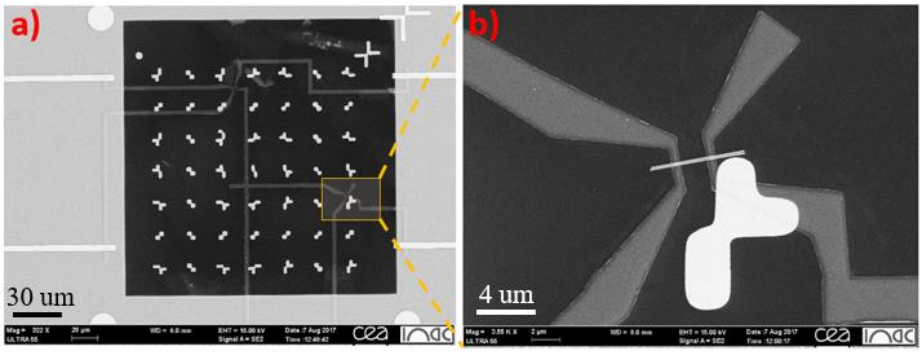

Figure 3.14: a) SEM image of the Al contacted n-doped Ge NWs on a 40 nm flat Si_3N_4 membrane and **b**) a zoom on the yellow rectangular box showing the Al pad contacted to the double Ge NWs.

3.7 Lift Off

After all above steps have been done, the sample is placed in acetone overnight to remove the unexposed photoresist. The micropipette is used to blow the solution gently on the surface of the membrane to assist lifting up the metal film. The sample can be checked with an optical microscope to be sure that the lift-off is complete. If there is any un-lifted metal part on the sample, sometimes it could be helped to use a sharp tweezer's tip for making a scratch on the remaining metal part and then gently blowing the acetone through the surface to remove the metal. The sample is then immersed in IPA for removing the residual acetone and dried by N_2 air flow.

3.8 Rapid Thermal Annealing (RTA)

Rapid thermal annealing (RTA) is a fast heating and cooling process used in semiconductor manufacturing for modifying the properties of the heated materials [84]. After RTA treatment, the dopants could be activated or have diffused through an interface or boundary. The structure could be relaxed or crystallized for amorphous materials. Normally high intensity lamps or lasers are used to raise the heating temperature controlled by a thermocouple or pyrometer. RTA can generate a heating temperature in the range of 200 to 1300 °C with typical ramp rates around 20 - 200 °C/sec

in an additional gas ambient control. Sophisticated multistage processes can be combined within one processing recipe. The temperature profile of the RTA process that was used is illustrated by the plot in figure 3.15.

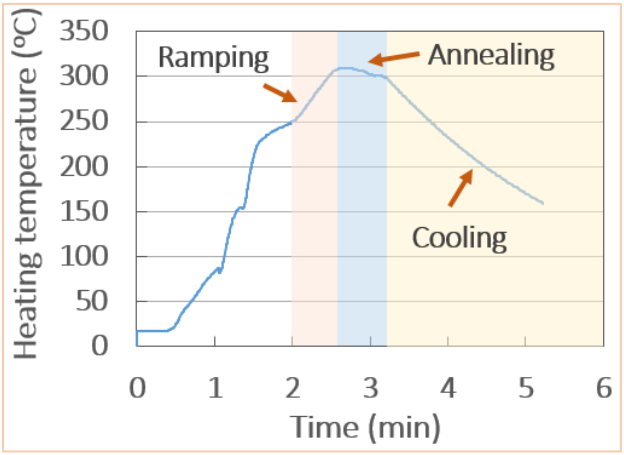

Figure 3.15: Illustration of the heating profile used in RTA.

As shown in the figure 3.15, the heating profile is divided into several steps. First the temperature is slowly increased from room temperature to a set temperature (i.e., 250 °C) in 2 min. Then the temperature is ramped linearly from 250 to 300 °C for 30 s. However, normally there is a spike at the end of the ramping step that the measured temperature is about 10 - 20 °C higher than the target value. The annealing temperature is then controlled via the thermocouple (or pyrometer) to lower the temperature down to the set point and maintain it constant during the annealing time. It is therefore worth noting that the real annealing time is longer than the setting value in the program. To finish the heating process, the temperature is linearly reduced back to room temperature in 4 min. In our experiments, the RTA was performed on the Jipelec™ JetFirst RTP Furnace [85] in BCAi Nano cleanroom, Grenoble INP. The images of the RTA machine and the sample holder are shown in figure 3.16. Particularly, the samples are installed in the middle of the two separated Si wafers. A high intensity lamp will heat up the top Si wafer while two thermal couples on the top and bottom will measure the temperature on the two Si wafers for a good control of the heating process. Meanwhile, N_2 gas is flowed through the chamber to prevent oxidation.

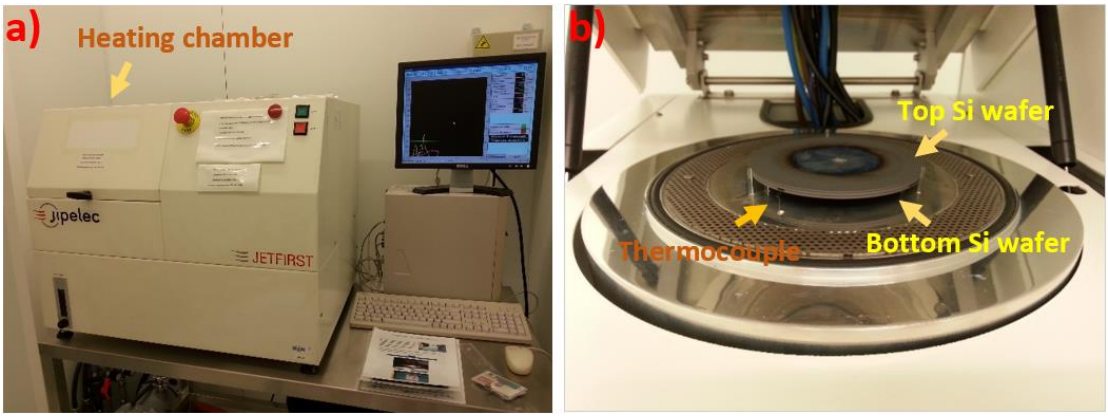

Figure 3.16: a) Images of the RTA machine used for the generation of metal/semiconductor thermal exchange. **b**) A zoom on the sample holder where the samples are installed in the middle of the two Si wafers. Thermal couples are used to measure and control the heating.

3.9 Electrical Measurement

In this PhD work, we also performed the IV characteristics measurement on the contacted Ge NWs and Si_xGe_{1-x} alloy NWs before and after the exchange reaction. The measured resistance was used to calculate the contact resistance at the created metal/semiconductor interface. These electrical experiments were performed on the four-point probe station in SiNaPS laboratory and CNRS/Institute NEEL.

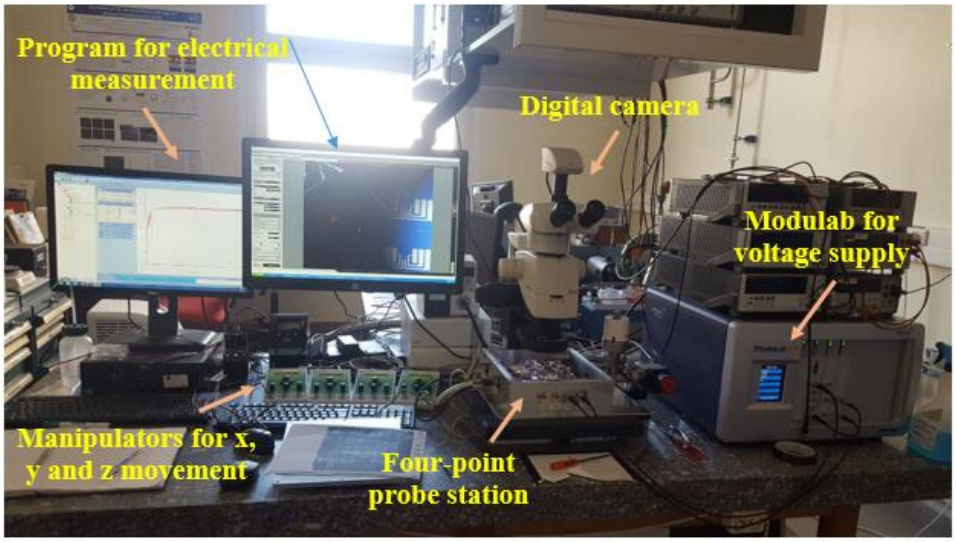

Figure 3.17: Image of the four-point probe station used for the electrical measurement located in CNRS/Institute NEEL.

3.10 Conclusion

In this chapter, we described all the processing steps to fabricate contacted NW structures compatible with TEM observation. In the next chapter, we will present the methodologies of the study, including the basic principles of different microscopy techniques (SEM and TEM) and the subsequent TEM based techniques for crystallographic and structural analyses such as geometrical phase analysis and energy dispersive X-ray spectroscopy.

Chapter 4

Electron Microscopy Techniques

Electron microscopy (EM) refers to all the imaging techniques that use electrons as illumination source to analyze objects. Starting in the early years of the 20th century, the development of electron microscopes has yielded a revolutionary imaging progress, which has beaten the spatial resolution of traditional light-based imaging devices. Nowadays electron microscopy becomes a crucial part of microstructure analysis with a wide range of applicable specimens such as inorganic, organic and biological objects, giving valuable atomic level information in crystallography, composition, energy levels or oxidation states [86].

In this PhD thesis, scanning electron microscopy (SEM) was used to image dispersed NWs on the Si_3N_4 membrane, for which Al contact patterns were designed and used for the electron beam lithography process. Fabricated devices were verified with the SEM for useful information of device quality and locations on Si_3N_4 membranes before proceeding with the TEM experiments. Importantly, the EDX quantification of Phosphorous dopants in Ge NWs was performed with the Ultra55 Zeiss SEM equipped with a FlatQuad 5060F annular detector, working at 4 kV. The SEM microscope is located in the nano characterization platform (PFNC) in CEA- Minatec, Grenoble.

(Scanning) Transmission Electron Microscopy (S)TEM was used for the structure and composition analyses of created heterostructures. The experiments with TEM operation mode were conducted on the conventional Philips CM300 microscope working at 100 kV in Institute Neel – Grenoble. STEM operation was done on a probe Cs corrected FEI Titan Themis microscope working at 200 kV, equipped with a SuperX – 4 (SDD) detectors for Energy Dispersive X-ray analysis (EDX). This microscope was also used for the in-situ heating experiments, providing real time observation at atomic level resolution. These experiments were performed at PFNC, CEA- Grenoble.

This chapter of the PhD thesis aims to describe the basic principles of the two microscopy techniques (SEM-TEM) and their interesting subsequent applications for structure and composition analyses: i.e., geometrical phase analysis (GPA), energy dispersive X-ray spectroscopy (EDX) and in-situ STEM heating.

4.1 Introduction

Stated by the Rayleigh criterion describing the minimum resolvable spatial resolution of any object, the image resolution δ is limited by diffraction and determined by the wavelength of the illumination source:

$$\delta = \frac{0.61\lambda}{\mu \sin \beta} \quad (5)$$

Where:

λ is the wavelength of the illumination source

μ is the refractive index of the medium with respect to free space

β is the semi angle of collection of the magnifying lens

$\mu.sin\beta$ is often called numerical aperture (NA) of the objective lens

If the optimum imaging condition is satisfied, the highest spatial resolution of a light microscope is about 0.61λ. Assuming a violet light source (the end of the light spectrum) that has a wavelength of 380 nm, the observed resolution is limited in the range of 200 nm.

Meanwhile, electrons characterized by the wave-particle duality, have the wavelength determined by the De Broglie equation (**6**):

$$\lambda = \frac{h}{p} = \frac{h}{\sqrt{2m_e E_b}} \quad (6)$$

Where:

h is Planck's constant (6.63×10^{-34} J.s in SI unit or 4. 136x10^{-15} eV.s)

m_e is the rest mass of the electron (9.1×10^{-31} kg)

E_b is the electron beam energy which is calculated by the multiplication of $q_e.U$ (U is the acceleration voltage of electrons).

Hence, if an electron is accelerated by an accelerating voltage of 200 kV, the relativistic electron wavelength is about 0.0025 nm, which is smaller than the atomic diameter of any element. Figure 4.1 demonstrates the observation limits of optical and electron microscopes.

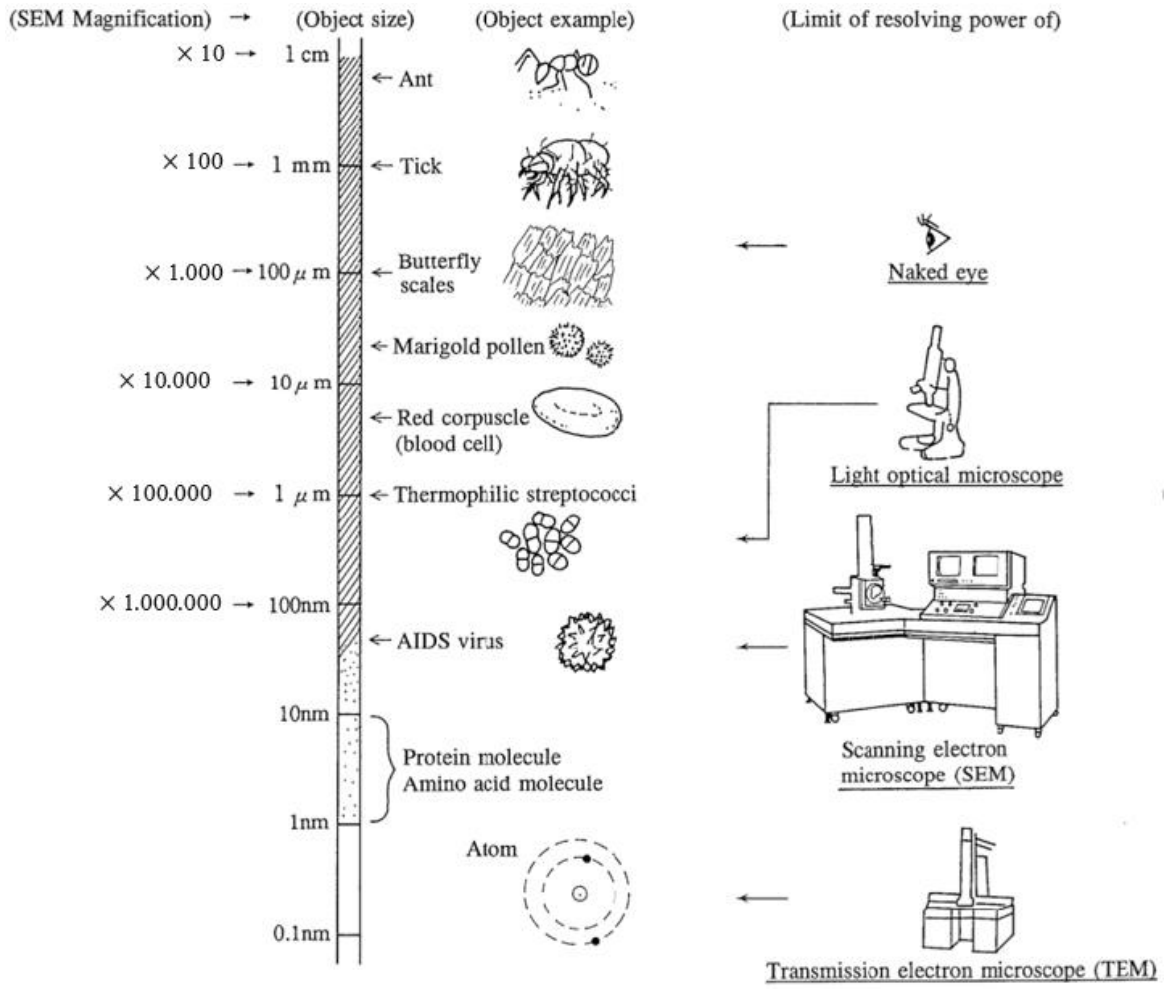

Figure 4.1: Schematic illustration of the resolution limits corresponding to human eyes, optical and electron microscopes. Ref [87].

Similar to optical microscopes, electron microscopes use lenses, but they are electromagnetic lenses (first developed by Hans Busch [88] in 1926) to control the pathway of the electron beam. The first transmission electron microscope was made by Knoll and Ruska [89] in 1931. A few years later, Siemens announced the first commercial transmission electron microscope [90] (TEM) in 1938. In 1965, Cambridge Instruments [91] delivered the first commercial scanning electron microscope with a resolution of about 20-25 nm. Nowadays, with the rapid development of modern technologies, electron microscopes become more and more powerful with supplementary imaging tools such as 4k high speed cameras, large area detectors for EDX like the Super X 4 detectors, etc.

Electrons interact with the specimen via elastic and inelastic interactions, giving off several signals that could be used as input for different analyses techniques. The following sections will discuss about the main principles and applications of two interesting electron microscopy techniques, i.e., scanning electron microscopy (SEM) and transmission electron microscopy (TEM).

4.2 Scanning Electron Microscopy (SEM)

SEM is the most used electron microscope for imaging and characterization of microstructure objects because of its high resolution (possible to achieve resolution better than 1 nanometer) and simple sample preparation process [90]. A wide range of materials from inorganic to biological objects could be used for imaging with flexible specimen size and thickness. SEM uses a focused electron beam scanning a 2D grid on the surface of the specimen. Signals emitted from the electron beam-specimen interactions are collected at different locations for different aims. The typical acceleration voltage of SEM is from 0.1 kV to 30 kV. The electron source is generated by a heated filament (LaB_6) or field emission gun (FEG) made of Tungsten (W), which normally gives better resolution than LaB_6. Figure 4.2 shows the main components of a SEM microscope including: an electron gun, a condenser lens, an objective lens, a scanning coil to adjust the beam positions, detectors and the pump system (vacuum level, about 10^{-6} Torr). The specimen is installed on a stage with movement capabilities such as horizontal movement (X, Y), vertical movement (Z), and specimen rotation (R) and tilt (T).

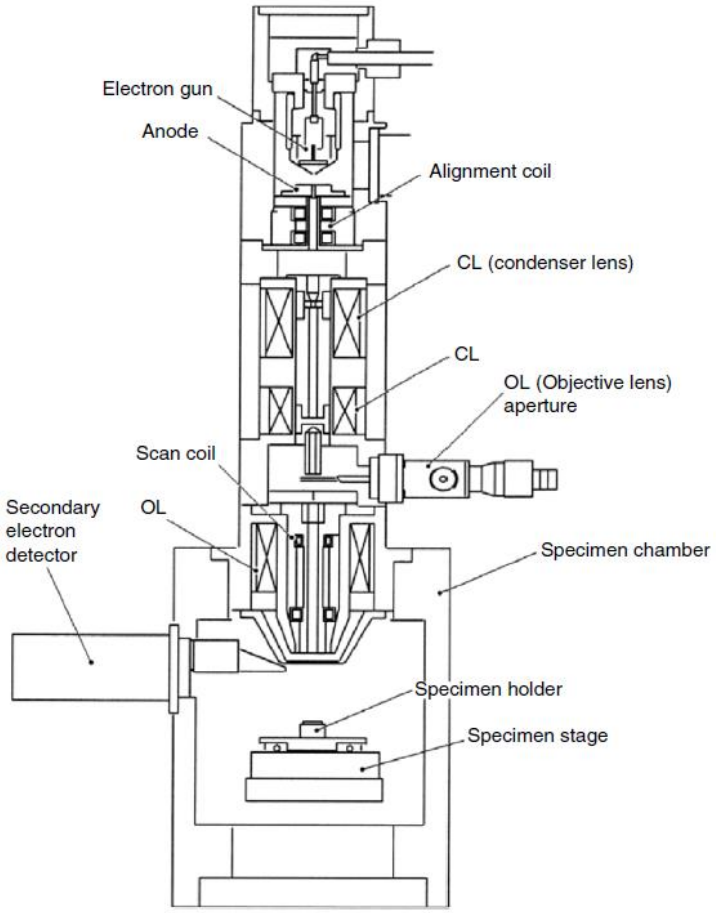

Figure 4.2: Schematic diagram of a scanning electron microscope (JSM—5410, courtesy of JEOL, USA). Ref [92].

In SEM imaging, there are two types of signals that are often used: i.e., (1) the secondary electrons (SE) emitted from the inelastic interaction between the primary electrons and the electrons on the outer shells of the specimen atoms, and (2) the backscattered electrons (BSE) bounced back from elastic interactions with specimen atoms. Depending on the acceleration voltage, electrons can penetrate at different depths in the specimen, generating numerous types of signals (shown in Fig. 4.3). Auger electrons are emitted electrons from inelastic interactions of primary electrons with the inner shell, and characteristic X-rays generated from the relaxation of electrons from high energy states to lower states. Both signals carry useful information of the specimen composition.

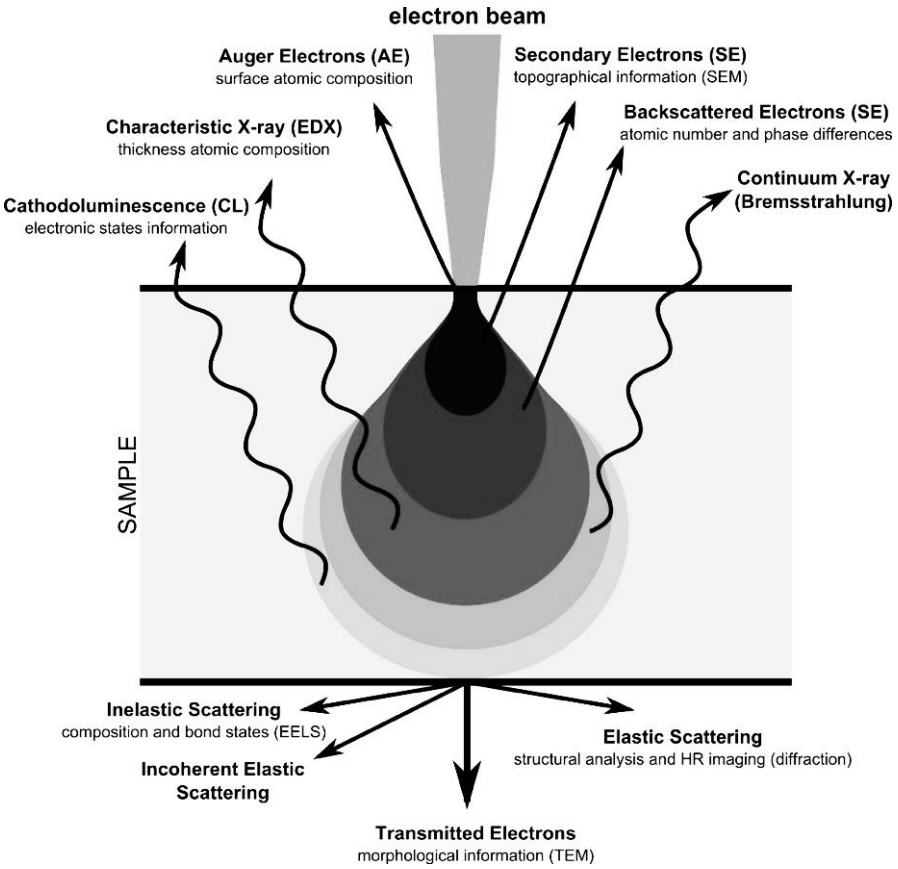

Figure 4.3: Electrons can interact with matter generating numerous signals in different pathways. Ref [93].

Not only providing good resolution, SEM images are also interesting for the large depth of field [87]. Meaning that specimen with different height features can be focused at the same time at different magnification, giving a good representation in 3D. This interesting characteristic is achieved by using a small objective aperture, leading to an electron beam with a small convergence angle. Moreover, the contrast in SE images can also give useful information about chemical composition and thickness of the specimen. Figure 4.4 shows the SE image of a fabricated Al metal contact on a Ge NW after being heated by RTA process. Since Au and Ge atoms are much heavier than Al atoms, they scatter more electrons resulting in the bright contrast. The white contrast on the edge of the Al electrodes is caused by a charging effect due to remaining PMMA resist.

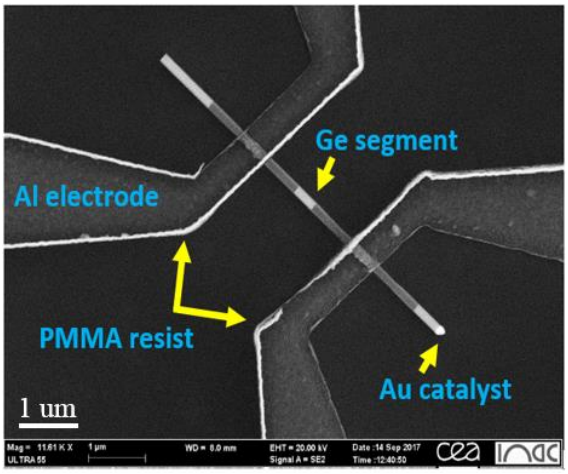

Figure 4.4: SEM image of the Al contacted Ge NW after being heated by RTA.

In general, the specimens prepared for the SEM are preferably conductive. This is because the primary electrons interact with the specimen and can cause charging effects by being absorbed or by emission of SE. If the specimen is nonconductive, the negative charges will add up to a certain level that could repel incoming electrons and lead to a distortion of the image. Normally, nonconductive samples should be coated by a thin layer of conducting materials, e.g., by flash evaporation of carbon wire or metal evaporation techniques. Moreover, a risk of deposition of contamination on the specimen is possible during the electron beam irradiation.

4.3 Transmission Electron Microscopy (TEM)

Transmission electron microscopy is the most preferable technique for atomic-scale structure analysis because of its sub- nm resolution [89]. In advanced TEM microscopes, several operation modes can be performed such as imaging mode, diffraction mode, microprobe/nanoprobe, nanobeam diffraction, convergent beam electron diffraction (CBED). Among these modes, conventional TEM and STEM imaging are the two main modes of operation. In the following sections, we will first present the typical configuration of a TEM microscope, which is a sophisticated system of multiple electrical components arranged within a compact column. The principles of TEM and STEM operation mode are explained in detail with a comparison giving the advantages and drawbacks of both techniques. After that, the process of in-situ heating experiments in (S)TEM environment will be presented that was used in this work for the initiation of a thermal exchange reaction between Al metal and semiconducting NWs. Finally, we will present the basic

theories of GPA and EDX techniques, which are used for a quantitative investigation of structure and composition of created devices.

4.3.1 Components

In order to obtain the optimum spatial resolution, the TEM microscope is packaged with several components in a closed column for maintaining a high vacuum working condition (for instant, 10^{-8} Torr in FEI Tian Themis microscope). Figure 4.5 demonstrates the order of the electrical components from the top to the bottom of the TEM microscope.

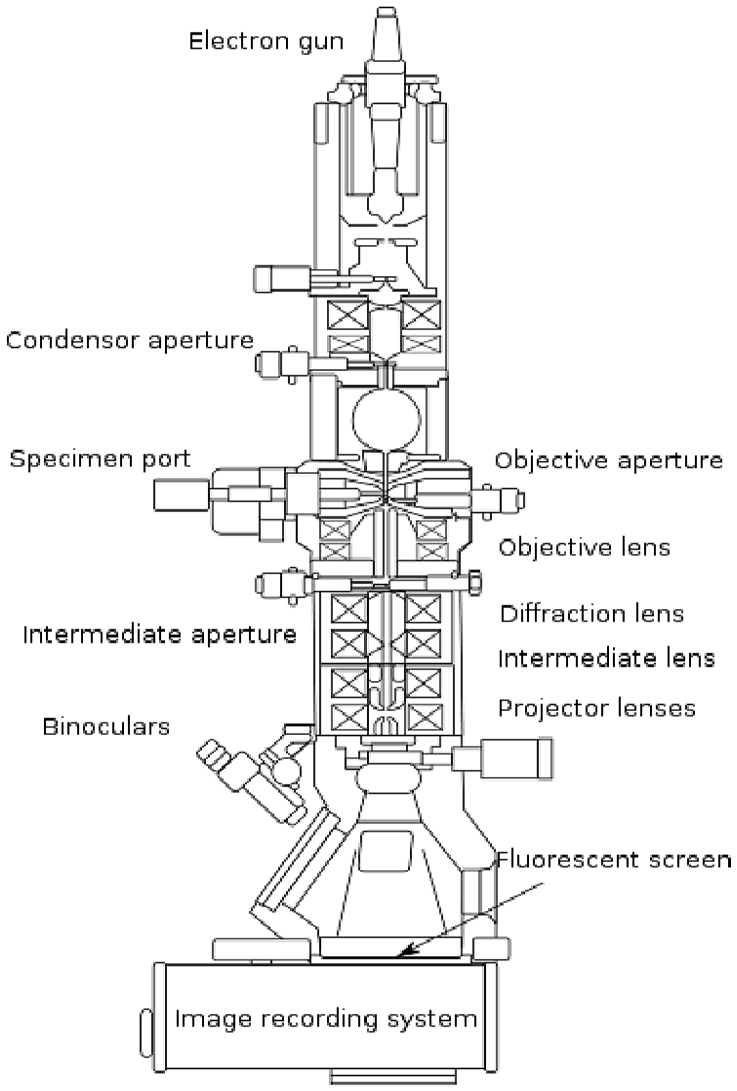

Figure 4.5: Schematic illustration of different components in a TEM microscope. Ref [94].

4.3.1.1 Electron Gun

The first component of every electron microscope is the gun, where the electron source is produced. There are two typical types of electron guns that are being used in most of the electron microscopes: i.e., thermionic gun and field emission gun (FEG). The characteristics of each type of gun are presented in table 4.1.

Table 4.1: Characteristics of thermionic gun and field emission gun (FEG) used for electron microscopes.

Type of eGun	**Thermionic**	**Thermionic**	**Field emission (FEG)**
Material	LaB_6 crystal	Twisted tungsten wire	Sharp W- tip
Vacuum required (Pa)	$\sim 10^{-5}$	$\sim 10^{-5}$	$\sim 10^{-8}$ Pa
Electrons generated by	Heated at high temperature	Heated at high temperature	Extracted by an electric field ($\sim 10^{9}$ V.m^{-1})
Advantages	Greater brightness than twisted tungsten wire	Low brightness	High brightness
Cost	Cost more than twisted tungsten wire	Very simple and inexpensive	Expensive
Gun image	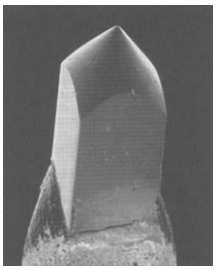		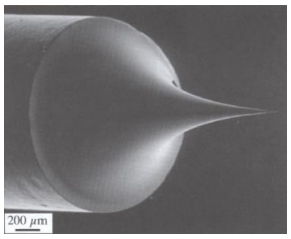

The principle of a FEG gun is presented in the schematic figure 4.6.

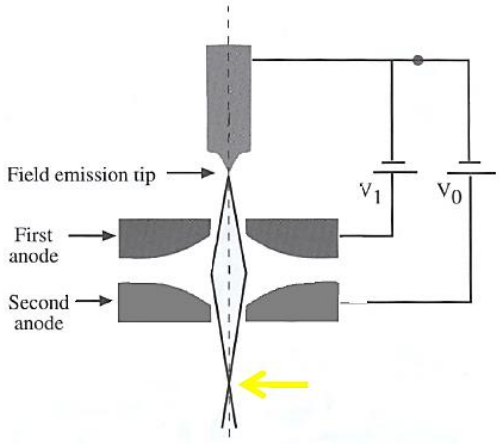

Figure 4.6: Schematic illustration for the working principle of the FEG gun. Ref [93].

As shown in the schematic, electrons are extracted from a sharp W- tip by an electric field (~10^9 $V.m^{-1}$) generated between the tip and the first anode (by an extraction voltage V_1). Then the electron beam is focused (forming a crossover) and accelerated by a second anode. The first crossover acts like a fine electron beam source.

4.3.1.2 Electromagnetic Lens and Apertures

The second part of the TEM is the arrangement of different electromagnetic lenses called condenser lens and objective lens. These electromagnetic lenses are made of metalic wires wrapped around a metallic core (as shown in Fig. 4.7a). The eletron paths will be controled by the applied current through these wires. Cooling water is flowing around the lens to remove the generated heat.

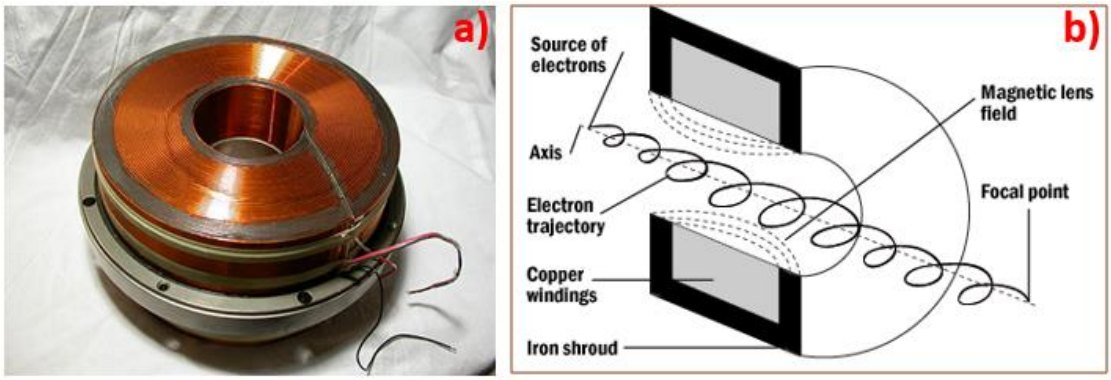

Figure 4.7: Image of electromagnetic lens (**a**) and the schematic illustration of the operation principles (**b**). Ref [93].

In advanced TEM microscopes, normally there are three condenser lenses named C1, C2 and C3.

- The first condenser C1 is used to collect all the electron rays from the source and make the first crossover between C1 and C2. In the TEM microscope, the strength of C1 is manipulated by changing the spot size.
- The second condenser lens C2 is designed to collect electron rays at certain directions to make a parallel beam at the output in TEM mode or a convergent beam in STEM mode. The strength of this lens is adjusted by the intensity knob or "brightness" knob.
- The condenser C3 is the last condenser lens in some microscopes, often combined with the C2 to control the convergence angle of the beam on the sample.

The objective lens is the most important lens in every microscope. The objective lens encloses the specimen with an upper and lower objective polepiece. In advanced microscopes, the condenser lens C3 is coupled with the upper part of the objective lens, used to focus the beam for a fine probe or to switch between microprobe/nanoprobe. The lower part is used to focus the exit beam creating a diffraction pattern (DP) in its back focal plane and an image in its image plane. The strength of this lens is controlled by the defocus knob.

For each electromagnetic lens, there will be a coresponding aperture to limit the collection angle of the electron beam. The aperture is usually an annular metallic plate (made of Pt or Mo) [93].

- The condense aperture C2 is used to shape and adjust the beam intensity on the specimen.
- The objective aperture is after the specimen, 50 μm above the lower pole piece of the objective lens. The objective aperture is normally placed in the back focal plane to select a certain region of reciprocal space. In imaging mode the aperture can be "on" or "off" the optical axis of the transmitted electron beam for taking the bright field (BF) or dark field (DF) images.
- A selective area aperture can also be inserted in the image plane to select the area of the specimen used for diffraction analysis. This aperture also helps to reduce the diffraction intensity avoiding the saturation of the camera.

4.3.1.3 Deflection Coils

Deflection coils are installed at different parts of the column, used to deflect the electron beam during the alignment process. A deflection coil is composed of several coils arranged in such a way that the generated magnetic field (the induced Lorentz force) can deflect the electron beam in a controlled manner as presented in the figure 4.8a-b. The double deflection coils are used for the beam shift and beam tilt manipulation, without causing a shift in the image (making the beam focus at the pivot point, Fig. 4.8c).

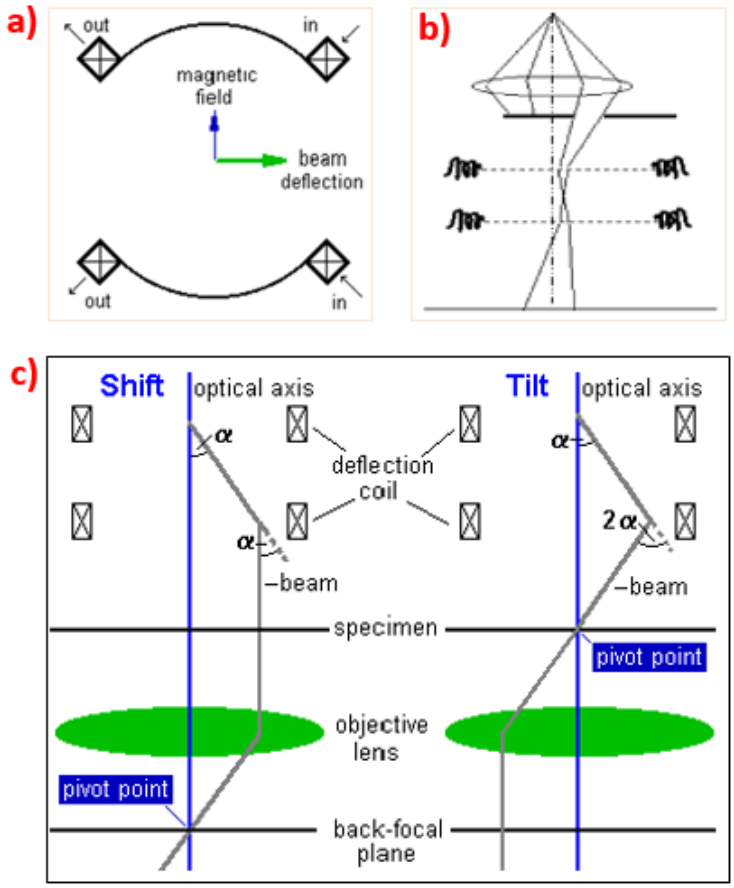

Figure 4.8: (**a-b**) schematic illustration of a deflection coil configuration used for the deflection of the electron beam. **c**) Combination of double deflection coils for the beam shift and beam tilt manipulation. Ref [93].

4.3.1.4 TEM Holder and Compustage

The TEM holder is used to transfer the specimen from outside to inside the TEM column. The TEM holder has two parts separated by the O ring (shown in Fig. 3.9). The specimen is installed at the extremity of the inner part of the TEM holder, which is designed for a single tilt (α tilt) or double tilt (α and β tilt) of the specimen. The holder is then inserted in the TEM column via the Compustage, which gives the α tilt about the holder axis. β tilt can be operated by connecting a cable from the holder to the TEM, that reads the values of the motor present in the black part on the left (in Fig. 4.9). The Compustage has a mechanical system that provides the (X-Y) and Z movement of the TEM holder. It is also designed to let the TEM holder being inserted without breaking the vacuum in the column.

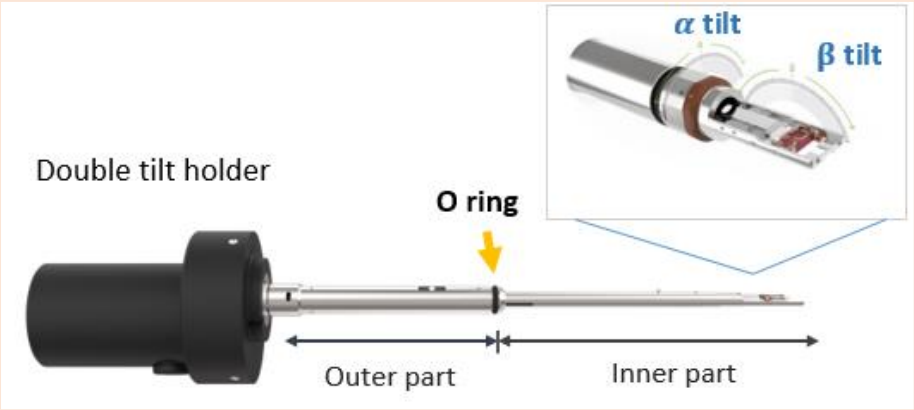

Figure 4.9: TEM double tilt holder from DENSsolutions company designed for in-situ heating. Ref [22].

There are several types of TEM holders for advanced microscopy such as Cryo-TEM holders with liquid nitrogen cooling, in-situ heating holders or tomography holders with the possibility to have full 360-degree rotation for the 3D structure reconstruction.

In this work, we have used an ultra-Narrow gap Fischione tomography sample holder for EDX analyses. This holder provides a wide solid angle for characteristic X-ray collection and a possibility of retracting the specimen into the body of the specimen holder. The image of the holder is presented in figure 4.10.

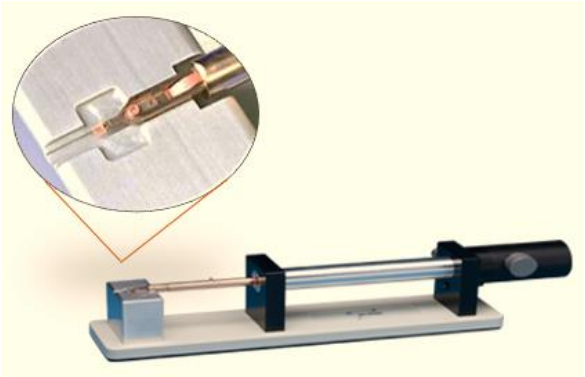

Figure 4.10: Image of Fischione Model 2030 Ultra-Narrow Gap Tomography Holder.

For the in-situ heating experiments, we have used the DENSsolutions heating sample holder with six contacts. The image of the holder is shown in the figure 4.11. The top part of the holder contains a β tilt mechanical system connected with the Compustage via the outer cable, which allows to tilt the specimen 30 degree in β direction. The membrane chip is inserted in the rectangular gap (indicated by the red arrow), which has a window for the electron transmission. Besides, 6 interconnecting electrodes are placed on top of the membrane chip for the external electrical connection.

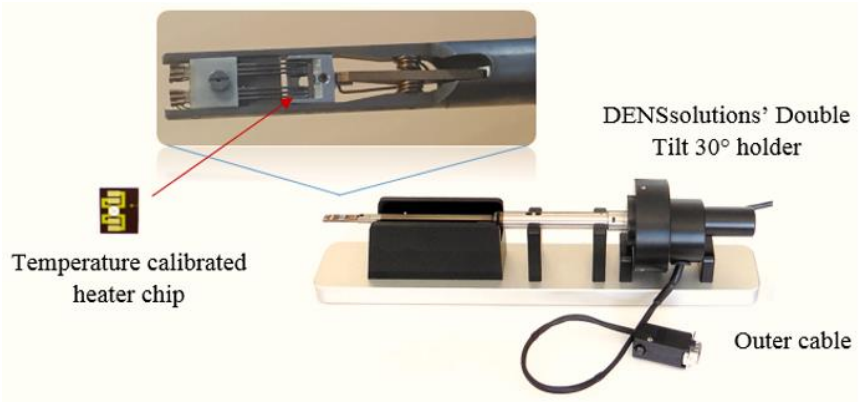

Figure 4.11: Image of DENSsolutions sample heating holder.

4.3.1.5 Diffraction Lens and Projection System

Below the objective aperture is the system of intermediate lenses (diffraction lens) and projector lenses. The intermediate lens is right below the objective lens, used to switch between the imaging mode and diffraction mode. In diffraction mode often a beam stop is inserted to cover the center spot in the DP, avoiding the exposure of the camera to the direct beam. The projection

system is used to magnify the image or DP by changing the camera length. The image or DP will be then captured by the (CCD) camera and displayed on the computer screen.

4.3.1.6 Fluorescence Screen and CCD Cameras

A global observation of the image can be done on the fluorescent screen, below the projection system at the end of the TEM column. The screen is coated with doped ZnS to emit green light (550 nm) when hit by electrons. A small binocular attached with a little fluorescent screen is used for looking at small features. In TEM mode, the fluorescent screen should be lifted up to make the BF or DF images on a recording device. In the old versions of TEM microscopes, the TEM images were captured by film that was replaced later by CCD cameras. These are now starting to be replaced by CMOS cameras for higher efficiency. Because of the heat generation, the camera is often cooled down to reduce the noise and increase the detection quantum efficiency.

4.3.1.7 Vacuum System and Cold Trap

The vacuum system is an essential part of the TEM microscope. First the gun system requires an ultra-high vacuum level to prevent the generation of an electrical arc in the anodes. In the column, the vacuum is indispensable to avoid collisions between the fast electrons and air molecules. Along the TEM column, there are several pumps installed at different locations such as the ion pump used for the electron gun, the turbo-pump for the projection system, the pre-vacuum pump for the loadlock to transfer the specimen from air into the TEM column, etc. In practice, the tubo-pump should be turned off during the investigation since it often generates strong vibrations. Furthermore, to reduce contamination during the TEM observation, a Cold trap is often used, which is a metallic piece placed close to the specimen and connected with a Dewar holding liquid nitrogen for cooling down the temperature.

4.3.2 TEM-STEM Mode

TEM and STEM operation modes can provide images with atomic level resolution. However, each technique has its advantages and disadvantages that should be considered for an appropriate analysis. In practice, STEM mode is often preferable because it offers a direct interpretation by the Z-contrast and the ability to couple with other (analytical) techniques like EDX and electron energy loss spectroscopy (EELS) for chemical analysis.

4.3.2.1 TEM Mode

In TEM mode, a large area of the specimen is irradiated by a nearly parallel electron beam. Hence the electron beam energy is spread uniformly on the illuminated surface. The specimen can therefore be less damaged by the high energy beam. TEM techniques are normally used to investigate low atomic number elements such as carbon or biologic objects. The principle of conventional TEM mode and switch between image and diffraction mode is described in the schematic figure 4.12.

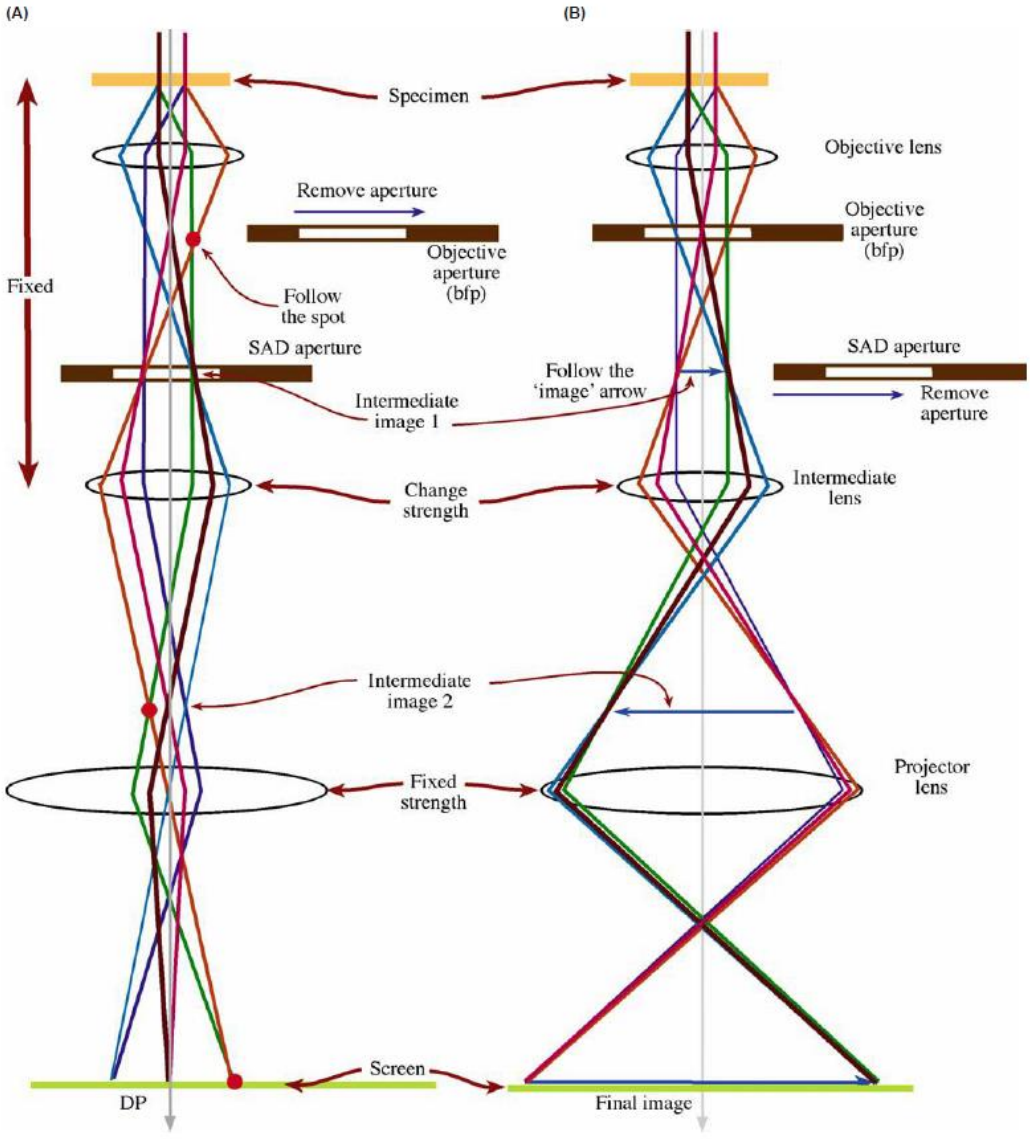

Figure 4.12: (**a**) diffraction mode and (**b**) imaging mode in conventional TEM microscope. Ref [93].

The diffraction mode and imaging mode are the two common operations in a TEM microscope. As shown in the figure 4.12, the parallel beam interacts with the specimen and is focused by an objective lens. In the diffraction mode, the objective aperture is removed and the selective area aperture (SA) will be inserted in the image plane. Then the intermediate lens will be adjusted to project the diffraction pattern (DP) from the back focal plane onto the fluorescent screen or the camera. In the image mode, an objective aperture can be inserted in the back focal plane and meanwhile, the SA is removed to obtain an image of the specimen. Instead of the DP, the intermediate lens will select the image plane as an object and project it on the fluorescent screen or the CCD camera.

TEM images can be bright field (BF, when the direct beam is used to form the image) or dark field (DF, when diffracted beams are used to form the image), which are captured by the camera at the end of the TEM column. As demonstrated from the name, in the BF images, the background (or vacuum) will turn white while the features appear darker. In the DF images, the objective aperture is placed in the back focal plane of the objective lens to block the transmitted beam while allowing diffracted beams at high scattering angle to contribute to the image. Therefore, in DF images, the background appears dark while the features become white.

When passing through the specimen, the electron beams can experience multiple diffractions within the crystal lattices, resulting in diffraction contrast. The objective aperture can be positioned to allow both the transmitted and diffracted beams to contribute to the image. Then, an interference pattern can be formed resulting in a high resolution (HR)TEM image (phase contrast). The resolution of the image is crucially determined by the objective lens, which is generally not 100% perfect. Therefore, the image suffers from different aberrations and the strongest aberration is called “spherical aberration – C_s”. Normally a specific current is applied to the objective lens to partly compensate the aberration (Scherzer defocus). In general, TEM images of crystalline specimens are difficult to interpret as the contrast depends on multiple factors such as electron wavelength, specimen thickness and orientation, the defocus and the spherical aberration C_s. Hence it is difficult to interpret the TEM contrast if the experimental conditions are unknown. A simulation step is often needed to allow full interpretation of the TEM image.

4.3.2.2 STEM Mode

In STEM mode, a small probe will scan pixel by pixel on the specimen surface, and the image is constructed respecting the scanning positions in the raster integrating a signal on a detector, similar to SEM. Depending on the probe size (normally a few angstroms or nanometers), the spatial resolution of the image will be affected accordingly. Detectors are placed below the specimen to collect the scattered electrons at different angles to form the image. The HAADF detector is often used in STEM since it collects scattered electrons at high angle (50-250 mRad, shown in Fig. 4.13). These electrons are scattered via elastic interactions with the specimen atoms. Therefore, they are very sensitive to the atomic number of the elements (Z- contrast). However, in HAADF STEM images, due to the low collected signal (<10%), the images can be noisier and often distorted due to the drift of the specimen during image acquisition. The principle of STEM mode and the different detectors are presented in the schematic below.

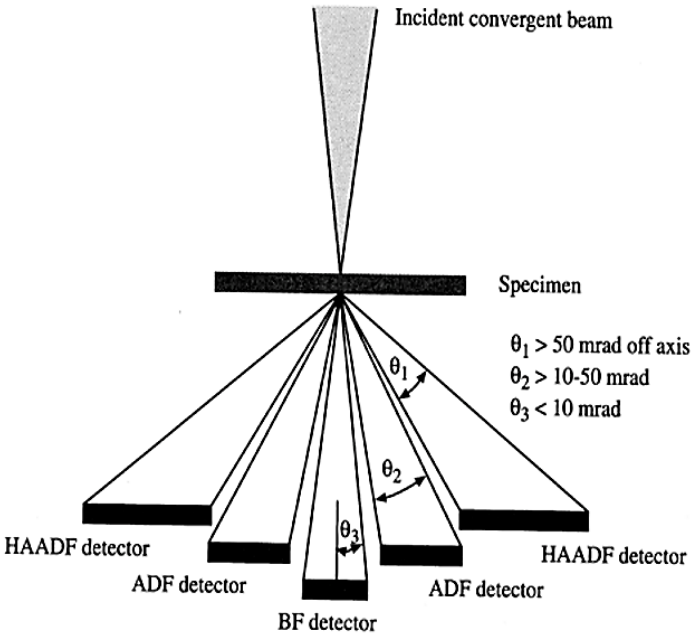

Figure 4.13: Demonstration of collecting angles for different detectors used in STEM mode. Ref [93].

Figure 4.14 shows the BF and HAADF images of the Al thermal diffusion in an Al_2O_3 passivated Ge nanowire after RTA. As shown in the images, the HAADF image gives very good contrast between Ge and Al regions, although they are also well visible in BF STEM in this particular example.

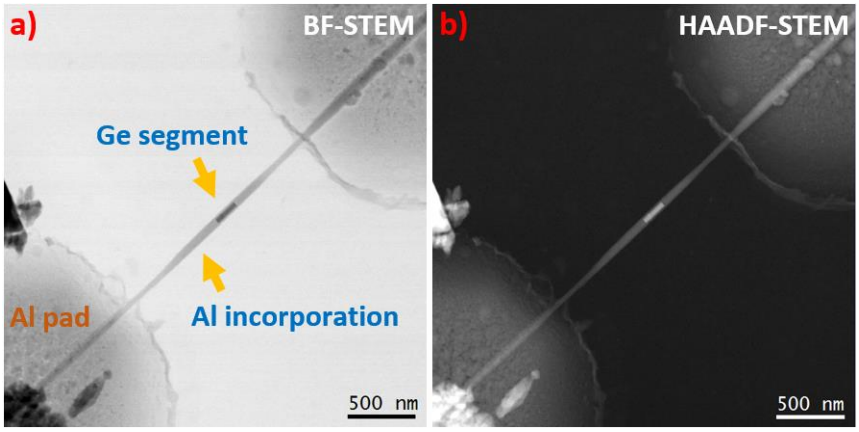

Figure 4.14: BF - STEM and HAADF - STEM images of the Al thermal diffusion in an Al_2O_3 passivated Ge nanowire after RTA.

The STEM resolution is determined by the convergent beam and the probe aberration (C_s). The stationary convergent beam generates a transmitted disk, called Ronchigram. The schematic of the Ronchigram formation is presented in figure 4.15.

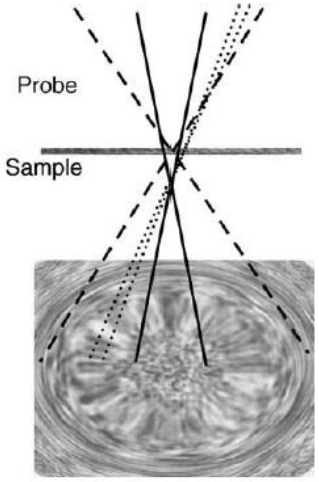

Figure 4.15: Schematic drawing of the Ronchigram formation at under-focus. Ref [95].

To optimize the resolution, it is necessary to bring the beam to the focus so that the magnification becomes infinity as shown in figure 4.16. The inner ring should appear homogeneous without any phase change. This process can be done on an amorphous specimen as there will be no alignment preference of the specimen atoms. If there is any stigmatism on the lenses, the Ronchigram will show a distortion and phase changes in the center.

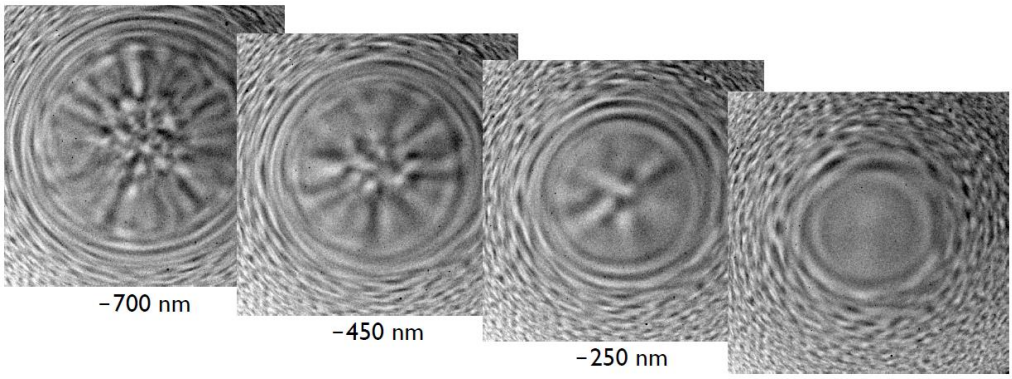

Figure 4.16: Ronchigrams at different defocus values, going to infinite magnification. Ref [95].

4.4 In-situ (S)TEM Heating Techniques

In traditional ex-situ heating experiments, the specimen will be inserted and heated in a heating oven with a pre-set heating procedure. Only information of the initial and final state of the specimen are recorded while the evolution process is missing. Therefore, in-situ heating experiments are more preferable for the real time observation of the process. In this work, the heating experiments were performed in the TEM microscopes, which provides a high vacuum environment for the metal/semiconductor exchange reaction and a good resolution for the real time observation. The heating temperature is generated by two different techniques: i.e., using direct Joule heating and temperature calibrated heater chips from DENSsolutions company.

4.4.1 Direct Joule Heating Method

Joule heating (or Ohmic heating) is the effect when a current passes through a resistant material, transferring the energy to the atoms via collisions and generating heat. In practice, Joule heating has been used for many daily applications like filaments in light bulbs or heating ovens. In electronic devices, however this phenomenon is unwanted since it causes a loss in terms of energy. In our experiments, Joule heating effect is applied to heat a local region around the Al contact pad and semiconductor NWs (shown in Fig. 4.17).

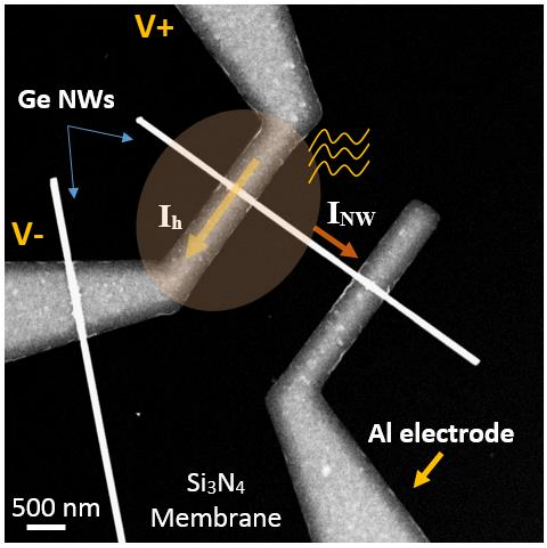

Figure 4.17: STEM image of the Al contacted Ge NWs for direct Joule heating technique.

As shown in the figure, the NW is contacted at the center of a thin rectangular 500 nm x 5 µm Al bar of 200 nm thickness. Both sides of the Al bar are connected with larger Al metal strips (3 µm width) for connecting to the outer electrical circuit. When a bias potential is applied at the two sides of the thin Al strip (with symmetrically positive and negative voltage), electrons will move from V- to V+ (the current direction will be reversed) and make collisions with Al atoms. Due to the narrowing of the Al electrode, the current density is increased at the thin Al strip, resulting in a locally heated region. A clear description of direct Joule heating technique is presented in the work of Mongillo et al [23]. However, the temperature distribution in this region is not uniform and un-calibrated. In our experiments, when the applied voltage was about 0.7 V (the heating current I_h = 2.7 mA), we observed the propagation of Al metal into the Ge NW. Similar ex-situ heating experiments were done via RTA, where the propagation started above 300 ^oC. Therefore, we can find from correlation that the temperature range generated in the in-situ Joule heating is around 300 ^oC. A main drawback of this heating technique is that with high applied current, the heating electrode can damage or melt, resulting in the cut of the electrical heating current. During the direct Joule heating experiments, we have observed the formation of Al islands and voids on the heating electrodes (shown in Fig. 4.18). This is due to the electro-migration effect as the flowing of the electrons pushes Al atoms in a certain direction and piles up to form islands. More details of the mechanism is explained in the paper of Kondo et al [96].

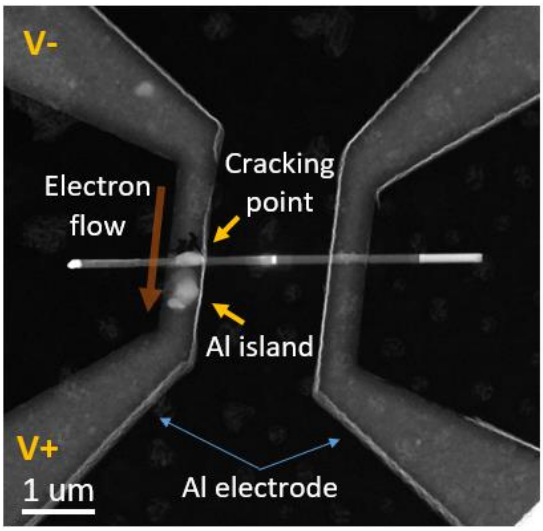

Figure 4.18: HAADF STEM image of fabricated device after being heated by direct Joule heating technique.

The electrical connections for these in-situ experiments are described in figure 4.19. A cable from the sample holder connects to an inter-connect box with one co-ax connection for each electrical contact on the sample holder, that can be connected to the electrical setup. For these experiments we used two 2401 Keithley sourcemeters and a 6485 Picoammeter for the voltage supply and the measurement of the current through the contacted NW, respectively. The experiment was monitored by a heating program installed on a laptop. The interconnect box as well as the electrical equipment was common grounded to the ground of the TEM.

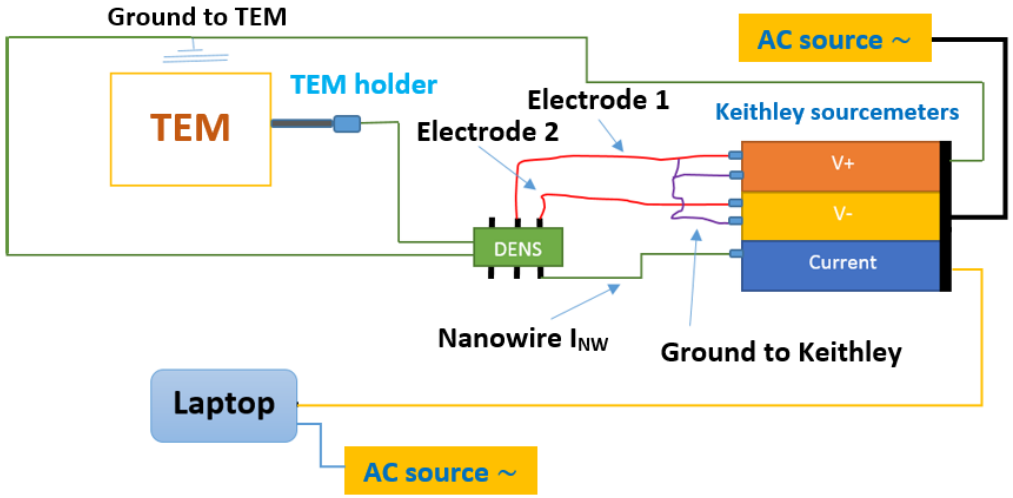

Figure 4.19: Diagram for the electrical connection in the direct Joule heating experiment.

4.4.2 Temperature Calibrated Heater Chip

Since the direct Joule heating technique is un-calibrated in temperature and cannot generate a sufficiently high heating temperature, we have also fabricated our devices on the calibrated heater chip from DENSSolution company [22] for calibrated annealing experiments (see the Fig. 4.20). The advantage of the heater chip is the temperature calibration and the possibility to raise the heating temperature up to 1300 ^{o}C within a short time.

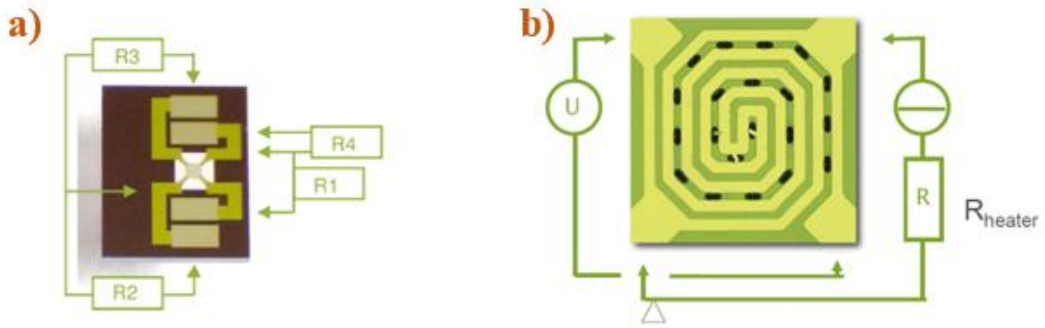

Figure 4.20: (**a**) Commercialized temperature calibrated heater TEM chip from DENSsolutions company. The heater chip consists of 4 heater electrodes with two electrodes for conducting a heating current and two other electrodes for measuring the generated voltage for the calibration. (**b**) A zoom on the electron transparent window shows a configuration of a metallic spiral embedded in the SiN_x membrane with several 6 µm x 23 µm holes. The specimens are contacted over the holes for the TEM investigation.

The heater chip is composed of a 200 nm thick electron transparent SiN_x membrane in the center of the chip and 4 outer electrodes for applying heating voltage (current). A Mo or Pt spiral with well-designed dimensions is buried in the middle of the SiN_x membrane for the Joule heating effect. There are several holes on the membrane, where the NWs are contacted for the TEM observation. The heater chip is then inserted into the TEM DENS holder for the in-situ heating experiment. The diagram for the electrical connection is presented in figure 4.21. The TEM DENS holder is first connected to the interconnect box and then to the electrical control box for the conversion from AC to DC current. The heating process is monitored via the heating program provided by DENSsolutions (Digiheater), installed on a laptop. The electrical setup is connected to the ground of the TEM, using a metal part of the TEM, which are all connected to the same common ground.

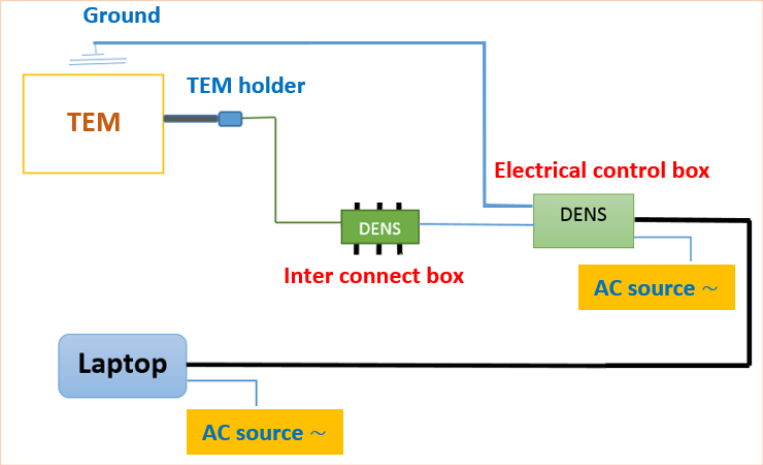

Figure 4.21: Schematic illustration of the electrical connection for the heating experiment with Commercialized temperature calibrated heater TEM chip from DENSsolutions company.

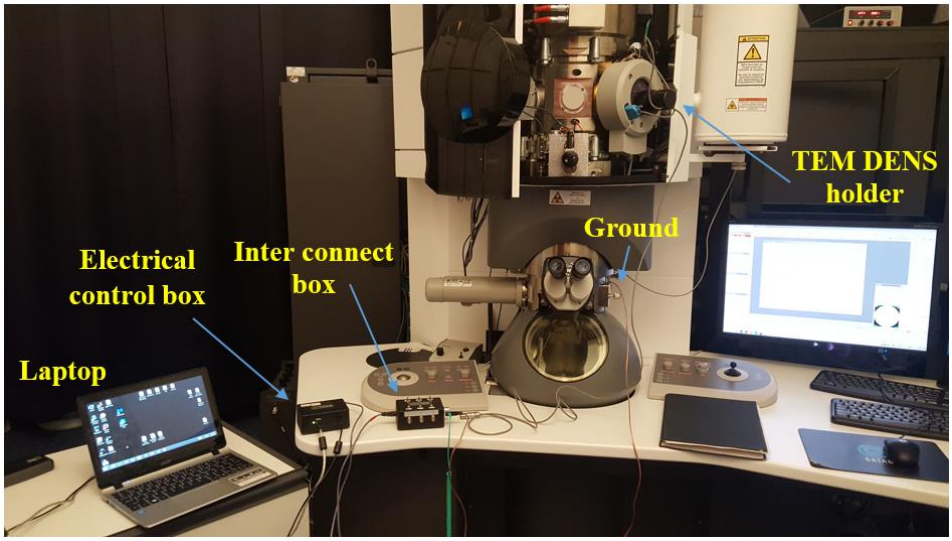

Figure 4.22: Set up for in-situ STEM heating using DENS TEM double tilt holder.

4.5 Geometrical Phase Analysis (GPA)

GPA is a TEM based technique that uses the reciprocal space Fourier transform (FT) of a HR-(S)TEM image to determine the change and shift in lattice fringes with high precision. The technique is based on the geometrical phase algorithms first reported by M. J. Hÿtch in 1998 [97]. A HR-(S)TEM image can be considered as the superposition of several sets of lattice fringes. Each particular set of fringes will contribute to a component (pixel) in FT. Hence, by analyzing the amplitude and the phase of the components individually, it is possible to retrieve quantitative information of the structure periodicities, deformation or strain mapping in the lattice.

❖ Basic steps of GPA analysis:

a) Taking a HR (S)TEM image
b) Perform the FT on the calibrated HR image and select a $\vec{g}$ vector on the FT
c) Extract the amplitude and phase from the $\vec{g}$ vector
d) Removing of scan noise and correcting the phase jump
e) Generation of d-spacing, 2D deformation and rotation map

In the frame of this thesis, the GPA analysis was performed using digital micrograph with the script written by Rouvière, J. L [98]. The technique was used to determine the lattice spacing of the Si rich region in the created heterostructures when studying Al thermal incorporation in Si_xGe_{1-x} alloy NWs.

4.6 Quantitative EDX: Compositional Analysis of Created Heterostructures

Energy Dispersive X-ray spectroscopy (EDX) is a preferable technique for compositional analysis, thanks to its quantitative and fast performance [93]. The technique is based on the identification and quantification of the characteristic X-rays emitted from the inelastic interactions between the focused electron beam and specimen atoms. Elements with the atomic number higher than 4 (Be) can be detected using EDX technique. The specimen prepared for EDX analysis is not restricted in the size and shape. However, to be precise in the quantification, the specimen should be flat for a better determination of the absorption and also conductive to reduce the charging effect. Nowadays, the EDX technique is widely used in microstructure analysis for chemical mapping (with color code presentations) and also the possibility to perform 3D reconstruction of the specimen.

In this PhD thesis, the measurement of phosphorous dopant in Ge NWs was performed in the SEM/EDX Zeiss 55 Ultra microscope, which is equipped with a FlatQuad 5060F annular detector, working at 4 kV. Besides, quantitative EDX is applied for the determination of Al, Si and Ge concentration in the created heterostructures from Al thermal propagation in Si_xGe_{1-x} alloy NWs. For these experiments, EDX data is collected on the probe Cs corrected FEI Titan Themis microscope working at 200 kV, equipped with the SuperX: 4 (SDD) detectors.

4.6.1 Background

In the widely accepted Rutherford - Bohr model [99], atoms are described by the planetary model, which has a positive nucleus consisting of protons (Z number) and neutrons, and different orbiting electron shells associated with fixed energy levels. Electrons in the inner shell (with the smallest orbiting radius) are attracted by the nucleus, and therefore have the highest bonding energy. The outer shell electrons, with lower bonding energies due to the increase in the orbiting radius, are more easily removed from the atoms when sufficient ionization energy is provided. Each electron shell is named by an alphabet character, starting from K (n=1), L(n=2), M (n=3), N(n=4), O(n=5), etc. Furthermore, each shell is divided into several subshells where corresponding electrons have slightly different energies.

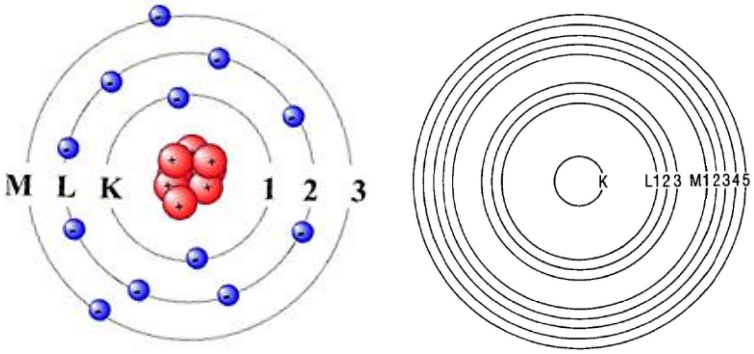

Figure 4.23: Bohr model of magnesium atom (**left**) and number of subshells corresponding to the K, L and M shell (**right**). Adapted from ref [100].

If the irradiated electrons carry higher energy than the inner shell electrons, they can knock out the electrons and generate vacancies. Outer shell electrons at higher energy levels will jump into the vacancies to reduce the energy and release photons (named as characteristic X-rays). The characteristic X-rays will carry an energy level relevant to the difference between the two orbitals. Therefore, characteristic X-rays can be used to identify elements since the orbital energy levels of a specific element is distinct from other elements. Figure 4.24 shows the schematic illustration of the interaction between the primary electrons and the specimen atom.

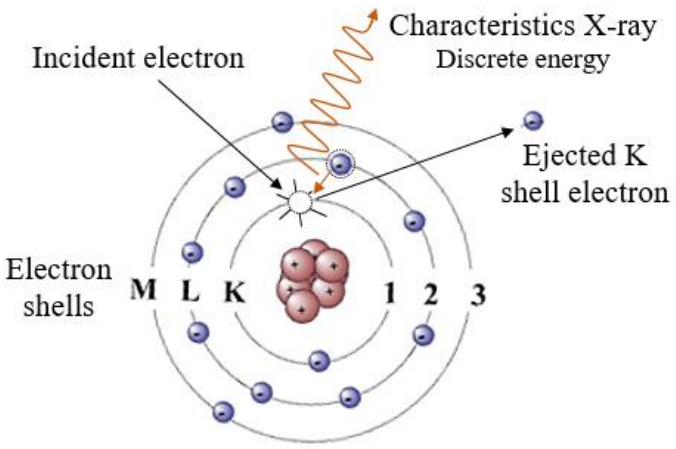

Figure 4.24: Schematic illustration of forming characteristic X-ray $\mathbf{K}_{\alpha}$ in a magnesium atom. Ref [100].

In most of the microscopes, characteristic X-rays are detected by the traditional Si(Li) detectors or Si drift detectors (SDDs). The SDDs have more advantages than Si(Li) detectors due to their high throughput of counts and reduced cooling needs while maintaining energy resolutions competitive with Si(Li) detectors [93]. The working principle of a SDD is that incoming characteristic X-rays hit the p-doped Si surface layer of the detector and generate electron-hole pairs. These electrons are collected by a high potential and their energies are amplified by a Pulse processor. Then the electrons are sorted to the energy channels (10-20 eV wide) by a multi-channel analyzer and the plot of the X-ray counts versus the energy is made of the complete spectrum of the analyzed specimen. To increase the efficiency of the detection, the detectors are placed as closed as possible to the specimen to increase the collection angle as much as possible. In advanced microscopes, 2 or 4 SDDs are arranged around the incident electron beam above the specimen to increase the number of counts. Besides, the specimen can be tilted towards the detector to increase the X-rays collection.

Energy resolution is an important factor of any detector. It is defined as the full width of the peak at half maximum height (FWHM). In practice, the energy resolution is broadened by the electrical system (noise). Poor energy resolution results in an overlap between energy levels of analyzed elements such as unresolved Si($K_{\alpha} = 1.740\ keV$) and W($M_{\alpha} = 1.775\ keV$). Typically, the Si(Li) detectors can give a resolution of 140 eV at Mn (K_{α}). SDDs can achieve better resolutions around 121 eV with the Peltier cooling (-25 °C). Moreover, another important characteristic of the detector is the time response or 'dead time', which is the time that the detector stops counting X-rays but

processes the previous count. If two X-rays arrive below the dead time, then the detector will sum up their energies to generate a "sum peak". Moreover, as shown in the figure 4.3, the interaction of the electrons with the specimen atoms also releases a continuous X-ray spectrum or "continuum". This background spectrum ranges from the zero-energy peak to the maximum energy E_0 of the primary electrons and superimposes with the characteristic X-rays. In addition, signals can also come from the instrument such as the Cu peak from the TEM grid, Al peak from the metal contact to the detector crystal, Si peak from the crystal dead layer, and escape peaks from the Si crystal K X-ray.

4.6.2 Quantitative Analysis

EDX is considered as a fast-qualitative compositional analysis since the acquisition time for collecting a chemical map (with a spectrum at each scan position) is a couple of minutes (depending on map and pixel size and other factors). However, for a quantitative analysis, the mapping process must be performed as long as possible to gain enough statistics of counts for a good precision. Increasing the beam current can help to raise the number of X-ray emissions, however the specimen can be seriously damaged resulting in a change in structure or morphology. Moreover, the absorption of large numbers of electrons in the specimen can result in a charging effect, causing drift of the specimen. From literature, there are several methods for the quantification of specimen composition based on the X-ray intensity analysis.

4.6.2.1 K- ratio Method by Raimond Castaing.

In 1951, Castaing proposed the "*K*-ratio" method for the determination of the composition for the same element in the unknown and in a standard of known composition based on the ratio of the measured characteristic X-ray intensities [101]. This method was developed for massive specimens where the X-ray collection was obtained on the same instrument, under the same operating conditions. Neglecting the presence of absorption and secondary fluorescence, the ratio of the weight fraction between an unknown element within the specimen and a standard sample element can be approximated by equation (**7**):

$$C_i^{unk} \approx \frac{I_i^{unk}}{I_i^{std}} C_i^{std} = K_i C_i^{std} \qquad (7)$$

Where C_i, I_i, and K_i is the weight fraction, X-ray intensity and "K ratio" of the subscript **i** element. Therefore, if we measure the X-ray intensities of both the standard and unknown sample in the

same microscope, we could roughly estimate the concentration of the element **i** in the unknown sample.

In practice, however, the X-rays produced within the material will be generated in all directions, and partially absorbed when passing through the substance. Figure 4.25a shows the geometry of the X-ray absorption in a substance when being irradiated by an electron beam. Generated X-rays need to pass through a distance of $z\,\mathrm{cosec}\psi$ (where ψ is the takeoff angle) before reaching the spectrometer. Moreover, the X-ray production within the material is not homogeneous, but varies with the penetration depth z and material density ρ as shown in figure 4.25b.

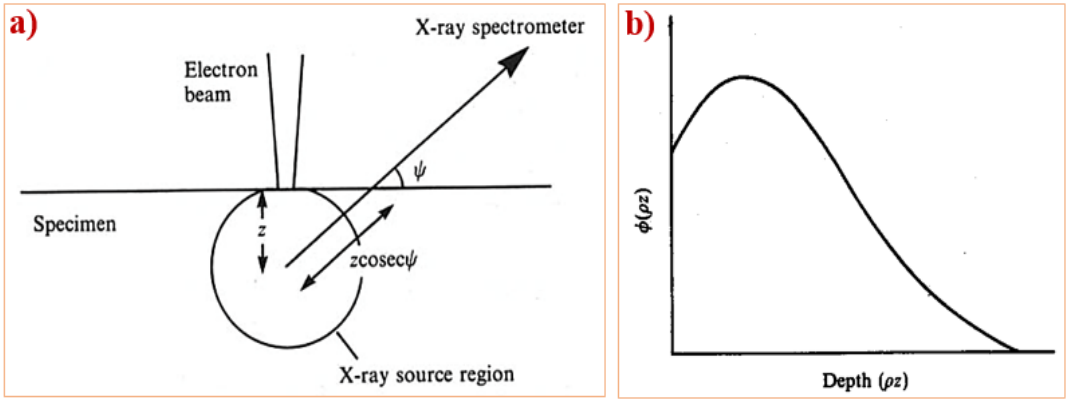

Figure 4.25: (**a)** Geometry of the X-ray absorption in a substance when being irradiated by an electron beam and (**b**) X-ray distribution as a function of depth z. $\boldsymbol{\rho}$ is the material density (g/cm^3). Ref [102]

Therefore, in order to precisely correct the X-ray absorption (**A**), the X-ray distribution function (**ϕ**) should be incorporated. In fact, this function is influenced by several parameters such as the accelerating voltage ($\mathbf{E_0}$), critical excitation energy of a particular element line ($\mathbf{E_c}$) and mean atomic mass number (**Z)** of the material. The general behavior for the influence of these parameters to the X-ray absorption can be demonstrated in figure 4.26a-c.

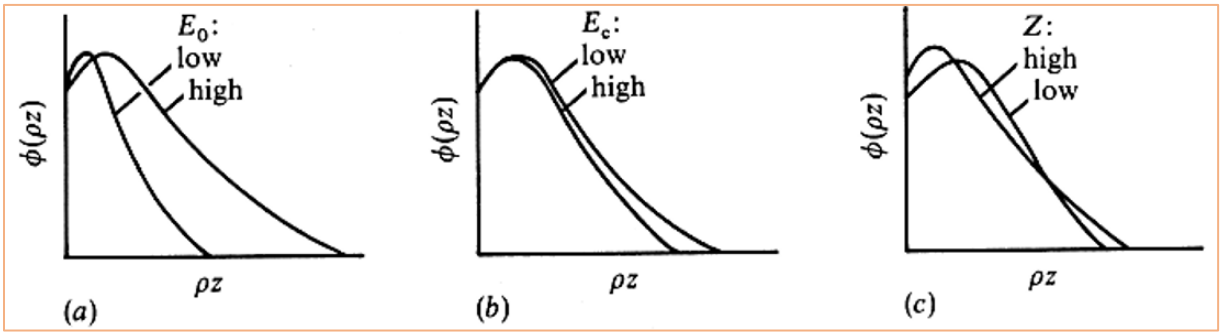

Figure 4.26: Influence of the accelerating voltage (E_0), critical excitation energy of a particular element line (E_c) and mean atomic mass number (Z) of the material to the X-ray absorption. Ref [102]

Besides, when the characteristic X-ray has an energy greater than the absorption edge energy of other elements present in the specimen, it can again excite these low ionization energy elements and generate secondary fluorescence (**F**). For all these phenomena, the **ZAF** correction method [103] was proposed to calculate separately each component for a correct determination of the composition. The equation (**7**) can be rewritten as:

$$C_i^{unk} = \frac{I_i^{unk}}{I_i^{std}} \frac{ZAF_i^{unk}}{ZAF_i^{std}} C_i^{std} \qquad (\mathbf{8})$$

4.6.2.2 Cliff and Lorimer Ratio Method

To overcome the limitations of the K-ratio method, Cliff and Lorimer developed the new method, named "Cliff-Lorimer ratio method" [104], which does not require a standard sample. This method is intentionally applied for thin specimen. Assume that the specimen is a binary system of element A and B, the k-ratio could be directly related to the X-ray intensities of the two elements by the equation (**9** and **10**):

$$\frac{C_A}{C_B} = k_{AB} \frac{I_A}{I_B} \quad \text{and} \quad C_A + C_B = 1 \qquad (\mathbf{9\text{-}10})$$

Here, k_{AB} depends only on the microscope setup and the acceleration voltage (kV). k_{AB} could be experimentally measured with a known standard (normally Si or Fe) if the specimen contains the standard element. In case the specimen is different from the standard, k_{AB} could be roughly equal to the ratio of k_{ASi} / k_{BSi}. Moreover, k_{AB} can be also theoretically calculated using the proposed equation of Goldstein et al [93]. However, the error of the concentration determination can be up to 20%.

$$k_{AB} = \frac{(Q\omega a)_B A_A}{(Q\omega a)_A A_B} \frac{\varepsilon_A}{\varepsilon_B} \qquad (\mathbf{11})$$

Where: Q is the ionization cross-section

ω is the fluorescence yield

a is the relative transition probability

A is the atomic weight

ε is the detector efficiency

Indeed, the ionization cross-section Q is not well known resulting in the uncertainty of the calculation.

4.6.2.3 Zeta Factor Method

In this PhD work, we use the zeta factor method proposed by Watanabe et al [105] to quantify the composition of the formed structures. In this method, the specimen thickness at each individual analysis point is produced simultaneously with composition. Therefore, no prior knowledge of the sample thickness is required. The absorption is corrected based on the measured specimen thickness, which gives a better precision. Assuming that the characteristic X-ray intensity is proportional to the mass thickness of the specimen (ρt) and the composition (C_A in wt.%). Therefore, the relation of the mass thickness (ρt), the beam current and the composition of element A can be expressed as:

$$\rho t = \zeta_A \frac{I_A}{C_A D_e} \quad \text{and} \quad D_e = N_e I_b \tau \qquad (\mathbf{12 - 13})$$

Where: ζ_A is called zeta factor

D_e is the total electron dose during the acquisition time ($D_e = N_e I_b \tau$)

N_e is the number of electrons per unit charge (in Ampere)

I_b is the beam current (in Ampere)

τ is the acquisition time

From the theoretical calculation of Armigliato [105], the X-ray intensity can be approximated by the equation (**14**):

$$I_A = N_v \frac{Q_A \omega_A a_A}{M_A} C_A \rho t D_e (\frac{\Omega}{4\pi}) \varepsilon_A \quad \textbf{(14)}$$

Where: N_v is Avogadre's number, Q_A is the ionization cross-section,

ω is the fluorescence yield, a is the relative transition probability of the X-ray line,

M_A is the atomic weight, ε is the detector efficiency at this energy

$\frac{\Omega}{4\pi}$ is the detector collection angle in the whole space

Therefore, we can extract ζ_A from equation (**12**) and (**14**):

$$\zeta_A = \frac{M_A}{N_v Q_A \omega_A (\frac{\Omega}{4\pi}) \varepsilon_A} \quad \textbf{(15)}$$

The equation (**15**) allows us to calculate the zeta factor for specific elements from the instrumental set up. However, a larger error can be added up due to the uncertainty of several components. In our work, to improve the precision of the quantification, the zeta factor corresponding to each analyzed element was measured experimentally on a standard sample using equation (**12**), where the zeta factor value is determined by the slope on the plot of the mass thickness ρt and $\frac{I_A A_A}{C_A D_e}$.

Here the absorption term A_A is added to the nominator to correct the collected X-ray intensity I_A, which will be discussed in equation (**21**).

Similarly, we apply for the element B,

$$\rho t = \zeta_B \frac{I_B}{C_B D_e} \quad \textbf{(16)}$$

Assume that the total concentration in the specimen $C_A + C_B = 1$, then we can determine the three unknowns C_A, C_B and ρt by the three equations:

$$C_A = \frac{\zeta_A I_A}{\zeta_A I_A + \zeta_B I_B}, \; C_B = \frac{\zeta_B I_B}{\zeta_A I_A + \zeta_B I_B}, \; \rho t = \zeta_A I_A + \zeta_B I_B \quad \textbf{(17-19)}$$

Moreover, if we know the density of the specimen ρ, it is possible to extract the thickness of the specimen t. Normally, the specimen density can be calculated by the equation:

$$\frac{1}{\rho} = \sum \frac{C_i}{\rho_i} \quad \textbf{(20)}$$

Here, we haven't considered the absorption. The absorption of a single X-ray can be calculated by equation (**21**) given by Philibert [105]:

$$A_A = \frac{(\mu/\rho)_{sp}^{A} \rho t \operatorname{cosec}\psi}{1-\exp\left[-(\mu/\rho)_{sp}^{A} \rho t \operatorname{cosec}\psi\right]} \qquad (\mathbf{21})$$

Where: $(\mu/\rho)_{sp}^{A}$ is the mass absorption coefficient of the specimen for element A and Ψ is the X-ray take-off angle.

Therefore, the collected characteristic X-ray intensity is the multiple of generated characteristic X-rays I_A and the absorption coefficient A_A. Finally, if we substitute equation (**20**) into equation (**17-19**), we get:

$$\rho t = \sum_{j}^{N} \frac{\zeta_j I_j A_j}{D_e}, \quad C_A = \frac{\zeta_A I_A A_A}{\sum_{j}^{N} \zeta_j I_j A_j}, \ldots, C_N = \frac{\zeta_N I_N A_N}{\sum_{j}^{N} \zeta_j I_j A_j} \qquad (\mathbf{22})$$

The equation (**22**) will be valid as long as the total composition $\sum C_N = 1$.

4.6.3 3D Reconstruction

The EDX hyper-map is the 2D projection of the specimen composition with respect to the detector position. Since the mass thickness, composition and absorption coefficient of the specimen at a particular analysis point could be deduced from the zeta factor method, it is possible to reconstruct the specimen in 3D based on fitting of the experimental results with a model. Particularly, for a NW system, the 3D reconstruction can be done by integrating several ellipses whose dimensions (major and minor axis), positions and rotation are adjusted to a respective center. A detailed description of this method is presented in reference [106]. In the following some basic steps of the reconstruction are described:

a) A representative cross-sectional model based on the structure properties of the NW is assigned for the reconstruction. Typically, elliptic, rectangular or hexagonal shapes are chosen as they are the usual shapes of NWs.
b) Calculating the first cross-sectional model with the thickness obtained from the zeta factor method.

c) Varying the number of ellipses, dimensions, positions and rotations based on the concentration profiles.
d) Recalculate the local concentration and ellipse dimensions by minimizing the difference between the experimental concentration profile and the calculated profile.

In this PhD thesis, the 3D reconstruction is applied for the Al/SiGe ternary system. As Al atoms thermally exchange with Si and Ge atoms within the NW, several thin layers of Si, Ge, Al_2O_3 and SiO_2 have been observed by EDX analysis. Therefore, a 3D reconstruction of the formed structure will be useful for a better understanding of the kinetics of the exchange reaction.

Chapter 5

Solid-State Reaction of Al/Ge Binary System

In this chapter, the study of the thermally induced solid state reaction of the Al /Ge binary system will be presented in detail. The exchange reactions were either initiated by ex-situ heating via RTA or in-situ heating using direct joule heating technique described in section 3.8 and 4.4.1, respectively.

The first part of this chapter will briefly summarize recent knowledge on the thermal exchange reaction of the Al/Ge couple. Then we elaborate the reasons for choosing Al metal as a diffusion source both to elucidate the kinetics of metal/Ge thermal exchange reaction and also to examine the hypothesis of dopant "pile up" at the Ge/Al reaction interface.

In the second part, real time (S)TEM observations of the Al/Ge exchange are presented from the initial stage to the end of the of the protruding process, where a sub- 10 nm Ge quantum dot was created. We demonstrate that a drawback of the direct Joule heating method is that it can damage the contact electrodes. Therefore, a complementary RTA treatment is proposed for the reliability of the fabrication process. During the metal/semiconductor exchange reaction, the electron beam radiation, the NW surface quality and diameter have been found to influence the diffusion rate/behavior. Importantly, step-wise growth of the Al/Ge reaction interface is attributed to NW surface roughness.

In the third part, we present electrical measurements on several doped and un-doped Ge segment lengths to elucidate the formed Al/Ge contact resistance and the capacity of conducting high current densities. These electrical measurements were conducted manually using the Keithley sourcemeters "set up" as presented in section 4.5.

Finally, we present the measurements of dopant redistribution in propagated Al/Ge NWs, which aim to clarify the hypothesis of dopant "pile up" effect in Ge. Quantitative EDX analyses were performed on a SEM/EDX equipped with a FlatQuad 5060F annular detector at the PFNC, CEA-Grenoble.

In this chapter, the specimens investigated in section 5.8 were prepared by Dr. Masiar Sistani, TU-Wien, Austria. Particularly, Ge NWs with a 20 nm passivated Al_2O_3 shell were contacted by Al pads on both sides and being annealed during several time intervals to achieve a short Ge segment length (from 200 to 550 nm).

The experimental result presented in section 5.5 was reported in the paper of El Hajraoui et al [13], where we show an ambiguous influence of the NW diameter on the propagation rate of the Al/Ge reaction interface.

5.1 Background

In the last couple of years, thermally assisted metal diffusion in semiconductor NWs (Si, Ge, GaAs, etc.) has been attracting a considerable interest due to great benefits of low dimensional confinement and possibilities of producing ultra-scaled devices below the spatial dimensions of traditional electron beam lithography process [26–28]. To study the formation of metal/germanium contacts, there are several reports on the phase formation of Pt - Ge [26], Ni - Ge [41], Cu - Ge [31,107], Mn - Ge [34] couples, etc. Depending on the annealing temperature and metal, the protruding of metals in Ge NWs can result in the formation of intermetallic phases, which may improve the contact quality of the metal/semiconductor contacts. In addition to incorporating the intermetallic phase from both sides of the NW, it is possible to narrow the semiconducting channel for the production of ultra-short semiconducting channel devices. However, the potential presence of several phases in the intermetallic crystal structure also yields a complication of property control and reliability. Among metal resources, the Al/Ge system in NWs appears very promising since, in contrast to other metal-semiconductor combinations, no intermetallic phase is formed and a pure monocrystalline Al NW is created with a very sharp interface with the remaining Ge NW. Moreover, the combination of the intrinsically strong spin−orbit coupling in Ge and the superconducting properties of Al make this system a promising platform to study hybrid superconductor-semiconductor devices that could be potential building blocks for superconducting quantum interference devices (SQUIDs) [12]. It is reported in the literature that Al has a low solubility limit in Ge, and vice versa [108]. An Al-Ge phase diagram is presented in figure 5.1, the couple forms a simple eutectic at 420 ^{o}C. The melting point of Al and Ge is 660 ^{o}C and 940 ^{o}C, respectively. At the eutectic temperature, this phase diagram predicts that about 5.2% of Ge atoms can be soluble in the Al matrix while that is 1.82% of Al in Ge. Moreover, metastable phases ($Al_{70}Ge_{30}$ and $Al_{60}Ge_{40}$ alloy) with rhombohedral crystal structure can be made and coexist using a mechanical alloying technique [109].

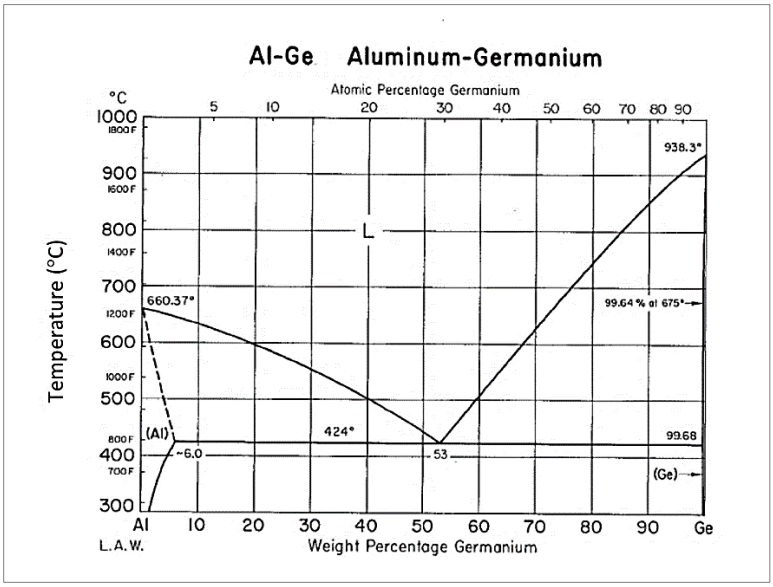

Figure 5.1: Al-Ge phase diagram. Ref [110].

It has been reported in the study of Sebastian Kral [44], that the thermal reaction of the Al/Ge couple can only occur above 327 ^{o}C. Electrical measurements on the Al/Ge interfaces show the formation of a Schottky contact. Besides, by ex-situ consecutive heating (RTA) at the same condition, a linear dependence of Al propagating length on the heating time has been observed. Also in Kral's study, he shows a plot of the Al reacted length versus the NW diameter. While this plot is characterized by a lot of scatter, it may indicate a dependence of the length of the created Al region with the NW diameter. A sophisticated study of the Al /Ge thermal exchange kinetics has been reported by Khalil El Hajraoui [13], in which he showed that the intrusion of Al in Ge NWs will result in the formation of a monocrystalline Al core with face-centered cubic (FCC) structure. The pure Al core is surrounded by a thin pure Ge (~2 nm), Al_2O_3 (~3 nm), and Ge containing Al_2O_3 (~1 nm) layer, respectively. Combining kinetic studies of the reaction interface with three dimensional chemical modelling, he proposes a surface diffusion mechanism in the Al/Ge binary nanowire system where Ge atoms diffuse through a surface diffusion channel on the created Al NW into the Al contact pad, while Al atoms are supplied to the reaction interface by Al self-diffusion and exchange with Ge atoms at the interface. The electrical and optical transport properties of ultra-scaled Al/Ge/Al heterostructures were elucidated in the work of Sistani et al [15] and Staudinger et al [16], where they showed quantum ballistic transport as well as quantum ballistic photo-detection at room temperature. The same exchange reaction was also used to obtain

a monocrystalline Al NW via the complete replacement of Ge by Al by Florian M Brunbauer [111]. Here he shows a remarkable capacity of the created Al NW of withstanding a current density as high as 1.78×10^{12} A.m^{-2}. The above results were ex-situ (RTA) or in-situ studies with relatively low spatial resolution.

In this PhD, we continue to elucidate the thermal diffusion behaviors of Al/Ge binary system for a further understanding of the contact formation and a fine manipulation of the growth rate. In-situ heating experiments were carried out on different TEM microscopes, offering a good resolution for observing the exchange reaction at atomic scales. Several factors such as Al/Ge contact quality, NW diameter, surface roughness and electron beam radiation were studied. Optimizing all influencing parameters for an atomically precise control of the Al/Ge interface, we have successfully produced a sub- 10 nm Ge QD. Moreover, we performed a verification of a dopant 'pile up' hypothesis, which speculated that a locally increased doping concentration may be present at the Al/Ge interface, as the dopants would be pushed forwards by the advancing reaction interface [112]. Such a dopant pile-up effect is expected to decrease the contact resistance and may produce Ohmic contacts.

5.2 Experimental

For the experiments, we used single-crystalline Ge NWs synthesized via the VLS process by the chemical vapor deposition method (CVD) with gold catalyst on (111) germanium substrate. The NWs grow in the <111> direction. GeH_4 gas was used as the precursor for the nanowire growth. The typical diameter of as-synthesized Ge nanowires varies around 100 – 150 nm with 8 μm length. The nanowires were intentionally doped with Phosphorous at 7 x 10^{19} atoms/cm^3. Since doping are relatively low concentrations, a doping of 7 x 10^{19} atoms/cm^3 corresponds to roughly 0.16%, we do not expect an influence on the Al exchange reaction speed or behavior. In our experiments, as grown Ge NWs were either being used as-grown with an applied metal contact or the native GeO_2 shell formed due to the exposure of the NWs to the atmosphere was first removed by dipping in diluted hydriodic acid (HI acid, >57%, Sigma-Aldrich -MERCK) with deionized water (DI) with ratio 1:3 for 5 s and immediately coated with 5 nm of Al_2O_3 by atomic layer deposition (ALD) at 250 ^oC to protect them from oxidation and improve the surface quality. To fabricate the metal contacts, the NWs were first diluted in ethanol solution by sonication and dispersed on electron transparent 40 nm Si_3N_4 membranes by drop casting. The membrane

fabrication has been described elsewhere [76]. SEM images of Ge NWs were taken for NW selection and designing the electrodes. Selected single or double Ge NWs were contacted by a pair of parallel Al rectangular bars so that the contacted NWs should be located near the center of each bar. Practically, for a good coverage of the NW surface, the optimized sizes of Al heating electrodes are about 500 nm in width, 3 µm in length and 150 nm in thickness. The two ends of each Al bar were connected to Ti/Pt electrodes, patterned in a prior lithography step. The contact between the large Pt electrodes on the Si_3N_4 chip and the electrical setup was made by small metal tips of a DENSsolution six contact heating/biasing TEM sample holder on the electrodes. The patterning process was done using electron beam lithography with PMMA 4% photoresist. Before performing the metal deposition after lithography and development, the NWs with the protecting Al_2O_3 shell were dipped into buffered hydrofluoric acid - BOE 7:1 ($HF : NH_4F = 12.5 : 87.5\%$) for 10 s to completely remove the Al_2O_3 shell in the contact region and then put in diluted hydriodic acid (HI) for 5 s to remove the GeO_2 shell. The samples were then cleaned by Ar plasma for 15 s before performing 150 nm Al deposition by sputtering (with the purity of 99.995% and in vacuum at a pressure lower than 10^{-6} Torr). Finally, the samples were lifted off in acetone solution overnight. The heating experiments were done by two different approaches: i.e., i) using a direct Joule heating method as described in the paper by Mongillo et al [23]. Particularly, a voltage difference (V_{ap}) was applied through the two ends of the Al metal strip connected with two 2401 Keithley source meters providing the applied voltage and then slowly increased step by step of 0.025 V to increase the heating current ($I_h=V_{ap}/R_{strip}$). The resistance of the sputtered Al strips is around 130 Ω. The main advantage of this approach is performing the Al/Ge exchange reaction in a single step; however, the contact electrodes could easily damage at high applied voltage and current, before the exchange reaction actually started. ii) The samples were first heated using RTA in N_2 ambient at 300 ^oC during 20 s and cooled down to room temperature during 4 min. The RTA experiment was performed in a Jipelec™ JetFirst RTP Furnace [85]. RTA initiates the nucleation stage of the reaction in all contacts. Once Al has entered the Ge NW at the contact pad, the direct Joule heating can be performed without the need to apply high potentials/currents to the Al heating electrode, allowing propagation of the Al in the Ge NWs without damage to the Al contact. For temperature calibrated in-situ heating experiments, the samples were heated inside the TEM microscope using a commercial DENSsolutions [22] six contact double tilt TEM holder. High angle annular dark field (HAADF) scanning TEM (STEM) was performed on a probe corrected FEI Titan Themis

operating at 200 kV. The experiments were performed in STEM mode with a beam convergence angle of 20.7 mrad, electron beam current of 96 pA and beam diameter below 1.3 A.

5.3 The Nucleation of the Exchange Reaction and Degradation of the Al Heater by Joule Heating

Consecutive heating via rapid thermal annealing is a common technique for performing a metal/semiconductor NW thermal exchange reaction. Fabrication of an ultra-short Si segment between PtSi contacts has been reported in literature [27] from Pt thermal diffusion in a Si NW. However, the reproducibility of such a diffusion process is typically not precise at atomic length scales, due to the fact that the exchange reaction does not start in all NWs at exactly the same moment, or to different reaction speeds depending either on NW diameter or contact quality [39]. Direct Joule heating, first reported in the work of Mongillo [23], is an interesting technique to combine heating and biasing experiments in a single sample geometry, and allows heating while observing the diffusion process in the electron microscope using an in-situ biasing TEM sample holder. However, one drawback of this technique is that the heating electrodes can damage easily to initiate the reaction, which will be demonstrated in the following experiments.

During the NW selection process for making the Al contact electrodes on the Si_3N_4 membranes, sometimes we obtained two NWs lying side-by-side on the membrane, that we decided to contact. This allows us to investigate the diffusion behavior in both NWs with slightly different diameters under exactly identical conditions. Figure 5.2 presents the HAADF STEM images of Aluminum incorporation into two Ge NWs having 5 nm Al_2O_3 shell. The video of this experiment is available as supporting information SI M5.1. The contrast in HAADF STEM is related both to the sample thickness and the atomic number of the elements present. Since Ge is heavier than Al, the brighter contrast corresponds to the initial Ge NW, and the darker contrast to the entering Al metal, as the NW diameter, and therefore also the NW thickness, does not change much due to the exchange reaction. The diameters of the left and right NW are about 130 nm and 120 nm, respectively. The heating experiment was performed by passing a current from the left to the right of the Al metal strip (the electron flow is in the opposite direction) while monitoring the HAADF STEM image and contrast in the NWs. We slowly increased the applied voltage (V_{ap}) and observed the start of the exchange reaction at a defect, a small indentation at the surface in the middle of the left NW (indicated by a yellow arrow in Fig. 5.2a) when V_{ap}=1.7 V and I_h=3.5 mA. Then multiple nucleation points appeared at the NW surface. Clearly, even though the two NWs were contacted under

identical conditions, the exchange reaction in the two NWs was different as the reaction of the right NW was a bit slower than the left NW (Fig. 5.2b-f). Since the exchange reaction occurs underneath the Al contact pad, the metal coverage is an important factor that can affect the reaction behavior. As shown in figure 5.2e-f, we observe the formation of voids close to the right side of the small NW (the right NW), which is likely the cause of the slight difference in diffusion rate between the two NWs. The scenario of the exchange reaction could be: Ge atoms from the nanowire gradually dissolve into the Al reservoir by removing layer by layer of Ge(111) plane while Al atoms from the heating electrode diffuse into the NW to fill the empty space. This can be understood since the Ge(111) lattice spacing (0.32667 nm) is the largest interplanar distance of all crystal planes in Ge without intermediate planes (Fig. 5.2c). It can be noted in SI M5.1 that the reaction front (Al-Ge interface) stopped at the two edges of the Al contact pad and only started moving out when Ge atoms underneath the Al pad had fully dissolved in both NWs. This diffusion behavior results in a symmetric Al propagation length on both sides of the Al contact electrode.

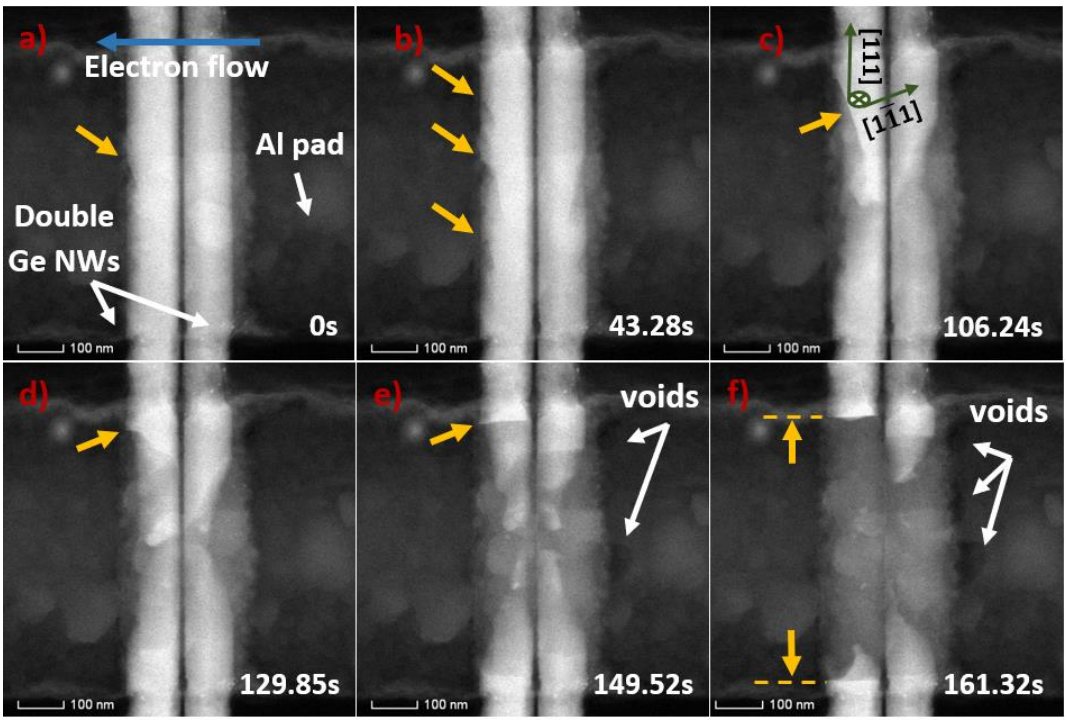

Figure 5.2: HAADF-STEM image sequences of thermally assisted diffusion of Al into double Ge nanowires based on Joule heating method. A heating current is passed through the Al heating electrode from the left to the right, as indicated by the blue arrow (the flow of the electrons is reversed). **a**) The propagation nucleated from a defect at the surface of a Ge NW (yellow arrow). **b**) Multiple reacting points appeared simultaneously when raising the applied voltage, accelerating the exchange process. **c-e**) The reaction front moved along the direction of (111) planes until

reaching the edges of the Al contact pad. **f**) The exchange reaction rate of the right NW is a bit slower than the left NW. The exchange reaction also induced voids on the right side of the Ge NWs. The scale bar is 100 nm. See the supporting information SI M5.1.

In another experiment, presented in SI M5.2, we observed the formation of Al crystals on the heating strip, and some remaining Ge islands present below the contact electrode. Figure 5.3 shows the HAADF images of Al incorporation in a 162 nm diameter Ge NW with a 5 nm Al_2O_3 shell. The exchange reaction started at V_{ap} = 0.725 V and I_h = 3.2 mA.

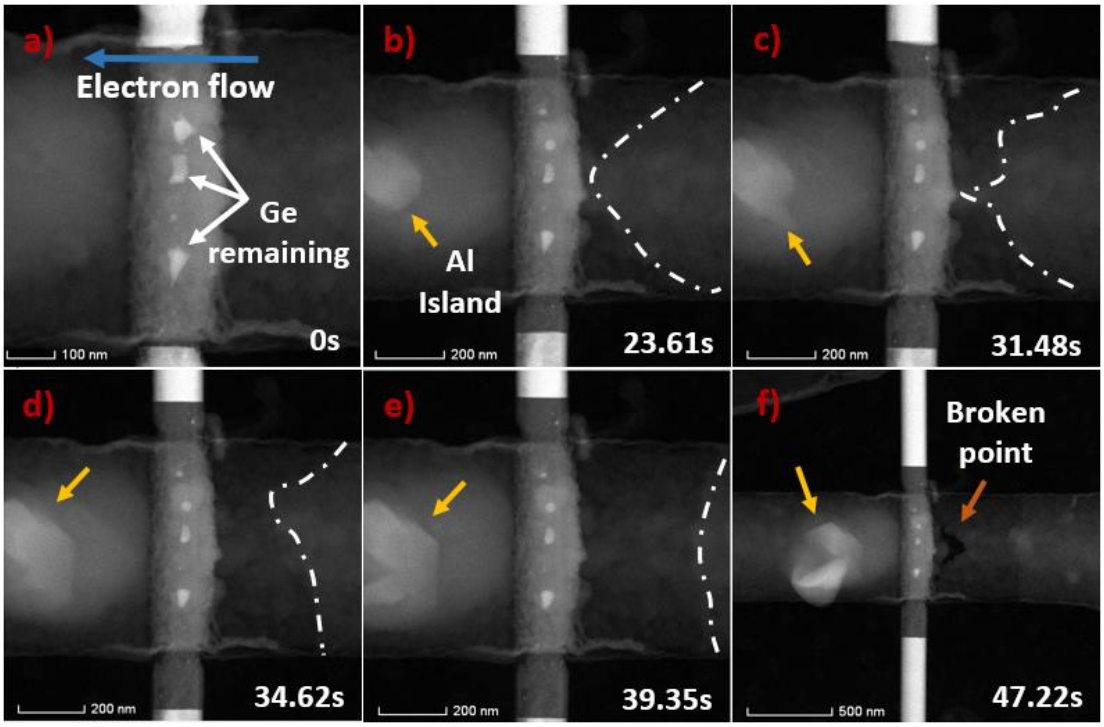

Figure 5.3: HAADF-STEM images of Al intruding in 130 nm Ge NW with 5 nm Al_2O_3 shell by Joule heating method. **a**) Some remaining Ge islands are present underneath the Al contact pad when the reacting front moved out. **b-e**) The diffusion of Al atoms into the Ge NW and the formation of a large Al crystal (yellow arrows) lead to a local exhaustion of Al atoms on the contact pad. **f**) A cracking point appeared on the right side of the NW in the Al contact, creating an open contact and blocking the heating current. The orange arrow indicates a broken point in the Al electrode. The scale bar varies in each image. See the supporting information SI M5.2.

As can be seen in figure 5.3a, even after the reaction front had moved out from underneath the Al metal contact pad, some Ge islands (indicated by white arrows) remain present in the NW underneath the contact pad. Besides, when the heating temperature was increased, a large Al crystal formed on the Al contact (Fig. 5.3b-f). The formation of Al crystals on the heating pads was

typically observed in most of the heating electrodes. The redistribution of Al atoms by the replacement with Ge atoms within the NW and the 'uphill' diffusion into the large Al crystal caused a local exhaustion of Al atoms from the contact pad. Consequently, a cracking point appeared on the right side close to the NW surface (Fig. 5.3f). We have also performed ex-situ heating experiments on similar devices using rapid thermal annealing, and no damage was found at the Al contact. Hence, the degradation of the Al heating electrode in Joule heating process is likely due to the electro-migration effect of the heating current. The result is in good agreement with reports [96] where the current will result in the formation of voids on the negative electrode and Al islands tend to form on the positive side.

From these experiments we saw that the initiation of the exchange reaction can occur at multiple nucleation points below the Al contact, and that the reaction interface moves out from this contact only once all the Ge underneath the contact has been consumed. Using the Al metal strip as a direct Joule heater to initiate the solid-state exchange reaction can also damage the Al contact, most likely due to electro-migration phenomena and the relatively high current that is needed to start the exchange reaction. In the section 5.7, we will show that this can be mitigated using first an ex-situ RTA of the specimen to initiate the exchange reaction and then continue the Al propagation process in a direct Joule heating experiment. This approach helps to preserve the contact quality and reduces the heating current during the in-situ annealing process. Using a combination of both ex-situ and in-situ annealing we could perform experiments in a more reliable way and were able to study the reaction interface in high detail.

During the in-situ heating experiments, we have seen an influence of the electron beam on the exchange reaction. Moreover, we monitored the reaction kinetics and observed an influence of the NW surface quality on the reaction kinetics and the height of the nucleation step at the reaction interface. Hence for an atomically precise control of the diffusion process, especially for producing sub- 10 nm semiconductor segments, it is important to master these effects during the sample preparation and TEM observation.

5.4 Effect of Electron Beam on the Reaction Interface Propagation Rate

It is well known in TEM investigations that the electron beam can damage the specimen if it stays on the specimen for a certain time. This can be due to the high energy of the electron beam that causes a displacement of atoms from the lattice above the displacement threshold of the investigated materials and therefore artificially perturbs the vacancy concentration from equilibrium [113]. Since we are performing heating experiments, another potential explanation can be additional heating due to the electron beam. In supporting information SI M5.3 we present an experiment where the edge of the reaction interface was imaged in high resolution HAADF STEM. The Ge NW was oriented on the [110] zone axis and (111) planes are visible. Since the NW core part is much thicker than the edge, the lattice spacing is less visible at the NW core. After recording the video shown in SI M5.3, we increased the magnification even more and zoomed in at the reaction interface at the center of the NW. After that, the magnification was reduced to have the entire reaction interface within the field of view. Presented in supporting information SI M5.4 we observed a clear influence of the electron beam on the diffusion behavior at the Al/Ge interface, in the case that the electron beam scanned only a small region of the reaction interface (as done in SI SI M5.3) and then zoomed out to lower magnification for observation. During STEM HAADF serial imaging, the electron beam was scanned over a 512 x 512 raster from the left to the right and from the top to the bottom in a square field of view of (17 nm x 17 nm) at high magnification and (193.28 nm x 193.28 nm) at lower magnification (shown in SI M5.4) with a per-pixel dwell time of 2 μs. The electron dose rate (e. nm^{-2}. s^{-1}) was calculated by dividing the probe current (96 pA) by the area of the raster, which is about 2.08 x 10^6 and 1.61 x 10^4 $e.nm^{-2}.s^{-1}$ at high and low magnification, respectively. Figure 5.4 shows the influence of the electron beam on the Al/Ge binary exchange reaction in the 133 nm Ge NW when it was interacting with the specimen. As indicated by the orange arrow in figure 5.4a, the Al migration front had advanced faster at the location where the beam had scanned a small area in previous frames. When the beam then scans a larger area including the entire reaction interface (Fig. 5.4a-f), the difference between the middle front and the two edges becomes smaller, and finally the interface becomes straight again. Similar observations have been reported in the work of Fauske et al [114] where the thermal diffusion of Au in GaAs nanowires was studied. Similar to their observations, the beam induced increased replacement rate was limited to the regions near the electron beam exposed area, and did not extend across the entire nanowire cross-section. Therefore, once a step has nucleated, it does not

necessarily advance over the entire reaction interface, indicating that the nucleation event is not the rate limiting step of this reaction.

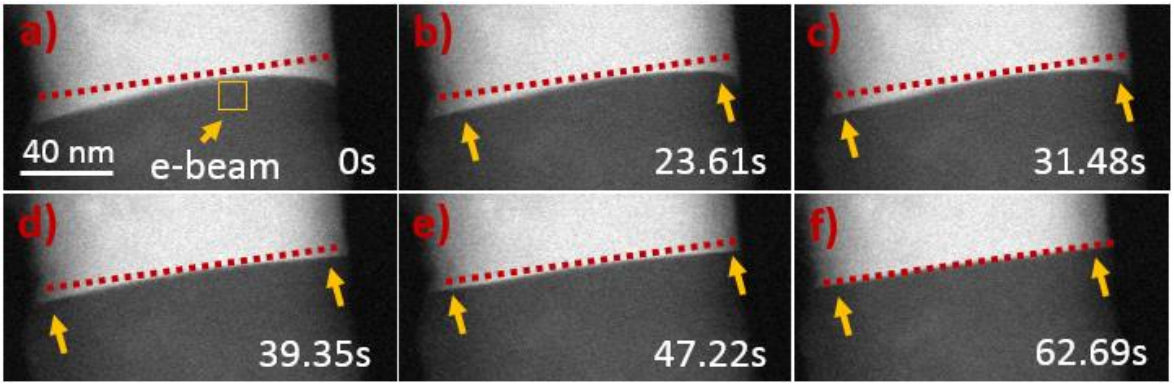

Figure 5.4: Sequence of HAADF-STEM images after high resolution imaging at the region indicated in (a). a) Image obtained after zooming out from the indicated region. b-f) After decreasing the magnification, the reaction interface is progressively restored to a flat interface. The yellow arrows indicate the regions far from the more irradiated square indicated in (a). See supporting information SI M5.4.

5.5 Influence of NW Diameter on Propagation Rate

As mentioned in section 5.1, Sebastian Kral has shown a plot of the Al propagating length versus the nanowire diameter characterized by a large amount of scatter [44]. Indeed, with ex-situ heating techniques, it is very difficult to elucidate the influence of the NW diameter on the diffusion speed since we have no information about the starting time of the exchange reaction. From our real time observations, it appears that the reaction interface advances faster in smaller diameter NWs compared to the large diameter NWs. However, the evidences are not straight forward since it can also be the effect of the metal surface coverage, which is different between small and large diameter NWs. Figure 5.5a-b shows the HAADF STEM images of two NWs propagating side by side. Their respective diameters are 150 and 127 nm. The experiment was carried out using varying heating current, therefore we cannot interpret the kinetics of the reaction looking at the propagation length L as a function of time, however we can compare the propagated lengths in the two different NWs and compare the propagation into the upper part of the NWs, that we call “top part” and into the “bottom part”.

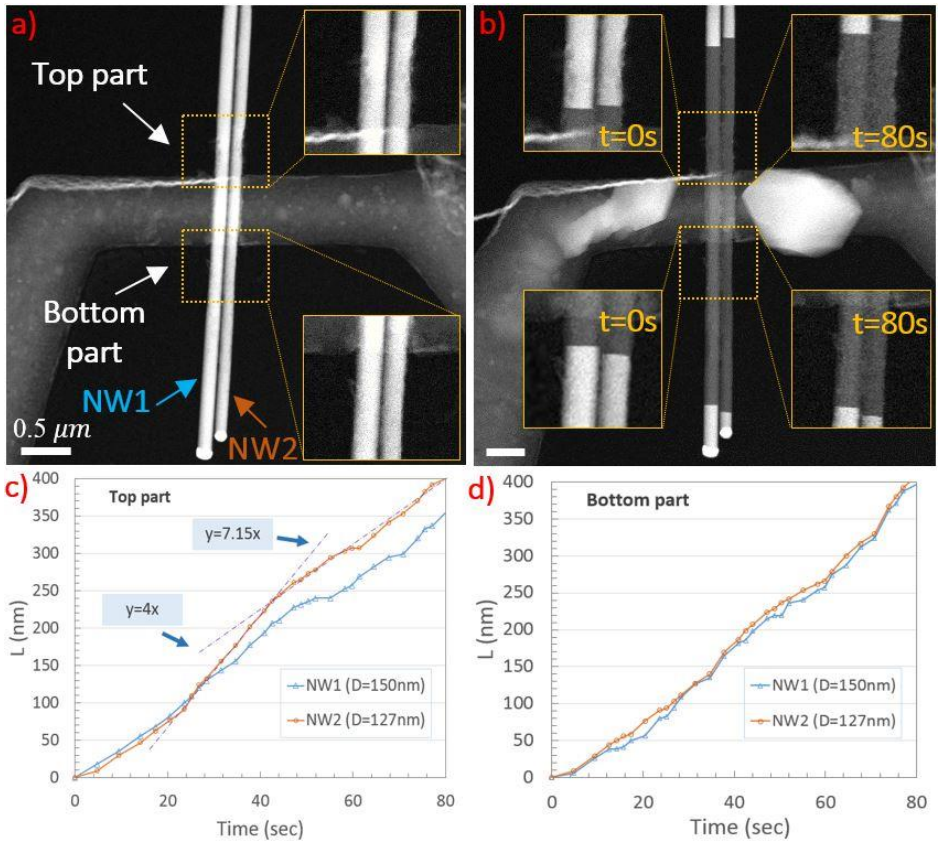

Figure 5.5: HAADF STEM images of fabricated device for direct joule heating. (**a**) The sample before reaction initiation. Insets show higher magnifications of NW parts just above and below the heater electrode. (**b**) The sample after the exchange reaction. Insets show the same regions at different moments. (**c**) The length of the transformed segment versus time L in the top part of both NWs. The interface was followed starting from an arbitrarily defined moment during the reaction referred to as t = 0 when the reaction interface had entered both NWs. (**d**) L versus time for the bottom part of the NWs. See supporting information SI M5.5.

Figure 5.5c-d shows plots of the of the interface location in both NWs as a function of time. The insets show that in the top part of the NWs located just above the heater electrode the NW surface is locally rough (presence of contrast variations on the NW) and the thinner NW2 also has a region where the diameter is locally reduced, while the NW surfaces have no such roughness in the NW regions below the heater electrode (smooth contrast on the NWs). Figure 5.5b shows the sample at the end of the Joule heating experiment, and the insets show the reaction interface both in the top part and bottom part of the NWs at two moments during the experiment where t = 0 indicates the moment where we start to follow the reaction interface that is followed during 80 s. We see that the reaction interface has first entered in the thinner diameter NW2. Figure 5.5c-d shows the length the reaction interface has traveled during 80 s in both NWs in the top part and bottom part of the

NWs, respectively. We observe that in the top part of the NWs the reaction speed is first similar in both NWs during around 20 s, but then the reaction speeds up at the thinner location in NW2 (Fig. 5.5c). The reaction interface speed recovers to approximately the original value in NW2 when the reaction interface has passed the thinner region. In the bottom part of the NWs, we find very similar reaction speeds in both NWs (Fig. 5.5d). In this experiment, we see that the reaction interface advances first out from the contact into the thinner NW but then very similar reaction speeds are observed in both NWs. Yet, at the thinner location in NW2 above the heater electrode, the reaction advances faster. We can conclude that indeed the influence of the NW diameter on the reaction speed is ambiguous and that we truly need in situ measurements to better understand the delicate interplay between NW size and other potential factors such as surface roughness (potentially related with surface defects) and strain.

5.6 Radial and Axial Propagation of the Al/Ge Interface – Effect of Al_2O_3 Shell

The diffusion rate could also be affected by other factors; for instance, in the study of Holmberg et al [115], they have reported the growth rate dependence on the distance from the metal source. Yaish et al [39], have showed in the Ni/Si system that the quality of the nanowire surface determined by the exposure time to ambient air before the metal deposition step could change the growth rate from the square root to the linear time dependence. In this work, we present clear evidence of an effect of the NW surface quality on the reaction kinetics and demonstrate that the surface quality can be improved by the presence of a protecting shell. Figure 5.6a-f represent HAADF-STEM images of Al migration in a 133 nm Ge NW without the presence of an Al_2O_3 shell. These NWs were exposed to the atmosphere so that they have been oxidized forming a GeO_2 shell (a 3D reconstruction of the GeO_2 shell has been reported in the paper [13]). Before starting the heating experiment, the NW was oriented such that the NW Ge(111) growth plane is parallel to the electron beam to allow better observation of the nucleation phenomena at the Ge(111) reaction interface. Since we observed an influence of the electron beam on the diffusion behaviour at high magnification, which additionally limits the field of view for the observation allowing to see only part of the reaction interface, we decided to lower the magnification for an overview of the exchange reaction of the Al/Ge interface, working at a resolution of 377.5 pm/pixel, just below atomic resolution. HR-STEM images were taken after the propagation had stopped. The Joule heating was started and series of HAADF images were acquired during the exchange reaction. The

diffusion behavior in this NW is presented in the supporting information SI M5.6. As shown in figure 5.6a, the interface of Al-Ge was initially very sharp. After 1.574 s, there was a jump of the Al reaction interface of 6.5 nm in the axial direction at the left side of the NW, corresponding to a replacement of 20 layers of Ge(111) atomic planes. Then the Al/Ge reaction front runs in the lateral direction from the left to right (along the NW diameter of 133 nm) and finishes a cycle after 7.87 s. These observations allow calculating the diffusion speed in the lateral direction to be about 16.9 nm/s. Figure 5.6g shows the plot of Al protruding length ***L*** as a function of time in the axial direction of the propagated NW without having the Al_2O_3 shell. The graph demonstrates local variations in propagation speed of the Al/Ge reaction front, due to the nucleation and subsequent ledge flow of steps of a few nm in height on the reaction interface. As can be seen from the plot, the average propagation rate of the reaction interface is about 0.64 nm/s. It is worth noting that the observed growth rate in the axial direction is 26 times smaller than in the lateral direction. This result is quite reasonable since it takes some time to nucleate a new step on the reaction interface.

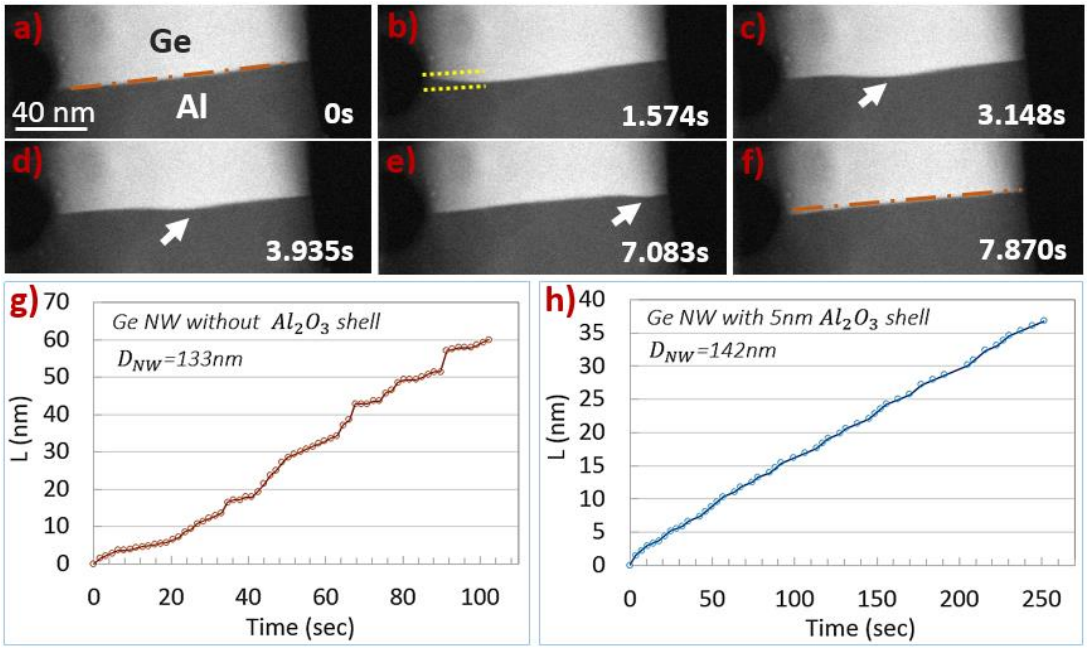

Figure 5.6: a-f) Series of HAADF-STEM images of Al migration in a Ge NW showing the nucleation of a step at the Al/Ge reaction interface and its propagation in the lateral direction from the left to the right. The diameter of the NW is about 133 nm. The yellow dash lines present the step height. The white arrows indicate the positions of the step moving along the reaction interface from the left to the right. Figure 5.6g-h shows the plot of Al converted length *L* as a function of time in the axial direction of the NW without and with the protection of a 5 nm Al_2O_3 shell,

respectively. The movie of the diffusion presenting the experiment of figure 5.6a-g is available for viewing in supporting information SI M5.6. The experiment presented in figure 5.6h is available in the SI M5.8.

From literature [116], it has been known that the Ge surface is very sensitive to atmospheric ambience. Probably, the NW surface was strongly oxidized, and this may be related to increased surface roughness and/or the formation of surface defects at the Ge/GeO_2 interface (the HAADF STEM and BF STEM images of the Al/Ge interface and a zoom on the oxidation shell are shown in figure 5.7a-b). The trapping and de-trapping of the reaction interface at these defects could result in the observed stepwise growth. In contrast, investigating the Al/Ge exchange reaction in a Ge NW with the presence of a 5 nm Al_2O_3 shell, a smoother linear time dependence of the Al diffusion length is observed and plotted in figure 5.6h. The reaction interface speed in this experiment is about 0.143 nm/s. It is worth noting that the diffusion speed in this case is lower than in the example of a NW without the protecting shell (0.64 nm/s). However, we cannot interpret the kinetics between the two NWs since the Joule heating experiments are not temperature calibrated. These results may indicate that in the latter case the quality of the NW surface was better controlled by the protection of the Al_2O_3 layer, hence the exchange reaction took place uniformly along the NW axial direction without the strong fluctuation of the diffusion rate due to surface defects. A smooth advancement of the interface is paramount for controlling the length of the semiconductor region with atomic scale precision.

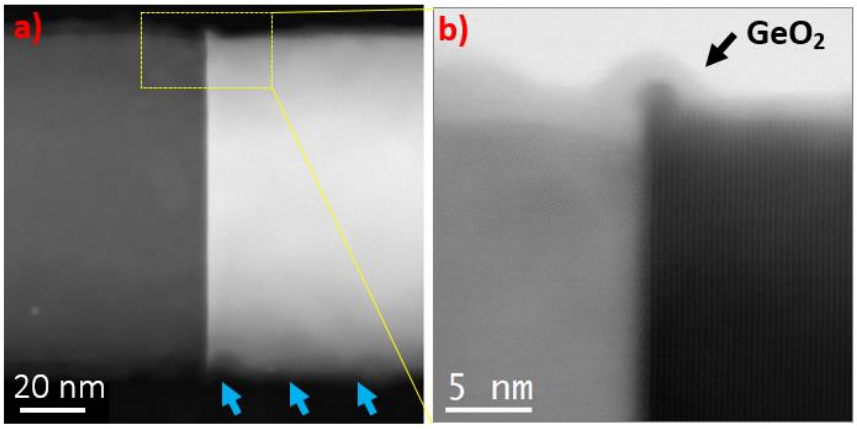

Figure 5.7: (**a**) HAADF STEM of the Al/Ge interface showing the non-uniform surface of the Ge NW and (**b**) BF-STEM image of the zoom on the top surface of the Al/Ge interface, showing the presence of a thin GeO_2 shell on the NW.

It should be noted that the current study focuses on relatively large diameter NWs (120≤d≤162). Previously we have observed a smooth propagation behavior in much thinner NWs (15≤d≤50) at low temperatures (250 – 330 ºC) where the length of the propagated region as a function of time follows a square root behavior, indicating the reaction is limited by diffusion [13]. In addition, using an ex-situ reaction at a heating temperature of 350 ºC, it was observed that no propagation occurs in NW diameters above 150 nm [44]. These combined observations potentially indicate that the reaction rate is limited by diffusion for small NW diameters, and is limited by an interface (either the metal reservoir-NW interface or the reaction interface) for larger diameter NWs.

5.7 Al/Ge Thermal Exchange by Rapid Thermal Annealing (RTA)

Using the direct Joule heating technique, it is quite difficult to generate the thermal exchange reaction gently without damaging the heating electrode. Moreover, achieving long Al exchanged lengths ($\geq 1.5\ \mu m$) is hardly obtained in direct Joule heating since a higher applied voltage is required for extending the Al/Ge interface far from the Al heating electrode, subsequently causing the formation of Al crystals on the heating electrodes and loss of the electrical connection. The experimental results are therefore not reproducible for a similar heating process. To assist the thermal reaction for a lower applied voltage, we proposed an ex-situ annealing step (RTA) to start the exchange reaction underneath the Al/Ge contact pad. Since the whole sample is heated at the same temperature, it is expected that the heating electrodes are preserved without any damage to the electrical conduction. When the reaction front spreads out from underneath the contact pad, consecutive heating is performed to obtain a small Ge segment (≥ 100 nm). The direct Joule heating method can be finally applied to finalize the thermal diffusion in a controlled manner.

Figure 5.8 shows the HAADF STEM images of a passivated 155 nm Ge NW (with 5 nm Al_2O_3 shell) before (a) and after the consecutive thermal treatment (b) with a zoom on the unreacted Ge segment. In this experiment, the annealing process was performed at 300 ºC for 35 s (in N_2 gas) and then cooled down to room temperature in 4 min, giving 650 nm of Al propagation length from each side of the Al contacts. The unreacted Ge segment was then made even shorter by another 10 s annealing step similar to the previous recipe, to achieve another 200 nm of Al intrusion length. The final structure had a 165 nm unreacted Ge segment ready for the direct Joule heating with all heating electrodes nicely conserved. EDX mapping at the unreacted Ge segment is presented in

figure 5.8c-d. The line-scan crossing the Al/Ge interfaces shows the formation of sharp interfaces of about 5 nm width.

In general, conducting the metal/semiconductor thermal exchange by ex-situ heating (RTA) brings many advantages such as fast annealing time and specimen preservation (e.g. heating electrodes). However, due to the lack of sample evolution information during the annealing process, it is an unreliable process for the production of ultra-short semiconducting channel lengths (sub- 100 nm).

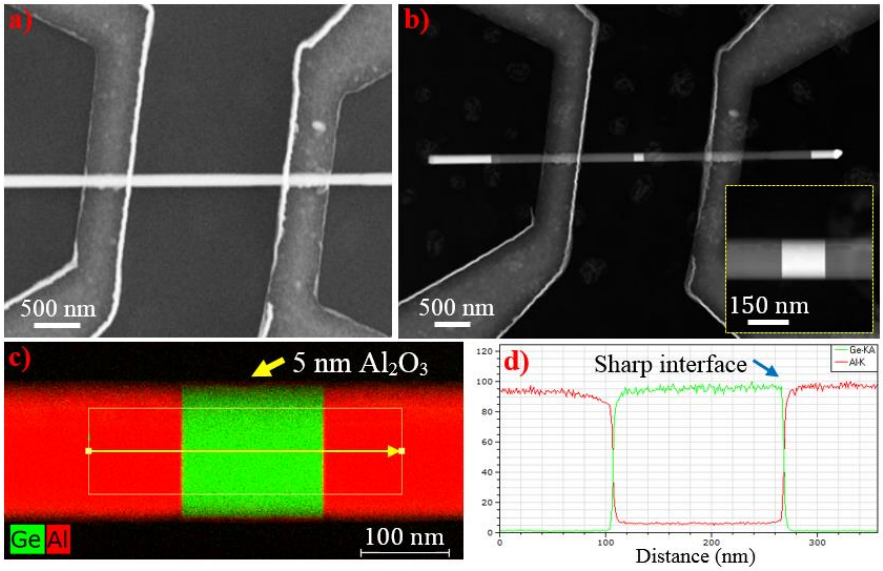

Figure 5.8: HAADF STEM images of contacted 155 nm Ge NW (with 5 nm Al_2O_3 shell) before (**a**) and after consecutive RTA (**b**). (**c-d**) EDX mapping and line-scan profile taken at the 165 nm unreacted Ge segment showing the presence of the sharp Al/Ge interfaces.

Table 5.1 presents the statistical data of Al propagating length at different annealing time intervals. The ex-situ heating was performed at 300 ^{o}C in N_2 ambience and cooled down to room temperature in 4 min.

Table 5.1: Al intrusion length versus the annealing time.

Heating temperature (^{o}C)	Annealing time (s)	Al diffusion length (nm)
300	15	400 - 600
300	20	500 - 700
300	30	600 - 900
300	40	800 - 1200

5.8 The influence of Al Sputtering/E-beam Evaporation on the Solid-State Reaction

As a side note, in this PhD work, specimens were also fabricated by different metal deposition techniques using either sputtering or electron beam evaporation techniques. From several in-situ experiments, it was noted that Al/Ge solid state reaction occurred easier in the specimens that were prepared by Al sputtering. The exchange reaction was observed to initiate at low applied voltage (e.g., 0.725 V as presented in section 5.3) while the specimens prepared by electron beam evaporation could not start even at very high applied voltage. Figure 5.9a-b shows the BF STEM image of the contacted $Si_{0.05}Ge_{0.95}$ NW prepared by electron beam evaporation. The resistance of the contact electrode is 400 Ω, which is higher than the one deposited by sputtering technique (~130 Ω). To reduce the risk of losing the heating electrodes during the heating process, a pre-step of ex-situ heating via RTA was therefore performed on this device to assist the thermal exchange reaction. The specimen was annealed at 300 ^{o}C for 20 s, giving 250 nm of Al propagating length. When performing direct Joule heating on the device, the exchange reaction was observed starting at 2.250 V (with the heating current I_h= 8.13 mA). The real time observation of the Al/Ge thermal diffusion is available for viewing in supporting information SI M5.7. As can be seen from the movie, the heating electrode was rapidly damaged after a short Al propagating length of 250 nm. Besides, the evolution of the heating electrode during the propagation results in a vibration of the specimen (shown in the movie).

It is believed that Al sputtered atoms carry high energy to bombard the Ge contacted surface during the metal deposition process. Therefore, they can penetrate through the oxide/surface barrier of the Al/Ge contact interface helping to reduce the thermal energy that is required for the exchange reaction. In case of specimen prepared by the electron beam evaporation technique, the rapid melting of the heating electrode can be related to the bad electrical conductivity. From STEM images shown in figure 5.9a-b, we can recognize that Al pads deposited by the electron beam evaporation technique have large grains while the structure of electrodes deposited by the sputtering technique seem to be more compact (Fig. 5.9c-d). The presence of grains on the heating electrode can have a negative impact on the electrical conductivity since charge carriers can be scattered more at the grain boundaries causing the increase of the resistance. Under a high applied heating current, the electrode can melt due to the large amount of generated heat before the exchange reaction actually starts.

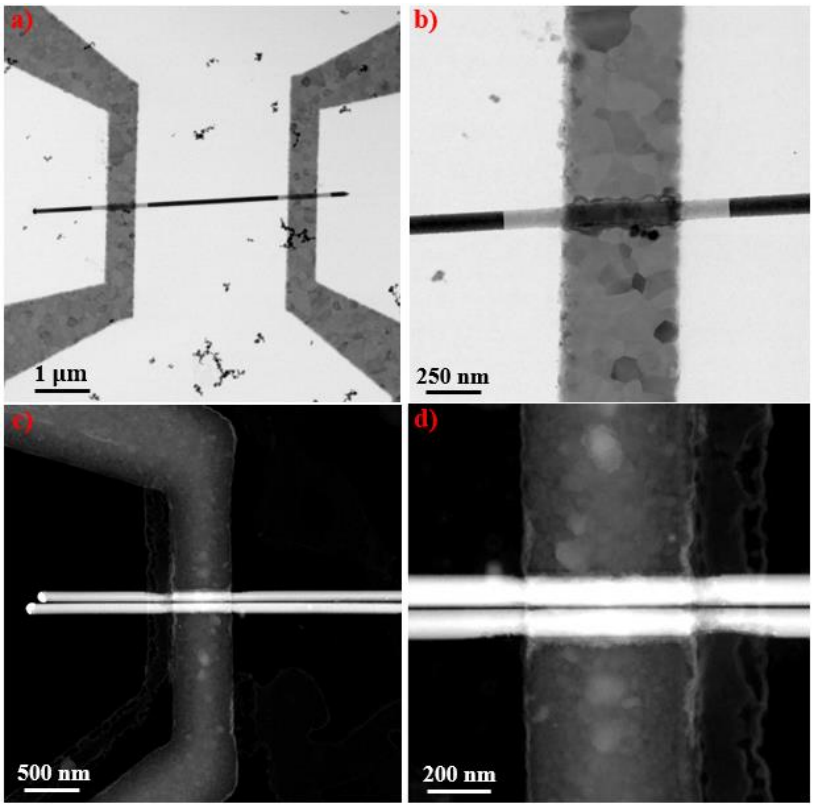

Figure 5.9: (**a**) BF-STEM image of a fabricated device with 200 nm Al contact electrodes depositing by the electron beam evaporation technique and (**b**) a zoom on the Al/Ge contact region. (**c-d**) HAADF STEM images of the Al heating electrodes prepared by sputtering technique.

In general, the sputtering technique is therefore preferable over the electron beam evaporation technique when performing direct Joule heating since it doesn't require a pre-step of RTA to start the exchange reaction. However, to preserve all the heating electrodes for post-investigation, it is recommended to start the thermal diffusion by RTA, potentially followed by the direct Joule heating technique.

5.9 Combining Ex-Situ and In-Situ Heating to Produce an Ultra-Small Ge QD

Using the direct Joule heating technique, it is quite difficult to generate the diffusion gently without damaging the heating electrodes. Therefore, we first annealed the sample by RTA to initiate the exchange reaction between Ge and Al. Since the whole sample was heated at the same temperature, no damage was found at the contact pads after the intrusion of Al into the Ge NW. Figure 5.10 represents the HAADF-STEM images of Al incorporation in a 142 nm diameter Ge NW with 5 nm Al_2O_3 shell, to obtain a smooth advancement of the reaction interface. The sample

was heated at 300 ^{o}C for 20 s in N_2 ambience, giving 750 nm propagation length from each side (Fig. 5.10a). We then performed the direct Joule heating sequentially from each side in-situ in the TEM using HAADF STEM imaging to carefully reduce the unreacted Ge segment length. The movie for the production of a small Ge segment is presented in SI M5.8. When the Ge segment reached sub- 10 nm scale, it is important to lower the applied heating voltage to decrease the diffusion rate until achieving the desired segment length. Since we observe the position of the reaction interface in real time in-situ, we can stop the heating current at any moment. As we use an extremely local heating, the injected power is very small and dissipated almost instantly through the contacts when we remove the heating current. It is this capacity to heat and cool almost instantly that finally allows us to deterministically fabricate a (nm) sized Ge segment. Figure 5.10b illustrates the formation of an ultra- small 7 nm Ge segment after a RTA treatment followed by an in-situ Joule heating process. The segment length of this Ge disk was intentionally stopped at 7 nm for further investigations. Due to the relatively large NW diameter, that is much larger than the thickness of this Ge disk, we expect mostly axial confinement in this structure and therefore this structure would resemble a quantum disk. Ge quantum dots could also be reliably fabricated with this method using NWs with smaller diameter. It is also possible to perform a complete Al-Ge exchange for the fabrication of a monocrystalline Al NW [111]. Figure 5.10c shows an HR-HAADF-STEM image of the interface between the reacted and unreacted part with the corresponding Fourier transform (FT) in the inserted figure. The interface appears quite sharp when oriented on the [10$\bar{1}$] zone axis of Al. There is a rotation of 18 degrees between the Al(111) atomic planes and Ge(111) planes of the NW growth direction as can be observed in the FT shown in the inset of figure 5.10c.

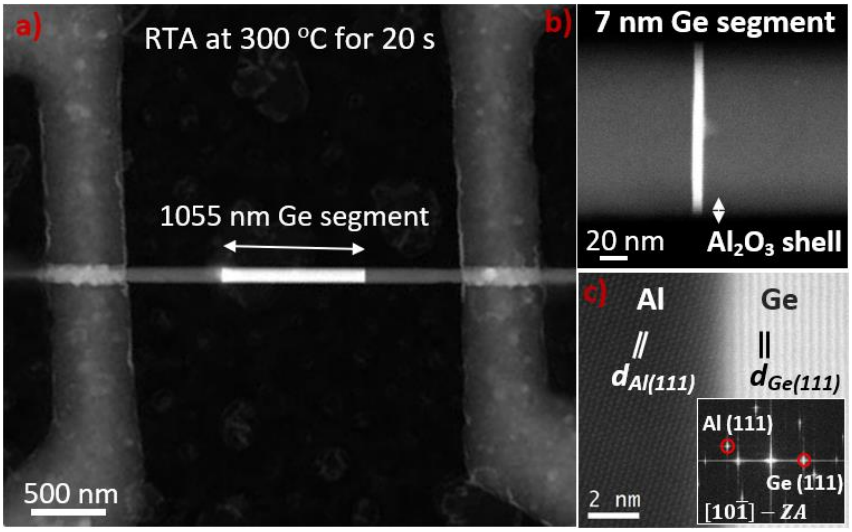

Figure 5.10: a) HAADF-STEM image of an axial Al/Ge/Al NW hetero-structure formed after the RTA treatment at 300 °C for 20 s. The NW diameter is about 142 nm and covered by 5 nm Al_2O_3 shell. **b**) An ultra- short 7 nm Ge segment was created by combining RTA and in-situ Joule heating method. **c**) HR-STEM image with the corresponding FT at the Al/Ge interface showing the 18 degree rotation between Al (111) and Ge (111) planes when the specimen is oriented on the [10$\bar{1}$] direction of observation on the Al part. The interface appears very sharp. See supporting information SI M5.8.

Due to the large difference in lattice constants between Al (aAl= 4.05 Å) and Ge (aGe = 5.65 Å), a rotation at the interface is generally observed, presumably to accommodate the lattice mismatch. We show a schematic of this interface (shown in Fig. 5.11). The 18° rotation may be a way for strain minimization and lattice relaxation.

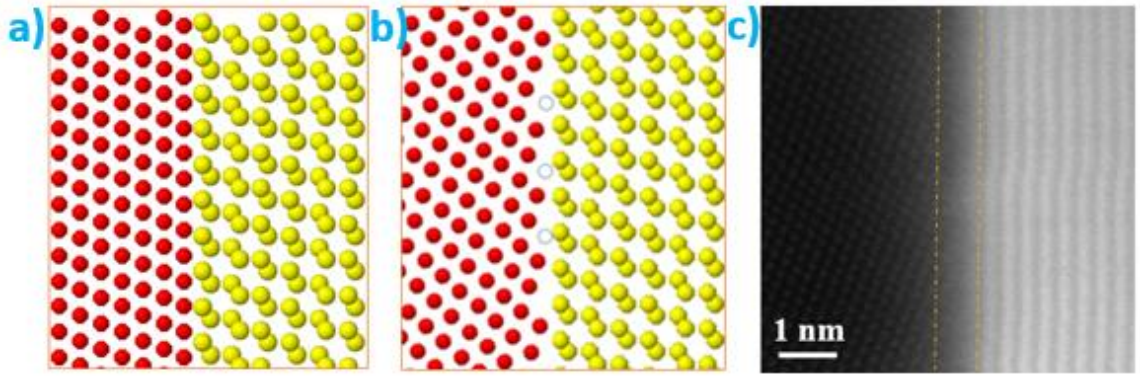

Figure 5.11: **a-b**) Schematic illustrations of lattice matching between Al(111) and Ge(111) planes without and with 18 degrees of rotation between the two planes. The schematics reflect the perfect crystal lattice. **c**) The HR HAADF STEM image of the real Al/Ge interface showing the blur in the HAADF contrast at the interface.

5.10 Electrical Measurements on Short Ge NW Segments

In this study, we performed electrical experiments on low dimensional Al/Ge/Al devices, with the aim to characterize the maximum current density that a short Ge segment can withstand before being melted by the high passing current. Besides, the IV characteristics of several contacted Ge segment lengths were measured before and after the thermal exchange reaction to determine the contact resistance of the Al/Ge interface.

5.10.1 Maximum Electrical Conduction of Short Ge Segments

For the experiment, un-doped Ge NWs with a 20 nm Al_2O_3 passivation shell were used. The NW diameter varies in the range of 40-45 nm with about 3 µm length. The NWs were contacted on both ends by Al metal electrodes on the flat Si_3N_4 membranes and were annealed where the duration of the annealing was varied with the aim of achieving a short segment length, in the range of 200-550 nm. The electrical measurements were performed manually using the Keithly 2401 sourcemeters, where a current was applied through the Ge segment and increased slowly by 0.5 µA steps each 30 s, meanwhile the current-voltage (IV) characteristic was recorded. The experiment was performed while the specimen was inserted in the TEM microscopes (FEI Titan Themis at 200 kV or CM Philips CM300 at 300 kV) for a real time observation of the structure evolution at high current densities in the Al/Ge/Al NW heterostructures. The plots of the measured voltage and resistivity versus the applied current for a 255 nm Ge segment length were shown in figure 5.12a-b, respectively.

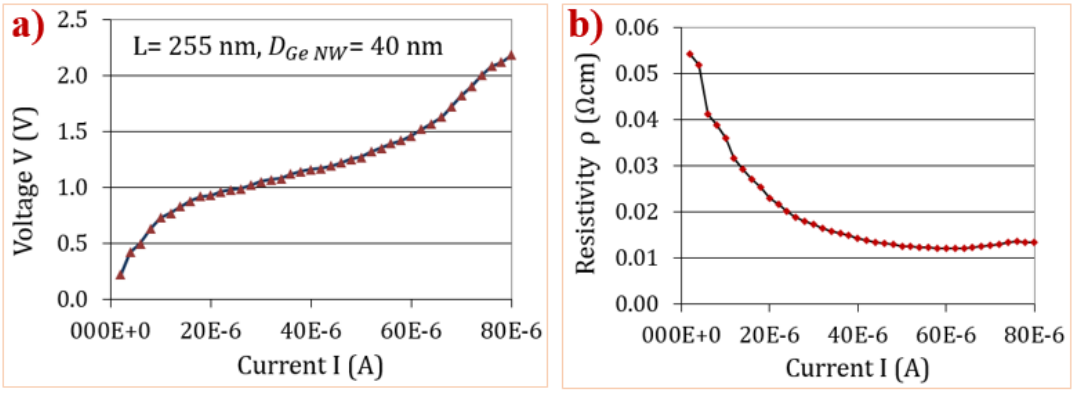

Figure 5.12: (**a**) IV characteristics and (**b**) Resistivity dependence on applied current measured on the 255 nm Ge segment length.

As shown in figure 5.12a, the IV characteristics indicate a Schottky contact behavior of the created Al/Ge interfaces. The calculated resistivity shows a hyperbolic trend with increasing current. Then, we kept the current at a constant value of 80 μA to check the ability to sustain the high current over time. Remarkably, after 1 hour, the segment still survived. However, we observed a drop of the measured voltage, from 2.06 V to 1.36 V. Probably, the crystal structure had been refined for a better electrical conduction. After that, the current was again slowly increased as described previously. The current was increased to 100 μA, where the Ge segment suddenly failed, creating several holes along the NW. These current levels correspond to current densities as high as 6.4 x 10^6 A cm^{-2} that can be supported over hours, and a failure current density of 8 x 10^6 A cm^{-2}. Figure 5.13 shows the HAADF STEM images of created Ge segments with different lengths before and after passing a high current and failure.

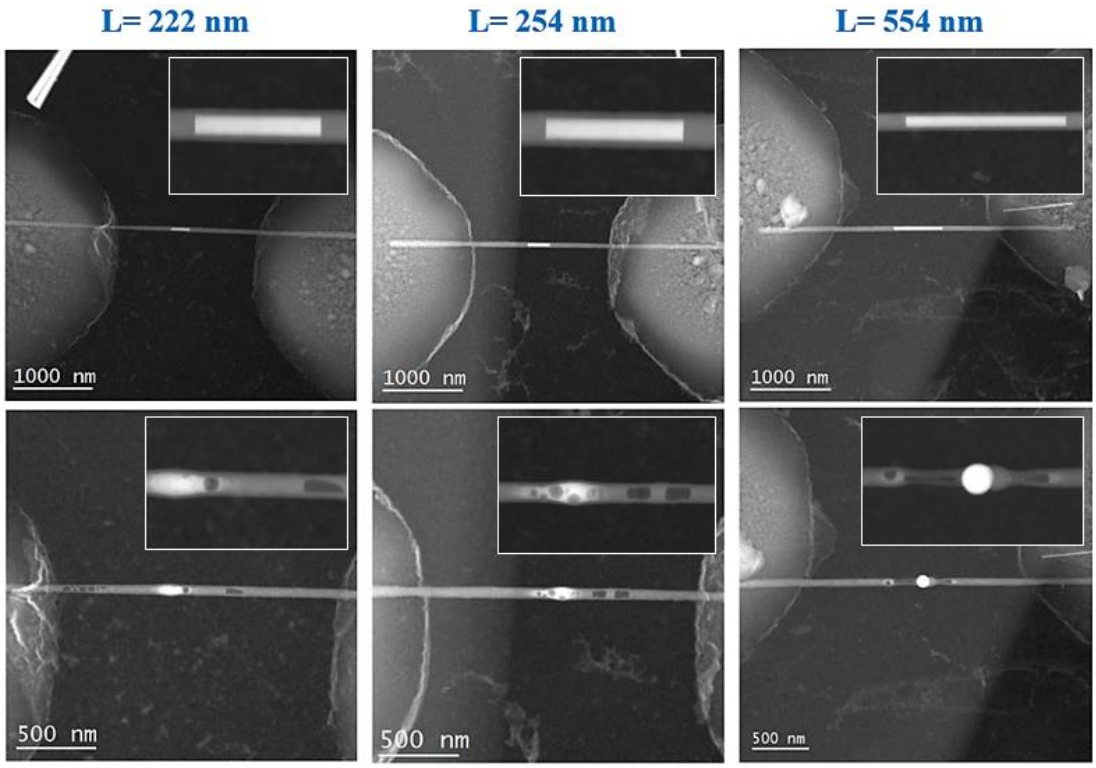

Figure 5.13: HAADF STEM images of created Ge segments before and after passing the high current and failure.

Specifically, as shown in the longest Ge segment (L = 554 nm), the melting of the Ge segment formed a Ge bubble on the NW. Probably, the generated heat in this long segment was higher than in the first two shorter segments due to the larger resistance. EDX mappings on the melted part of the Ge segment (L= 254 nm) is shown in the figure 5.14.

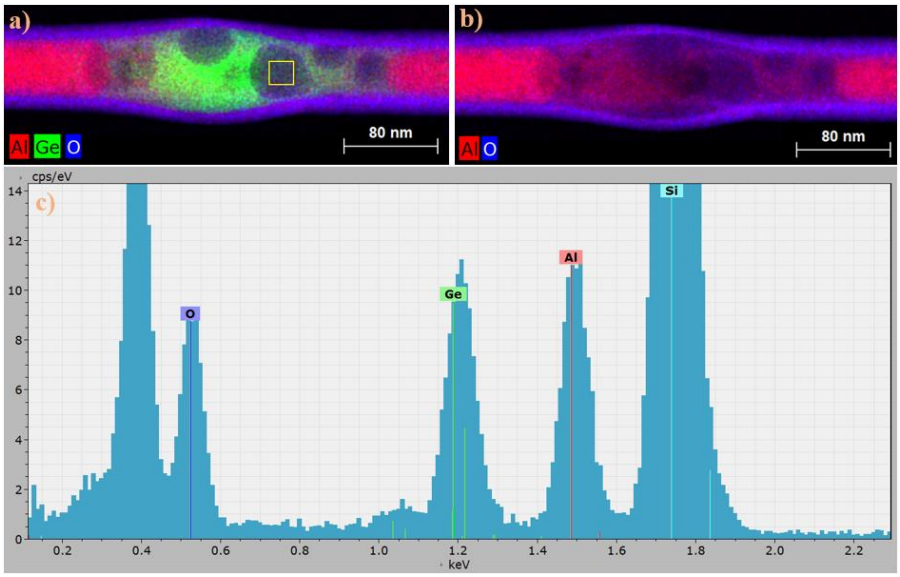

Figure 5.14: EDX chemical maps of the present elements in the failed Ge segment (L= 254 nm). The Al, Ge and O maps are presented in red, green and blue color, respectively. A spectrum analysis taken on the yellow box in figure 4.13a shows the presence of Ge, O and Al on the black hole.

As shown in figure 5.14c, the spectrum taken at the yellow box indicates the presence of Ge, Al and O with small quantities. It seems that these are empty holes surrounded by Ge atoms. In addition, Al atoms migrated on the semiconducting part as shown in the Al map (Fig. 5.14b). The IV measurement on this failed segment showed no electrical conduction after the failure.

5.10.2 Measurements of Contact Resistance in Doped Ge NWs

The goal of the experiment is to elucidate the Al/Ge contact quality before and after Al metal thermal incorporation into the Ge NW. To increase the conductivity of the Ge NWs, n-doped Ge NWs were used, which have 50 nm in diameter and 4 μm in length. In addition, passivated Ge NWs having 5 nm of Al_2O_3 shell were also used, which aims to elucidate the influence of the HF etching process on the electrical contact quality of the created Al/Ge contacts. The resistance of contacted NWs were measured using the BENNING MMP3 multimeter [117], which has a precision range of 0.1 Ω - 40 MΩ. Since the Al/Ge contact is not Ohmic, we only extracted the resistance value at a specific voltage applied by the multimeter (0.4V), with the aim to allow comparison between different samples.

5.10.2.1 Al/Ge Contact Quality before the Thermal Exchange Reaction

Figure 5.15 shows the plot of the resistance versus Ge segment length measured on the 50 nm diameter Ge NWs without (a) and with (b) passivation shell of 5 nm Al_2O_3. The figure 5.15a shows a strong fluctuation of the resistance over a range of 5 to 25 MΩ for the different Ge NW lengths between the contacts of 800 nm to 1.6 µm. This data indicates that the contact quality varies on every single NW. The other plot on the passivated Ge NWs (Fig. 5.15b) shows a similar behavior; however, the measured resistance is lower than in the un-passivated NWs. Probably, with the HF treatment to remove the Al_2O_3 layer, the surface quality of the contacted NWs was cleaner and maybe the NW diameter was getting thinner underneath and next to the contact, due to the over etching of the strong acid (a HAADF STEM image was shown in section 3.12).

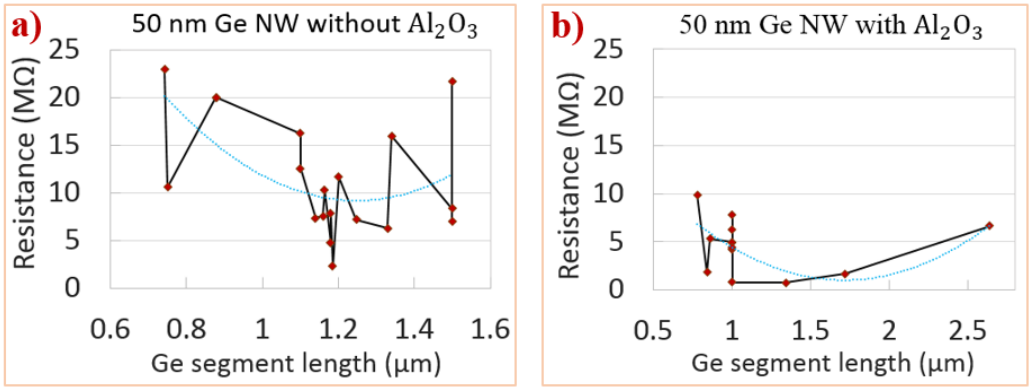

Figure 5.15: The plots of the resistance versus Ge segment length measured on the un-passivated (**a**) and passivated (**b**) Ge NWs with the HF treatment to remove the Al_2O_3 shell at the interface between the NW and the metal contact. The contacted NWs have 50 nm in diameter and are (**b**) passivated by 5 nm Al_2O_3.

In practice, it is recommended to passivate the as-grown NWs by an Al_2O_3 shell for the stability. However, the shell thickness should be considered carefully for the HF etching process to avoid the under-etching effect and the thinning of the membrane support (Si_3N_4).

5.10.2.2 Al/Ge Contact Quality after the Thermal Exchange Reaction

The contacted devices were later annealed by RTA at 300 °C for 20 s (in N_2 gas) to generate the thermal reaction. Since the Al propagating front has advanced from underneath the Al/Ge contact pad, the measured contact resistance will reflect the quality of the Al/Ge cross-section interface. Figure 5.16 shows the plot of the resistance versus Ge segment length measured on a passivated Ge NW. Firstly, we can see a drop of the resistance after the thermal diffusion of Al

metal into the NW. Comparing figure 5.15b and 5.16, with a Ge segment length of 800 nm, the measured resistance before the exchange reaction varies in the range of 2 ~ 5 MΩ while it drops to 1.16 MΩ after the Al incorporation.

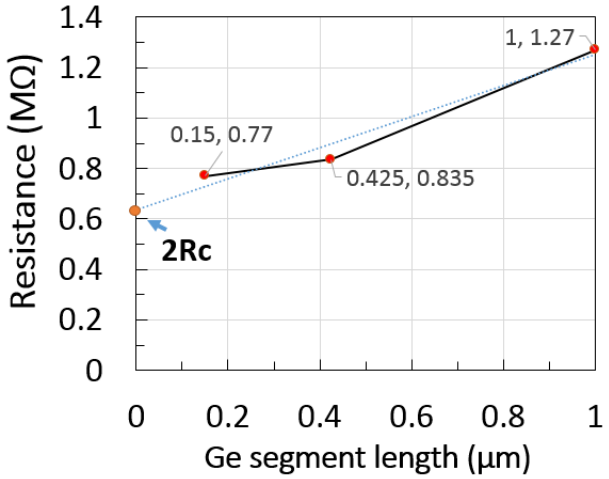

Figure 5.16: The plot of the resistance versus Ge segment length measured on the propagated 50 nm Ge NW with 5 nm Al_2O_3 passivation shell.

Then, we apply the Transfer Length Measurement (TLM) method [118] to calculate the contact resistance of the Al/Ge reaction interface. As shown in figure 5.16, the contact resistance $\boldsymbol{R_c}$ is defined by the intersection of the resistance curve to the zero segment length, which is equal to 3.18 x 10^5 **Ω**. Therefore, the contact resistivity of the Al/Ge interface calculated by the following equation (**23**) is about 6.24 x 10^{-6} **Ω**cm^2. This low resistivity is coherent with the finding on the study of Duan et al [119] where they calculate the resistivity of the NiGe Ohmic contact to n doped Ge.

$$\rho = R_c S_{NW} \qquad (23)$$

In conclusion, comparing the results of figure 5.16 with the resistance measured prior to the thermal exchange reaction, figure 5.15, clearly demonstrates that the exchange reaction both reduces the contact resistance, as well as renders this property of the contact much more reproducible.

5.11 Dopant "Pile-up" in Ge NWs

With the idea of dopant enrichment at the interface of metal/Ge during the propagation, Al metal is considered a promising candidate since a monocrystalline phase is formed at the core of the propagated part, and is expected to push the dopant atoms in the Ge region adjacent to the

moving front. For this experiment, EDX quantification was performed with the data collection from the SEM/EDX machine equipped with a FlatQuad 5060F annular detector working at 4 kV. We used n-doped Ge NWs with the diameters of about 100 - 150 nm and 8 µm length. While the SEM setup has a lower spatial resolution than the TEM based EDX experiments, it is superior for dopant quantification both due to the increased electron matter interaction at much lower acceleration voltage and due to the very large collection angle (1.1 steradians) of the FlatQuad detector for a working distance of 2 mm.

5.11.1 Detection of the n-doped Shell around the Ge NWs

For a reliable analysis, we first checked the characteristics of the n-doped Ge NWs for the doping concentration and dopant distribution, prior to any contacting or annealing steps. The NWs were passivated by 5 nm of Al_2O_3 to protect from the oxidation. The Al_2O_3 shell was also expected to capture the dopants inside the NW during the thermal annealing process. First, we performed the SEM/EDX quantification on the top and bottom parts of three NWs to check the axial dopant distribution in the NWs. Figure 5.17 shows the SEM images with the indicated position of the point spectra obtained by EDX analysis.

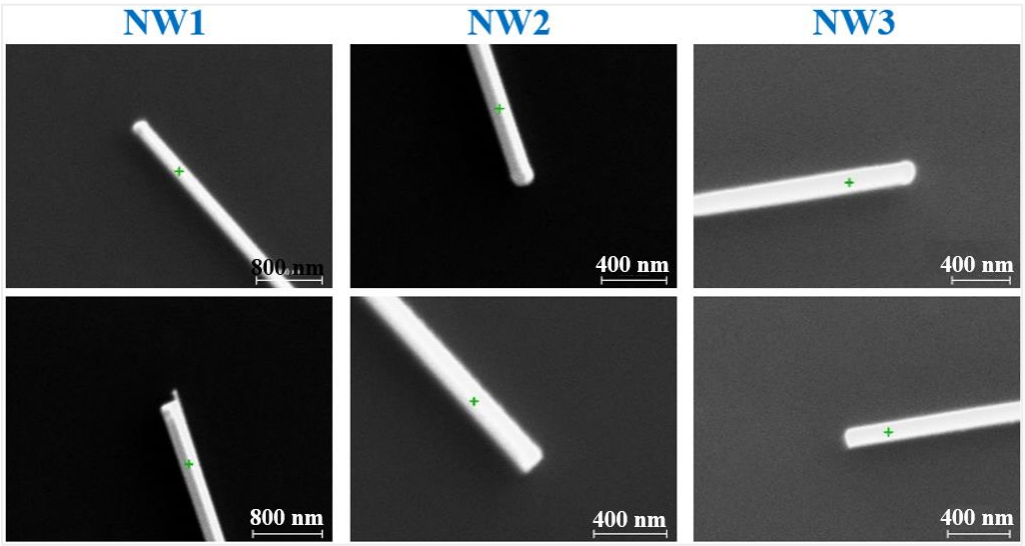

Figure 5.17: Positions of EDX point spectra analysis for the measurement of dopant concentration.

❖ The results of the EDX quantification are presented in table 5.2.

Table 5.2: Measurements of dopant concentration on n-doped Ge NWs.

Ge NWs	Phosphorous concentration (at./cm^3 x 10^{19})	
	Top	**Bottom**
NW1	4.94 ± 0.37	5.89 ± 0.38
NW2	6.25 ± 0.89	7.11 ± 0.91
NW3	5.81 ± 0.7	14.08 ± 0.76
Average	7.35 ± 0.67	

As presented in table 5.2, the average doping concentration on the n-doped Ge NWs is about 7.3 x 10^{19} atoms/cm^3. The axial distribution of dopants (the top and bottom) is quite homogeneous. Then we checked the dopant distribution on the radial axis of the NWs, first in a NW with contacts after the thermally induced Al propagation. From the EDX maps obtained on the FEI Titan Themis at 200 kV, we observed the presence of a highly doped shell on the Ge NW. Figure 5.18 shows the EDX maps of the present elements on the Al/Ge interface of the propagated n-doped Ge NW. Al, Ge and P are represented in red, green and blue, respectively. Figure 5.18b-c compares the spectrum intensities of the phosphorous peak (2 keV) at different regions indicated by rectangular boxes on the shell and the core of the reacted and unreacted part of the Al/Ge interface. Clearly a highly n-doped shell is present around the NW. In addition, the phosphorous content on the Al part seems to be higher than on the Ge part. In literature [68,69], it has been realized that a highly doped shell can be deposited on the doped NWs via the non-catalyzed radial growth process during the NW growth.

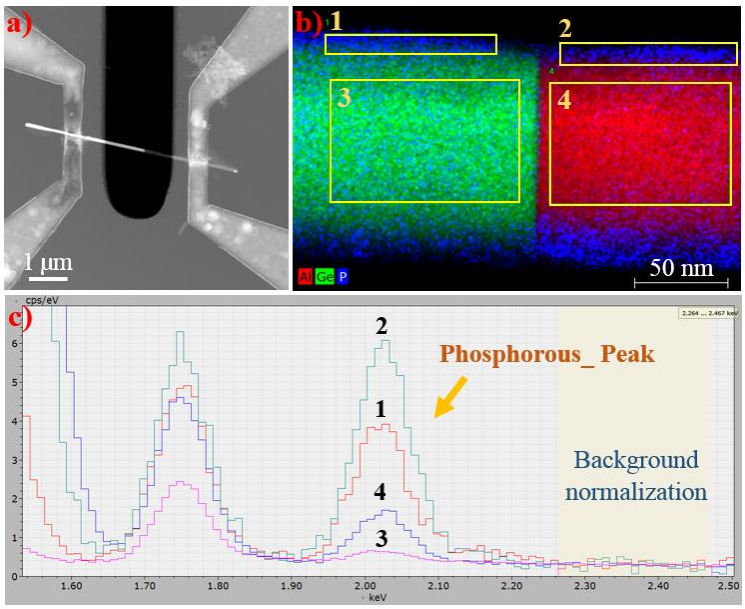

Figure 5.18: EDX spectrum analyses indicate the presence of a highly n-doped shell on the propagated NW. (**a**) HAADF STEM image of the propagated device. (**b-c**) EDX map of the present elements and the integrated spectra taken at different positions shown by the yellow boxes. The orange arrow indicates the position of the phosphorous peak at 2 keV.

We then performed the SEM/EDX quantification on a different propagated Al/Ge interface as shown in figure 5.19a. An EDX line-scan with 10 point analyses was taken crossing the interface from the reacted part to the unreacted part (indicated by the yellow arrow). The plot of the phosphorous (blue curve) and aluminum (red curve) concentration on the line profile is presented in figure 5.19b.

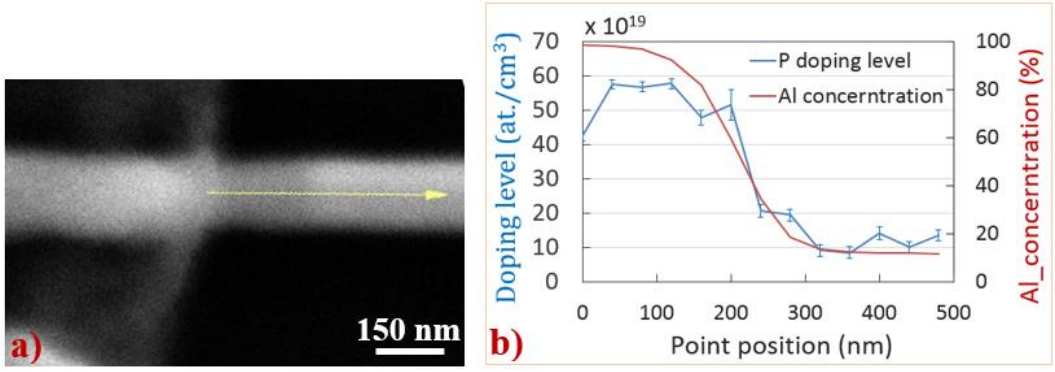

Figure 5.19: (**a**) SEM image of the Al propagated Ge NW used for EDX quantitative analysis. (**b**) Concentration profile of P and Al along the line-scan taken from the reacted part to unreacted part of the NW (indicated by the yellow arrow in Fig. 4.18a). The blue and red curves correspond to the profile of P and Al, respectively.

As shown in the plot in figure 5.19b, the phosphorous concentration drops from the reacted part (Al part) to the unreacted part (Ge part), which is consistent with previous results of EDX maps in figure 5.18.

5.11.2 Removing of n-doped Shell for Phosphorous Concentration Measurement

Since there was a presence of a thick n-doped shell around the NW, it is necessary to remove the n- shell before performing the dopant analysis for a reliable measurement. The process of removing the n-doped shell was described in section 3.3.2. Particularly, the as-grown NWs were dipped in diluted H_2O_2 acid for 15 s to remove about 20 - 30 nm Ge shell. Figure 5.20 shows the EDX mapping of the Ge NW after the etching process. The NW surface was quite rough and appears oxidized. The spectrum analysis made on the shell shows the absence of the P-peak at 2 keV. Therefore, we expect that the n-shell has been fully removed from the NW.

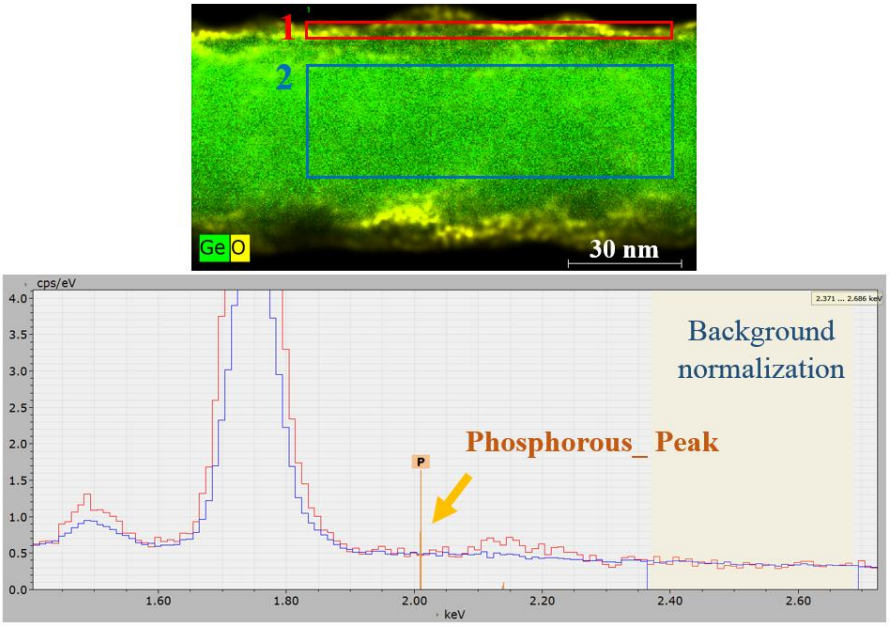

Figure 5.20: EDX map of the Ge NW after etching of the n-doped shell. The spectrum analyses on the shell and the core show the absence of the P-peak at 2 keV.

Then, having removed the n-doped shell, fabrication of contacts and annealing, we performed the SEM/EDX quantification of the phosphorous dopant distribution across the Al/Ge interface. Figure 5.21a shows an SEM image of the propagated Al/Ge interface used for the quantification. Different point analyses were taken from the Al reacted part to the unreacted Ge part along the axial direction (along the yellow arrow). The result of the EDX quantification is presented in figure 5.21b.

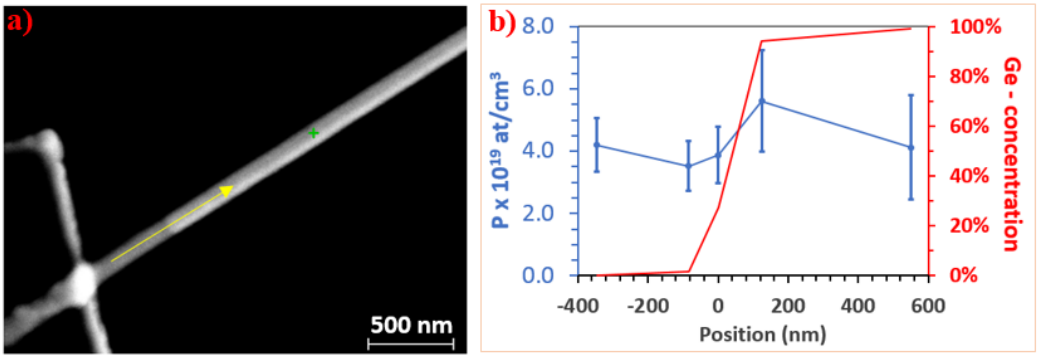

Figure 5.21: (**a**) SEM images of the propagated Al/Ge interface used for EDX point analysis from the Al reacted part to the unreacted Ge part. (**b**) EDX quantification for phosphorous distribution on the propagated Ge NW.

As shown in the plot, the variation of the phosphorous concentration is within the error bars going from the reacted to the unreacted part. The average concentration is about 4 x 10^{19} atoms/cm^3. Similar results were obtained on other analyzed interfaces, which clearly demonstrate that there is no considerable enrichment of the P dopant at the Al/Ge interface.

5.12 Conclusion

In this study, the diffusion behavior of the Al-Ge thermal exchange reaction was fully described from the earliest stage to the end of the exchange process using real-time observations, providing a method to deterministically create a semiconductor region with near atomic scale precision. We observed that at magnifications where lattice planes are visible, the electron beam influences the propagation locally at such a high magnification. It is therefore better to work at a slightly lower magnification, with the additional benefit of having the entire reaction interface within the field of view. Importantly, we have demonstrated the influence of the NW surface quality on the diffusion behavior of Al in a Ge NW. Without the presence of a protecting layer, the Al protruding length shows stepwise growth dependence as a function of time while a much smoother linear time dependence is observed when the NW is covered by a 5 nm Al_2O_3 shell in these relatively large diameter NWs ($120 \leq d \leq 162$). Finally, combining in-situ and ex-situ heating processes, we have successfully controlled and synthesized an ultrashort Ge segment of 7 nm. From literature, this is the smallest Ge segment length that has been obtained in the Al/Ge binary system, and among the smallest segments in other semiconductor NW metal systems.

Chapter 6 :

Solid-State Reaction of Al- (Si, Ge) Ternary System

In this chapter, we report the fabrication of Al/Si/Si_xGe_{1-x} axial heterostructures by the solid-state exchange reaction between a Si_xGe_{1-x} alloy NW and an Al contact pad.

First, a comprehensive review of the literature describing the motivation behind Si/Si_xGe_{1-x} heterostructures and existing limitations in the fabrication processes will be presented. Then, we describe the fundamental knowledge of the solidification process in Al-Si binary and Al- (Si, Ge) ternary system when cooling down the eutectic compounds to room temperature.

Second, experimental results of in-situ and ex-situ observations on Al/Si_xGe_{1-x} alloy thermal exchange are presented in detail. The crystallography and composition of the created heterostructures are investigated by STEM and quantitative EDX analyses with a 3D reconstruction on the reacted and unreacted parts of the propagated NW. Importantly, several parameters such as NW diameter, surface oxide confinement, and cooling temperature are elucidated to understand their influence on the reaction kinetics. Based on these crucial observations, diffusion models are proposed to interpret the kinetics of the thermal exchange reaction in Al- (Si, Ge) ternary system.

Finally, we present the transport measurements on the contacted Si_xGe_{1-x} NWs before and after the metal incorporation with the presence of Al/Si/Si_xGe_{1-x} heterostructures. The exchange reaction results in a significant increase of the contact resistance, which consequently suggests for doping the heterostructures for device applications.

6.1 Background

In the recent years, Si_xGe_{1-x} alloy has attracted considerable interests for its flexible bandgap tuning (from 1.3 µm to 1.55 µm) by adjusting the alloy stoichiometry (Fig. 6.1a) [120], bringing the potential for near infrared (NIR) sensing applications [120–122]. The strained or doped Si/Si_xGe_{1-x} heterostructures provide interesting material structures with novel physical properties such as band offset [121,123] or strong carrier confinement at the heterojunctions (Fig. 6.1b) [124], leading to interesting applications in microelectronics and optoelectronics.

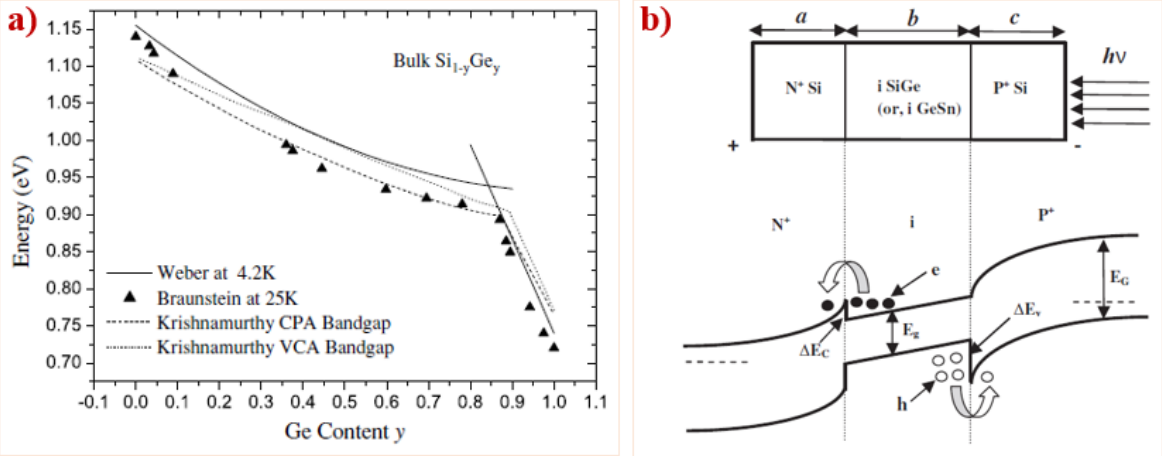

Figure 6.1: (**a**) Bandgap energy of bulk $Si_{1-y}Ge_y$ as a function of Ge content [120]. (**b**) Band diagram of doped Si/SiGe heterostructures (under reverse bias), showing carrier confinement at the interfaces [121].

A great benefit of Si/Si_xGe_{1-x} heterostructures is the compatibility with the existing silicon-based technology. Moreover, unlike most of the III-V material-based detectors that require a low temperature working condition, Si/Si_xGe_{1-x} based detectors can operate at room temperature, which importantly reduces the operation cost. However, due to a large lattice mismatch (4.2%) between Si and Ge, the growth of high quality Si/Si_xGe_{1-x} interface requires novel techniques such as low-energy plasma-enhanced CVD (LEPECVD) [125] or ultrahigh vacuum chemical vapor deposition (UHV-CVD) [126]. These material-growth methods are still an open issue limiting the device applications due to their high cost and complexity. In this work, for the first time, we propose a new approach for producing axial Si/Si_xGe_{1-x} heterostructures, using a thermally activated metal–semiconductor phase exchange reaction. Aluminum, used as a diffusion source to integrate into a Si_xGe_{1-x} NW, could bring a possibility to yield fine $Al/Si/Si_xGe_{1-x}$ heterostructures with tunable

semiconducting channel length through a remarkable reversible diffusion process of Al in the Si_xGe_{1-x} nanowire.

Basic literature on the Al-Ge binary system has been presented in chapter 5. The phase diagram of the Al-Si couple is shown in figure 6.2, demonstrating a hypereutectic point at 577 ^oC for an Al/Si compound with 12.2 wt. % Si. However, by slowly cooling, the maximum solubility of Si in Al falls from 1.64 % just below the eutectic temperature of 577 ^oC to a negligible value at room temperature [127]. Reported in the paper of Mostafa et al [128], the solubility of Al in Si is quite negligible, from 1×10^{-2} at.% at 1327 ^oC to 1.15×10^{-2} at.% at 997 ^oC.

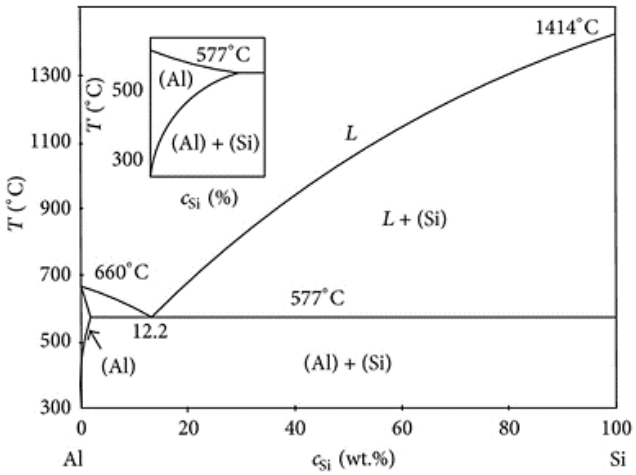

Figure 6.2: Al - Si phase diagram. Ref [127]

Extensive research has been carried out on bulk Al-Si alloys, which have been widely used for several applications in electrical, automobile and aircraft industry [21,127,129–131]. It has been known that when the Si content is beyond the solid solubility limit, it will precipitate in the diamond-structure inside the Al matrix. Indeed, the well-known solidification of Al-Si alloy has been applied in casting industries. A small addition of Si content to Al metal helps to increase the fluidity and reduces the compound's melting temperature. Moreover, the hardness and grain refinement of the aluminum-silicon alloy can be tailored by mixing with other elements such as: iron, copper, magnesium, or titanium [127,132]. From the study of G. J. van Gurp [18] on Si/Al films, he observed the diffusion and precipitation of Si on the grain boundaries and dislocations of the Al matrix. In particular, Hui Song [20] has reported a study of solidification in Al- (Si, Ge) ternary system, where he showed the phase diagram and proposed the kinetics of the morphological

formation at different ternary compounds. Figure 6.3 shows the optical images of eutectic Al- (Si, Ge) structures at different Si/Ge ratios.

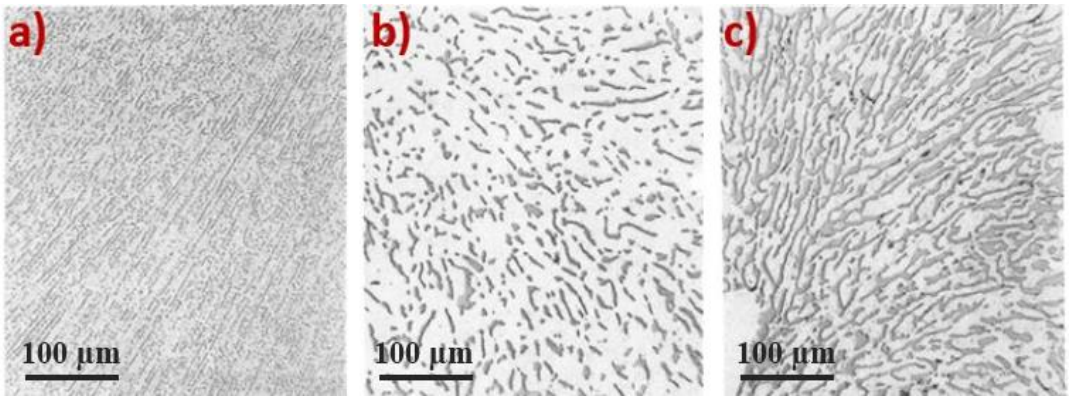

Figure 6.3: Optical images of eutectic structures: (**a**) A1-Si alloy, (**b**) Al-(Si, Ge) compound with 10 wt. %Si, 10 wt. %Ge and (**c**) Al-(Si, Ge) compound with 4.3 wt. %Si and 35 wt. %Ge. Ref [20]

From literature, several studies of thermal diffusion coefficients of Si/Al, Ge/Al and Ge/Si binary have been reported. However, the results are quite diverse due to different investigating conditions and techniques. Table 6.1 summarizes the activation energy and diffusion coefficients of Ge/Al, Si/Al, and Ge/Si at 400 ^{o}C for a comparison.

Table 6.1: Activation energy and diffusion coefficients of Al, Si and Ge at different annealing temperatures.

Diffusion of: in:	**Al**	**Ge**	**Si**	**Ge**
	Al	**Al**	**Al**	**Si**
E_a (kJ/mol)	144	119.4	136 ± 3	509
D_0 (m^2/s)	2.3 x 10^{-4}	3.39 x $l0^{-5}$	2.02 x 10^{-4}	62.6
D (m^2/s)	1.53 x 10^{-15} at 400 ^{o}C Ref [133]	1.85 x 10^{-14} at 400 ^{o}C Ref [19,134]	5.67 x 10^{-15} at 400 ^{o}C Ref [133,134]	10^{-29} at 600 ^{o}C Ref [135]

In a 1D system, there is no report of the Al thermal diffusion in a Si NW while Al can diffuse easily in a Ge NW at low temperature (< 300 ^{o}C). However, the diffusion behavior of the Al- (Si, Ge) ternary can be different from their couples (Al- Si and Al- Ge) due to the difference of atomic radii between Si and Ge atoms. Moreover, as the eutectic temperature of the Al- Si binary is higher than

that of Al-Ge, it is therefore expected that the solid state exchange reaction of Al- (Si, Ge) ternary will occur at higher temperature than in Al-Ge binary.

6.2 Experimental

In this PhD work, we have conducted the thermal diffusion of Al metal into three different Si_xGe_{1-x} alloy stoichiometries (i.e. x= 0.05, 0.12 and 0.67). However, for Al diffusion in low composition Si NWs (x=0.05 and 0.12) no clear difference with the pure Ge NW system was observed, and a strikingly different behavior was observed in the NWs with x= 0.67. Therefore, we decided to focus on the Si_xGe_{1-x} NWs (x= 0.67) in our experiments. The growth of $Si_{0.67}Ge_{0.33}$ NWs was performed by chemical vapor deposition method (CVD) via the VLS growth, using silane and GeH_4 gasses as precursors and gold as catalyst on a Si(111) substrate. The NWs were grown along the [111] direction. The fabricated NWs have a strong fluctuation in diameter, ranging from 65 to 250 nm. The contacting process was performed using the procedure presented in section 5.2 with some modification to adapt to a thicker Al_2O_3 passivated shell and Al metal thickness adapted to the larger NW diameter. Particularly, as-grown $Si_{0.67}Ge_{0.33}$ NWs were either being used directly to perform metal contacts or precedingly passivated by a 20 nm Al_2O_3 shell (using ALD at 250 ^oC). Aiming for in-situ heating experiments, $Si_{0.67}Ge_{0.33}$ NWs were dispersed on calibrated heater chips from DENSsolution company (see section 4.4.2), which contains several 6 μm x 23 μm holes on the SiNx membrane and has the possibility to raise the temperature up to 1300 ^oC within a few seconds. We then selected NWs lying over the holes and contacted both sides by a pair of Al rectangular pads. Prior to the deposition of Al metal layer, NWs with the 20 nm Al_2O_3 shell were immersed in buffered hydrofluoric acid - BOE 7:1 ($HF : NH_4F$ = 12.5 : 87.5%) for 40 s to remove the Al_2O_3 shell in the contact regions and then dipped in diluted hydriodic acid (HI) for 5 s to etch the native GeO_2 shell. After that, the samples were cleaned by soft Ar plasma for 15 s and being coated by a 200 nm Al thick layer using electron beam evaporation (with the purity of 99.995% and in vacuum at a pressure lower than 10^{-6} Torr). The samples were lifted off in acetone solution overnight to obtain the final devices.

For temperature calibrated in-situ heating experiments, the samples were heated inside the TEM microscope using a commercial DENSsolutions six contact double tilt TEM holder. The in-situ heating process was started from room temperature and gradually increased with a 10 ^oC step-jump until reaching 580 ^oC. We then slowly reduced the heating temperature and stopped at certain

temperatures for observation. In this study, $Si_{0.67}Ge_{0.33}$ NWs were also contacted on home-made 200 nm Si_3N_4 membranes for ex-situ heating experiments using rapid thermal annealing (RTA). For the ex-situ heating experiments, several contacted NWs can be propagated at the same condition giving a better statistics of the diffusion behavior. To conduct the thermal exchange reaction, specimens were annealed in a temperature range of 400 to 450 °C in N_2 atmosphere, and rapidly or slowly cooled down to room temperature. The RTA experiments were done in a Jipelec™ JetFirst RTP Furnace. The data of crystallographic and compositional analysis were collected using the FEI Titan Themis microscope equipped with a probe Cs corrector and SuperX EDX (4 SDDs) detectors working at 200 kV.

6.3 In-situ Heating Experiment: Real Time Observation of Thermal Exchange Reaction

To better understand the exchange reaction, it is of great interest to perform in-situ heating experiments for a direct observation of the solid-state reaction. We started with as-grown $Si_{0.67}Ge_{0.33}$ NWs without the passivation Al_2O_3 shell to eliminate the influence of a potential oxide barrier on the diffusion behavior. The heating experiment was divided into two separated processes:

- *The heating process*: the temperature was slowly increased from room temperature to the eutectic temperature of Al/Si (above 577 °C) with steps of 10 °C.
- *The cooling process*: when the Al reaction front had moved out from underneath the contact pad for a certain length, the propagation was intentionally stopped and the heating temperature was slowly reduced down to room temperature with steps of 5 °C. At some moments, the temperature was kept constant for observation.

6.3.1 During the Heating Process: Formation of a Double Interface Region

Figure 6.4 shows the HAADF STEM images of the Al contacted $Si_{0.67}Ge_{0.33}$ NW crossing over a 6 µm x 23 µm hole on the calibrated heater chip before (a) and after the in-situ heating experiment (b). The diameter of the investigated nanowire is about 150 nm with the length of 20 µm. In this experiment, we will elucidate the exchange reaction from the left Al contact pad (indicated by the orange arrow in Fig. 6.4a). The experimental heating profile is plotted in the figure 6.4c. When the heating temperature reached 350 °C, the exchange reaction was recognized by the HAADF STEM contrast changing underneath the Al contact pad. A real time observation of the reaction interface is presented in the SI M6.1, recorded at 540 °C. It is worth noting that the propagation length will stop after a certain time when the temperature is kept constant. Therefore,

to spread the reaction interface over the hole on the SiN_x membrane, the temperature was increased often during the heating process. Surprisingly, when magnifying the reaction interface, we observed the presence of a double interface region (with an intermediate HAADF intensity shown in the inset of Fig. 6.4b acquired at 550 ºC) sandwiched between the reacted and unreacted parts of the NW.

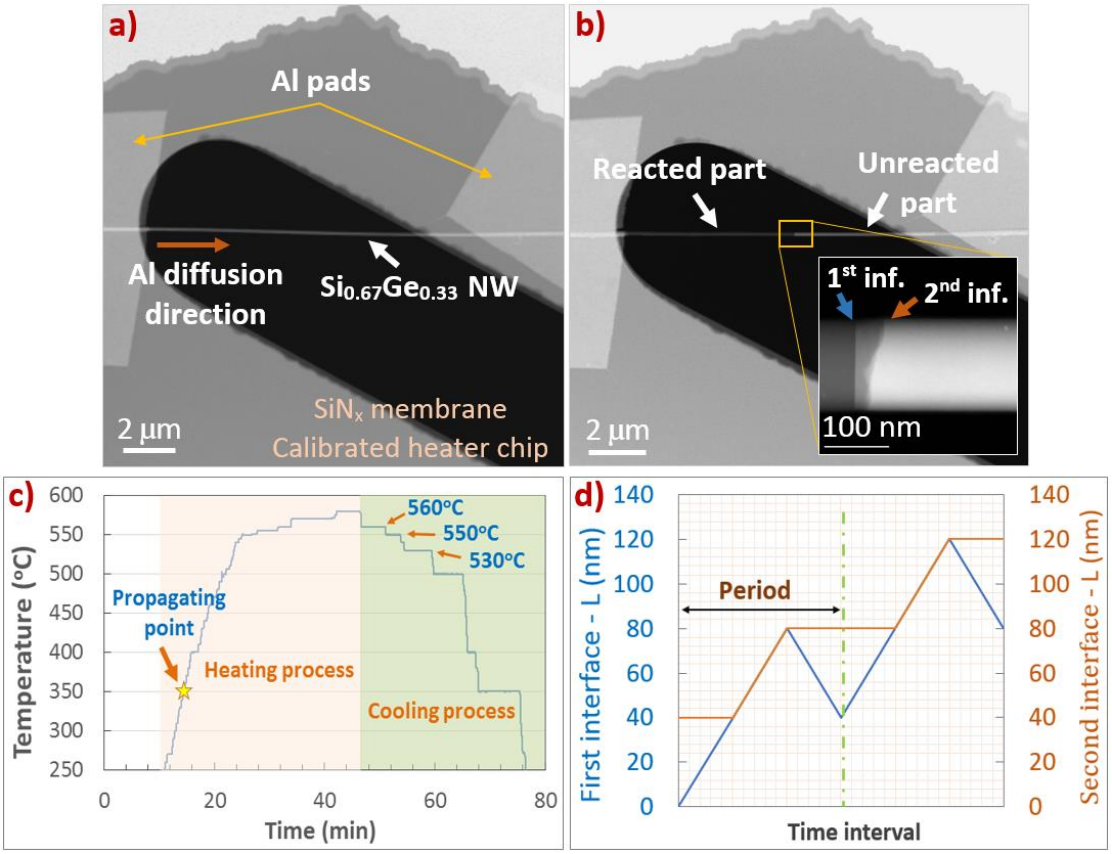

Figure 6.4: a-b) HAADF STEM images of the Al contacted $Si_{0.67}Ge_{0.33}$ NW crossing over the 6 µm x 23 µm hole on the SiN_x membrane before and after the in-situ heating experiment, respectively. The insertion in figure 5.4b shows the formation of a double interface region sandwiched between the reacted and unreacted parts of the NW, image taken at 550 ºC. **c**) The plot shows the temperature profile during the heating and cooling process. The solid-state reaction was initiated at 350 ºC, recognized by the HAADF contrast changing underneath the Al contact pad. **d**) The schematic illustration of the relative positions of the 1st and 2nd interfaces during the heating process. The real time observation of the exchange reaction is presented in the supporting information SI M6.1, recorded at 540 ºC.

For convenience, we shall call the left interface between the reacted part and the double interface region the **1st interface** (marked in blue color) and the one between the double interface region and the unreacted part the **2nd interface** (in orange color). The kinetic behaviors of the two reaction interfaces along the NW axis are very dramatic. Firstly, the propagation of the 2nd interface (the unreacted $Si_{0.67}Ge_{0.33}$ interface) is not continuous, but is showing a step-wise propagation with a very rough interface. The diffusion of the 1st interface is even more surprising with a forward and then backward propagation by relatively large (nm) sized steps. Moreover, the 1st interface is typically better defined during the propagation. The plots in figure 6.4d demonstrate the relative positions of the two interfaces over certain time intervals. Due to the random behavior of the interface, the time axis in figure 6.4d is not linear but adapted to show the forward and backward movement of the first interface. The plot demonstrates that the two interfaces are halted at the same position along the NW and that the two interfaces can momentarily catch up, to be a single interface, after which suddenly the 1st interface moves backward to generate a new double interface segment along the NW axial direction.

6.3.2 During the Cooling Process

When the reaction front had spread out of the left Al contact pad for about 7 μm length (the heating temperature reached 580 °C), we decided to stop the propagation and lowered the temperature slowly to room temperature. In addition, we stopped and kept the temperature constant for some time at three different points, i.e., 560, 550 and 530 °C to observe the evolution of the double interface region. Surprisingly, while the 2nd interface didn't show any change in either the position or shape, the 1st interface showed an elongation in the reversed direction (from the right to the left) back to the Al contact reservoir. The movie of the backward diffusion of the 1st interface is presented in supporting information SI M6.2 at 560 °C. Consequently, the length of the double interface region is extended toward the Al pad, which is clearly observed by the change of the HAADF intensity shown in the figure 6.5a. Figure 6.5b shows the diffusion length of the 1st interface as a function of time during the cooling process with respect to three different temperatures (i.e., 560, 550 and 530 °C). The plots demonstrate a linear diffusion behavior with an increase of the slope related to the decrease of the temperature. Furthermore, during the backward diffusion of the 1st interface, structural defects (twin boundaries) were formed in the crystal structure of the double interface region (a HR-STEM image at the NW surface with the corresponding FFT is shown in the inset of figure 6.5a). These defects started from the surface and

ran through the NW cross-section along the [111] direction. Moreover, there was a shrinkage of the NW diameter from 155 nm to 148 nm after the backward diffusion. The 1st interface extended up to 4.7 µm length in the reversed direction, and then we observed a change in the HAADF contrast in the last 1.6 µm until reaching the Al metal pad. The increase of the HAADF intensity at the moving 1st interface implies an increase in the mass density of the structure (or the thickness, but no modification in the diameter compared to the previous phase is observed), which in this case indicates an increased presence of Ge atoms. When the interface reaches the Al reservoir, a large crystal was suddenly formed at the Al pad (shown by the blue arrow in Fig. 6.5c). EDX mapping was performed at the created crystal, which interestingly shows that the crystal is mainly Ge (see figure 6.5d). The real time observation of the island formation is presented in the supporting information SI M6.3 at 500 °C.

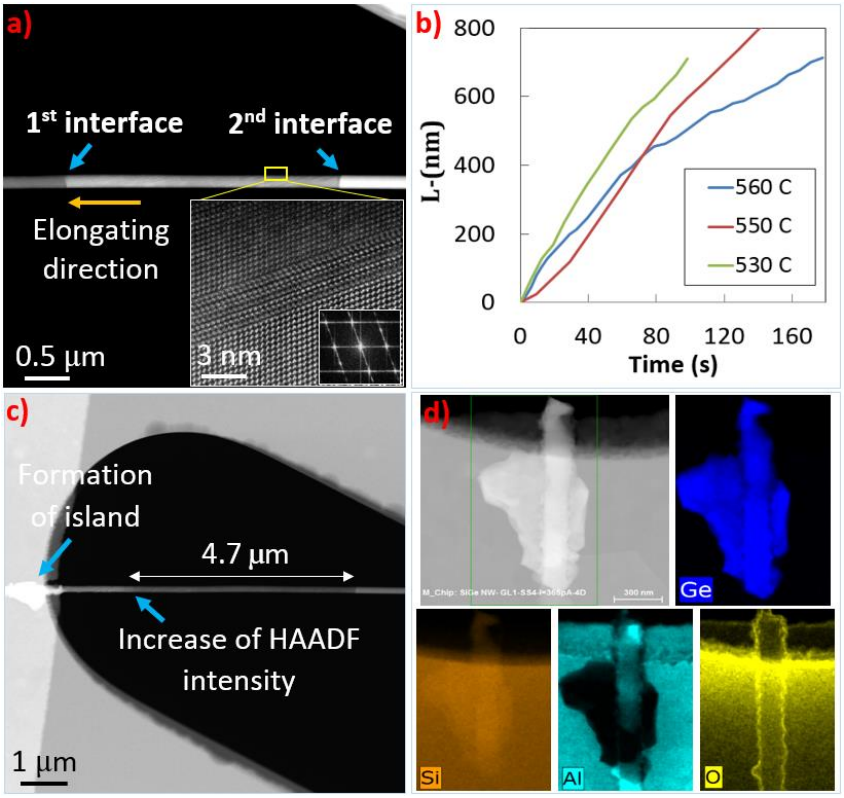

Figure 6.5: a) HAADF-STEM image of the propagated NW showing the backward diffusion of the 1st interface during the cooling down of the heating temperature, acquired at 530 °C. A zoom on the top surface of the double interface region shows the formation of structure defects running across the NW diameter. b) The plots of the diffusion length as a function of time at three different temperatures demonstrating a linear diffusion behavior of the 1st interface during the cooling process. c) HAADF-STEM image of the propagated NW showing the presence of two different HAADF contrast regions and formation of a large crystal when the interface reaches the Al contact

reservoir. d) EDX mapping at the crystal showing that it is mainly constituted of Ge. The real time observation of the island formation is presented in the supporting information SI M6.3, recorded at 500 °C.

6.4 Ex-Situ Heating Experiment: The Formation of Al/Si/$Si_{0.67}Ge_{0.33}$ Heterostructures

An in-situ heating experiment is very interesting for the direct observation of the thermal exchange reaction. However, due to a limitation in the field of view only one or two NWs can be characterized in an experiment, complicating the understanding of the more general diffusion behavior of the system. To obtain more statistics, we also contacted several $Si_{0.67}Ge_{0.33}$ NWs on home-made Si_3N_4 membranes to elucidate the thermal exchange behavior of a group of NWs. Figure 6.6 shows HAADF STEM images of the Al contacted $Si_{0.67}Ge_{0.33}$ NW crossing over the 2 µm x 8 µm hole on the 200 nm thick Si_3N_4 membrane. The NW diameter is about 68 nm with a 7.2 µm length. The exchange reaction was generated by ex-situ heating via RTA at 400 °C for 20 s, 400 to 300 °C for 30 s and cooled down to the room temperature during 4 min.

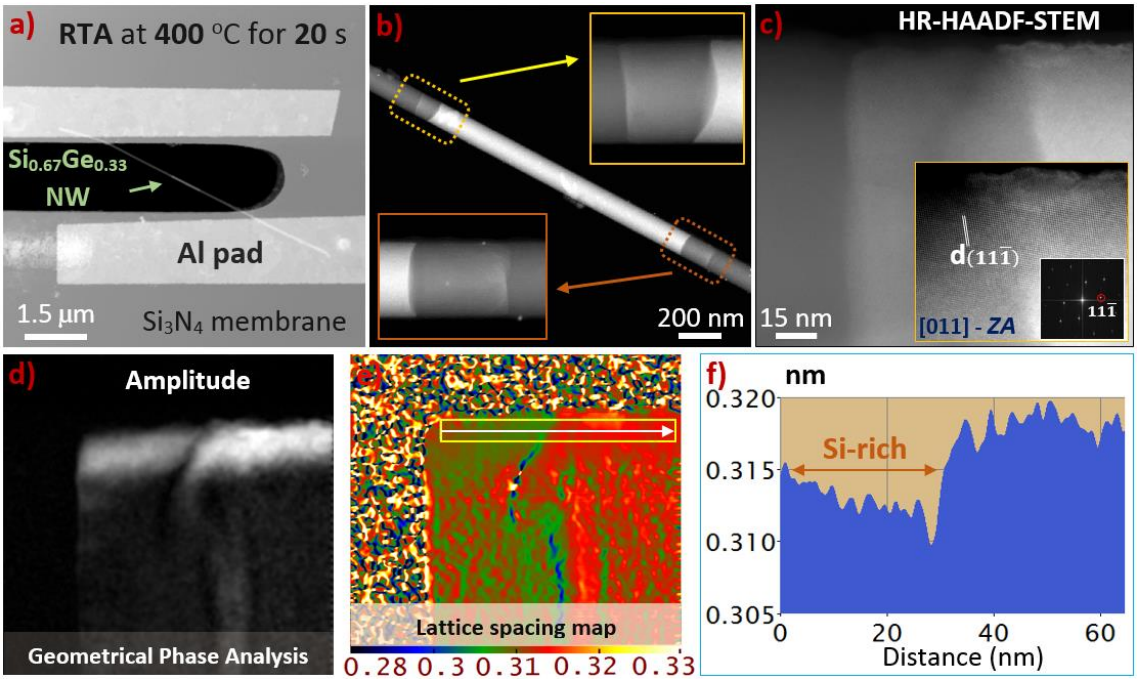

Figure 6.6: a) HAADF STEM image of the Al contacted $Si_{0.67}Ge_{0.33}$ NW crossing over the 2 µm x 8 µm hole on the 200 nm thick Si_3N_4 membrane. **b**) A zoom at the middle part of the NW showing the formation of the top and bottom double interface regions sandwiched between the reacted and unreacted part of the $Si_{0.67}Ge_{0.33}$ NW. **c**) The HR-HAADF-STEM image with zoom and corresponding FFT in the inset taken at the double interface on a different propagated NW, used for geometrical phase analysis (GPA). **d-e**) The amplitude and lattice spacing map of the HR-

STEM image extracted by GPA technique. **f**) The lattice spacing profile taken on the yellow box in figure 5.6e demonstrating the variation of the lattice spacing between the double interface region and unreacted $Si_{0.67}Ge_{0.33}$ NW.

Shown by the dark contrast region in figure 6.6a, about 2 µm and 1.5 µm of the $Si_{0.67}Ge_{0.33}$ segment length on the top and bottom of the contacted nanowire have been replaced by Al metal, respectively. Zooming on the top reacting interface, we can see the presence of a double interface region (indicated by the dash yellow box in Fig. 6.6b) with a length of about 60 nm in the NW axial direction. The bottom double interface region is marked by the orange box with a segment length of 85 nm. It is worth noting that both the Al propagation length and the created double interface region are not respectively equal in the top and the bottom positions even though passing through a nominally identical sample preparation process and heating conditions. Considering the top double interface region (the yellow box in Fig. 6.6b), there is a gradient of the HAADF intensity from the 1st interface to the 2nd interface. This indicates a compositional variation in this local region. The bright spots present on the NW surface are contamination: Si crystals coming from the fabrication process.

To analyze the double interface region, we first used geometrical phase analysis (GPA) technique to determine the lattice spacing of the crystal. The experimental data were elucidated using the digital micrograph interface with a script written by Rouvière et al [98]. Firstly, a HR-STEM image was taken at the double interface region, which was formed in a different propagated NW (see Fig. 6.6c). The amplitude and lattice spacing maps on the [11-1] reflection of the HR image were extracted and presented in figure 6.6d-e, respectively. As shown in the amplitude image, the atomic planes are more visible at the edge of the nanowire since this region is thinner than the middle part. Figure 6.6f presents the lattice spacing profile extracted from the yellow box region in the phase image (Fig. 6.6e). The line profile shows a lattice spacing gradient from the 1st interface to the 2nd interface, which is coherent with the gradient in HAADF intensity in figure 6.6b. Moreover, the variation of the lattice constant is very close to the theoretical lattice spacing of Si(111) plane families (0.313 nm), which implies for a main contribution of Si atoms in this region. The brighter contrast region of the original NW has larger lattice spacing (about 0.318 nm), which demonstrates for a mixing of both Si and Ge atoms.

6.5 Quantitative EDX: Compositional Analysis of Al/Si/$Si_{0.67}Ge_{0.33}$ Heterostructures

For a quantitative analysis of the structure composition, EDX maps were acquired for about 30 min on each region of the created heterostructures. Figure 6.7 shows EDX quantification for the top heterostructures presented in figure 6.6b (indicated by the yellow box). The distribution of Al, Si, Ge and O elements were displayed in turquoise, orange, blue, and yellow, respectively. Figure 6.7a presents a line profile crossing the double interface region from the Al reacted part to the unreacted $Si_{0.67}Ge_{0.33}$ part. The normalized concentration profile in atomic percent (at. %) was extracted using QUANTAX-800 software from BRUKER, showing a transition from an Al part to a Si-rich region and then the $Si_{0.67}Ge_{0.33}$ original part. It is obvious that the double interface region is mainly made of Si atoms. In addition, we observe a small gradient of Ge concentration from the first interface to the second interface, which is coherent with the HAADF intensity variation found in figure 6.6b. The 3D reconstructions of the NW cross-section on each particular region (using the modeling method written by Eric et al [136]) are presented in figure 6.7b-d. Figure 6.7b presents the mapping, radial line-profile and 3D reconstruction of the original $Si_{0.67}Ge_{0.33}$ NW. Firstly the line-scan profile in the cross-section direction demonstrates the presence of a homogenous $Si_{0.67}Ge_{0.33}$ core which is then covered by an oxidation shell. Quantitatively the as-grown NW has a $Si_{0.67}Ge_{0.33}$ core with the asymmetric diagonals of 74.3 nm and 65.4 nm. It is covered by 0.5 nm of thin Ge-rich shell (~ 43%) and 1 nm SiO_2 shell. Probably, the presence of the inner Ge-rich shell results from the hydriodic acid (HI) etching process which only removed the native GeO_2 but not the stable SiO_2 shell. EDX quantification for the Si-rich region is shown in figure 6.7c. In the core part, there is an uphill diffusion of the Si concentration from the original part (67% Si) up to $\geq$ 90%. This region is also composed of small proportions of 5 - 6%Ge and 0 - 2%Al. It should be noted that the finding of ~ 2%Al can be an artifact due to the scattered signals of Al from large Al contact pads. Besides, Al atoms may also diffuse into the structure defects present in the Si-rich segment (as shown in Fig. 6.5a). The outer shells are composed of a thin Ge-rich shell of 8% (about 1 nm) and then the mixture of Al_2O_3 and SiO_2 shell, about 2 nm. The presence of Al atoms in the core and shell part has importantly proved that the Al reaction front had reached the $Si_{0.67}Ge_{0.33}$ interface and was pushed back during the formation of the Si-rich region. Figure 6.7d shows the compositional analysis on the reacted part of the NW. The converted region has an Al core owning a noticeable 4%Si and small percent of Ge (about the quantification limit). The outer shell consists

of about 1 nm Ge-rich shell and 1-2 nm of mixing Al_2O_3 and SiO_2 shell. There is also a small shrinkage in the size of the Si-rich and Al reacted parts compared to the original size of the NW.

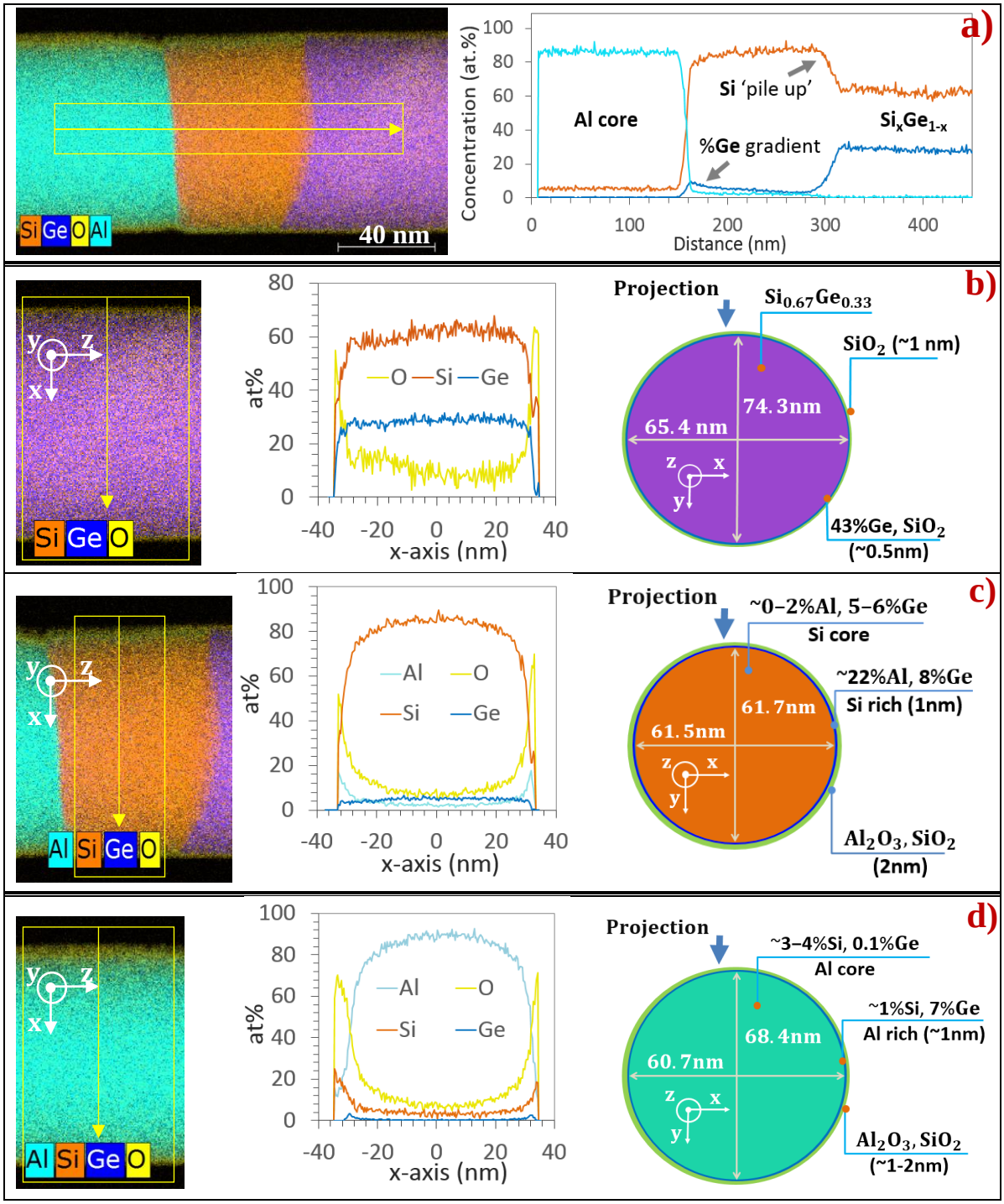

Figure 6.7: EDX mapping on the created heterostructures shown in figure 6.6b (the yellow box). **a)** EDX hyper-map and line-scan profile crossing the heterostructures from the reacted, double interface region and unreacted $Si_{0.67}Ge_{0.33}$ part. **b-d)** EDX quantification on three different parts of the heterostructures, showing the chemical map, 3D

reconstruction and chemical profile, respectively. The vertical arrow indicates the projection direction of the elliptic reconstruction model.

6.6 Influence of NW Diameter on the Diffusion Rate

For the interpretation of the diffusion kinetics, it is of key importance to understand the influence of the NW diameter on the propagation rate of the reaction interface. Reported in the theoretical work of Ogata et al [29], the dependence of the metal intrusion length (***L***) upon the annealing time (***t***) and NW radius (***R***) can give the cue to identify the mechanism of the exchange reaction (see section 2.1.2). We presented in chapter 5 on the thermal exchange reaction of Al/Ge NW binary, that the influence of large NW diameter (≥ 100 nm) on the diffusion behavior is still unclear due to the contribution of several parameters such as contact quality and surface confinement. In this experiment, we again contacted several $Si_{0.67}Ge_{0.33}$ alloy NWs with a wide variety of NW diameters (from 60 – 250 nm) to elucidate the size dependence on the propagation behavior. Prior to the metal deposition process, the NW contacted surface was cleaned by hydriodic acid (HI) and Ar plasma to optimize the contact quality and reduce its influence on the diffusion speed. Moreover, the thickness of the Al metal pad was increased to 300 nm to assure a complete coverage of the NW cross-section. The exchange reaction was generated by ex-situ heating (RTA) at 450 °C for 20 s, 450 to 300 °C for 30 s and then cooled down to the room temperature during 4 min. The plot of the Al intrusion length (***L***) versus the NW diameter is presented in the figure 6.8.

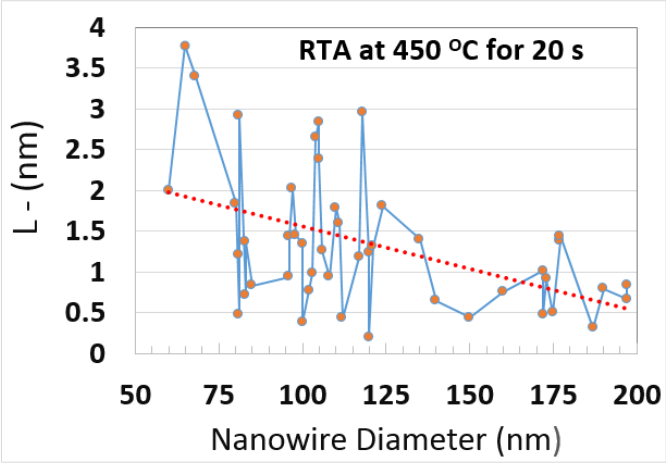

Figure 6.8: Al propagation length versus the $Si_{0.67}Ge_{0.33}$ NW diameter.

The data points however illustrate a strong fluctuation, which may demonstrate a large variation of the Al/$Si_{0.67}Ge_{0.33}$ NW contact quality. However, we may also recognize an ambiguous tendency

that the Al reacted length decreases on larger nanowire diameters (shown by the average red line). In this ex-situ RTA experiment, we have seen a clear influence of the NW diameter on the $Si_{0.67}Ge_{0.33}$ interface shape. Particularly, small NWs with diameters ranging from 60 to 100 nm show the formation of a clean $Si_{0.67}Ge_{0.33}$ interface with a straight or more often observed, convex shape. Larger NW diameters (150 – 200 nm) however show the presence of a very rough interface with different facets (shown in Fig. 6.9). In addition, we observed a large scatter of the Si-rich segment length in both small and large diameter NWs.

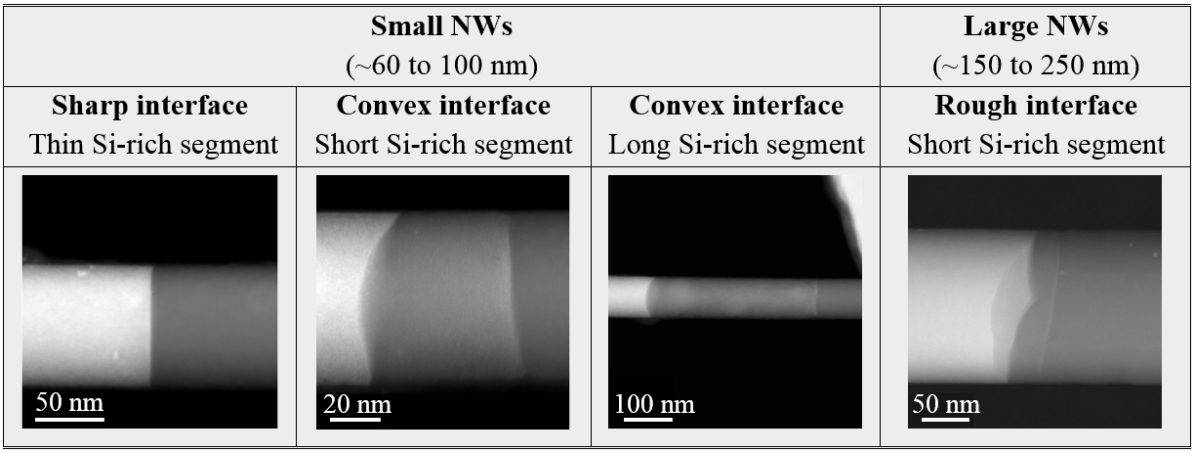

Figure 6.9: HAADF STEM images of propagated NWs having different NW diameters. The NWs with diameter in range of 60 to 100 nm show the formation of a clean $Si_{0.67}Ge_{0.33}$ interface with a straight or more often observed, convex shape. Larger NW diameters (150 – 250 nm) however show the presence of a very rough interface with different facets.

6.7 Influence of the Cooling Speed on the Si-rich Segment Length

From different heating recipes and the in-situ experiment, it appears that the variation of the Si-rich segment length is not only related to the NW diameter, but also strongly determined by the cooling procedure during the annealing process. To confirm this conclusion, we have annealed the specimens at 450 ^{o}C for 10 s, and then cooled down by two different recipes, i.e., (i) by rapidly decreasing the temperature from 450 to 300 ^{o}C for 30 s and then cooling down to room temperature during 4 min. (ii) by slowly reducing the temperature with several steps: from 450 to 440 ^{o}C for 30 s, 440 to 420 ^{o}C for 30 s, 420 to 300 ^{o}C for 30 s and then cool down to room temperature during 4 min. Figure 6.10 shows the comparison of the Si-rich segment length between the two cooling processes.

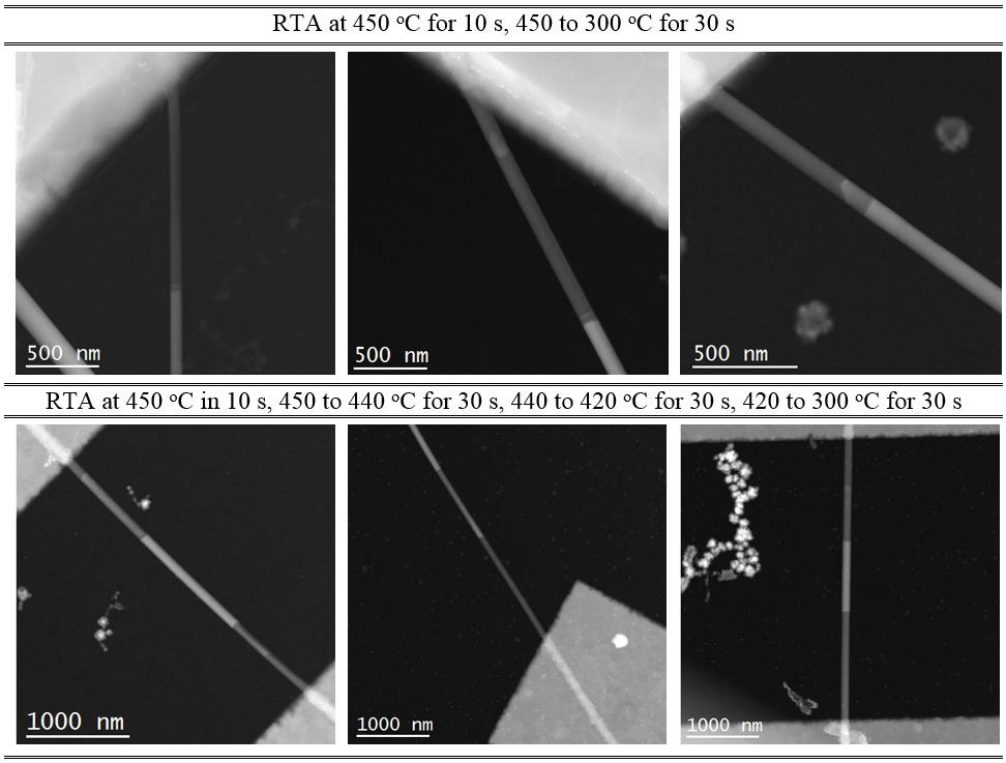

Figure 6.10: HAADF STEM images of propagated NWs when applying two different cooling processes. **a**) 450 °C for 10 s, 450 to 300 °C for 30 s, cooled down to room temperature during 4 min. **b**) 450 °C for 10 s, 450 to 440 °C in 30 s, 440 to 420 °C for 30 s, 420 to 300 °C for 30 s and then cooled down to the room temperature during 4 min.

In the first batch of specimens treating by a rapid cooling process, the diffusion length of Al into the as-grown $Si_{0.67}Ge_{0.33}$ NWs varies in a range of 1 – 1.5 µm. The Si-rich region appears quite short, about 50 – 100 nm. Besides, we can observe the HAADF contrast gradient in the Si-rich segments, showing the accumulation of Ge atoms at the propagating front of the Si-rich interface. On the other hand, specimens undergoing the long cooling procedure show a longer Al conversion length and Si-rich segment compared to the former case. The Si-rich segment length is about 10 times larger than that of the specimens with the rapid cooling process.

6.8 Influence of Al_2O_3 Shell on the $Si_{0.67}Ge_{0.33}$ Interface Shape

In the chapter 5, we have pointed out the important role of an Al_2O_3 passivation shell on the reaction kinetics. For the Al/$Si_{0.67}Ge_{0.33}$ NW system a similar influence of such a passivation shell may also occur. Therefore, we have contacted passivated $Si_{0.67}Ge_{0.33}$ NWs (having 20 nm Al_2O_3 shell) on both Si_3N_4 membranes and calibrated heater chips for ex-situ and in-situ heating experiments, respectively. The sample preparation started with the cleaning of the as-grown NW surface by dipping in diluted hydriodic acid (HI) for 5 s and the sample was then immediately coated by 20 nm of Al_2O_3 (ALD at 250 ^oC). Due to the addition of a thicker Al_2O_3 layer, a 40 s of HF etching (followed by HI etching and Ar plasma cleaning) was also performed prior to the deposition of 300 nm Al metal pads. The thermal reaction was first elucidated by ex-situ heating via the RTA technique. The heating process was performed at 450 ^oC for 20 s, 450 to 300 ^oC for 20 s and cooled down to room temperature during 4 min. Figure 6.11a shows the HAADF STEM image of a contacted 77 nm $Si_{0.67}Ge_{0.33}$ NW with a 20 nm Al_2O_3 passivation shell after the thermal treatment.

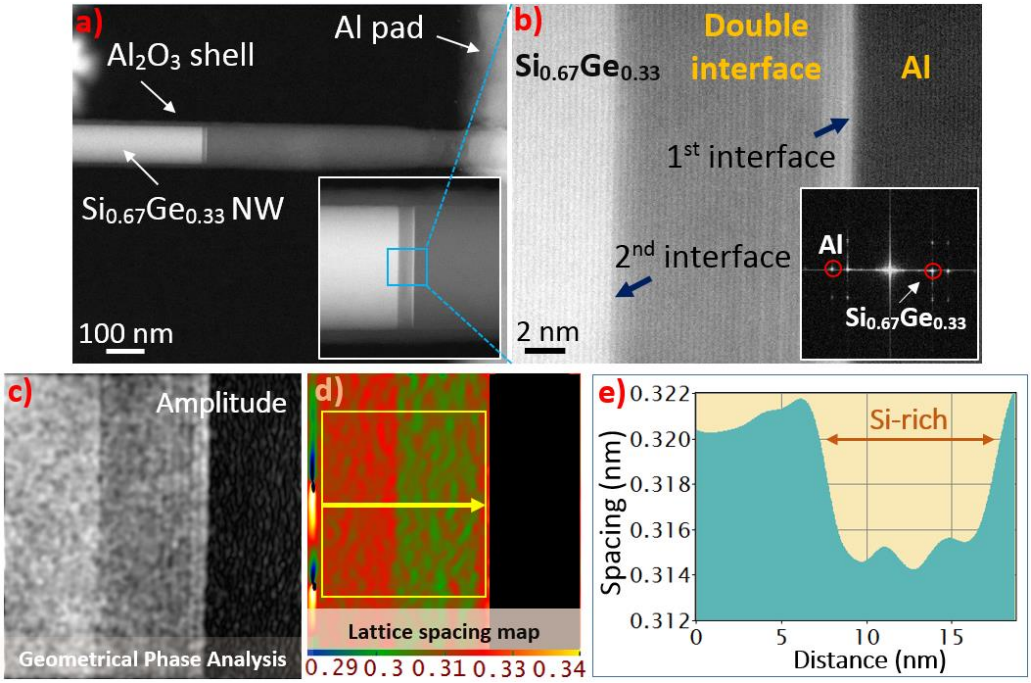

Figure 6.11: a) HAADF - STEM image of propagated NW showing the formation of Al/Si-rich/$Si_{0.67}Ge_{0.33}$ heterostructures. **b**) HR - HAADF - STEM image with the corresponding FT image taken on the blue box in figure 6.11a, showing abrupt interfaces of Al/Si-rich and Si-rich/$Si_{0.67}Ge_{0.33}$ along the (111) atomic planes. **c-d-e**)

Geometrical phase analysis for the HR-STEM image, showing the amplitude, phase and average lattice spacing profile taken on the yellow box, respectively.

The Al conversion length is about 650 nm from the Al contact pad, and the created Si-rich segment is around 14 nm. Figure 6.11b shows the magnified image taken in the blue box (Fig. 6.11a), showing the alignments of Al(111)//Si-rich(111) and Si-rich(111)//$Si_{0.67}Ge_{0.33}$(111) planes. Especially we can observe a high HAADF contrast region between the Si-rich region and Al reacted part (about 5 atomic planes). Figure 6.11c-e presents the results of GPA analysis, demonstrating the transition from a $Si_{0.67}Ge_{0.33}$ part to Si-rich part with an increase of the lattice spacing at the end. Observations in other propagated NWs (with different NW diameters) showed that the Si-rich region appeared shorter or even disappeared compared to the case of propagated NWs without the passivation shell in a similar annealing condition. $Si_{0.67}Ge_{0.33}$ NWs with 20 nm Al_2O_3 shell were also contacted on calibrated heater chips to have a direct observation of the thermal diffusion. Figure 6.12a-b show the HAADF STEM images of the contacted $Si_{0.67}Ge_{0.33}$ NW crossing over a hole before and after the thermal diffusion.

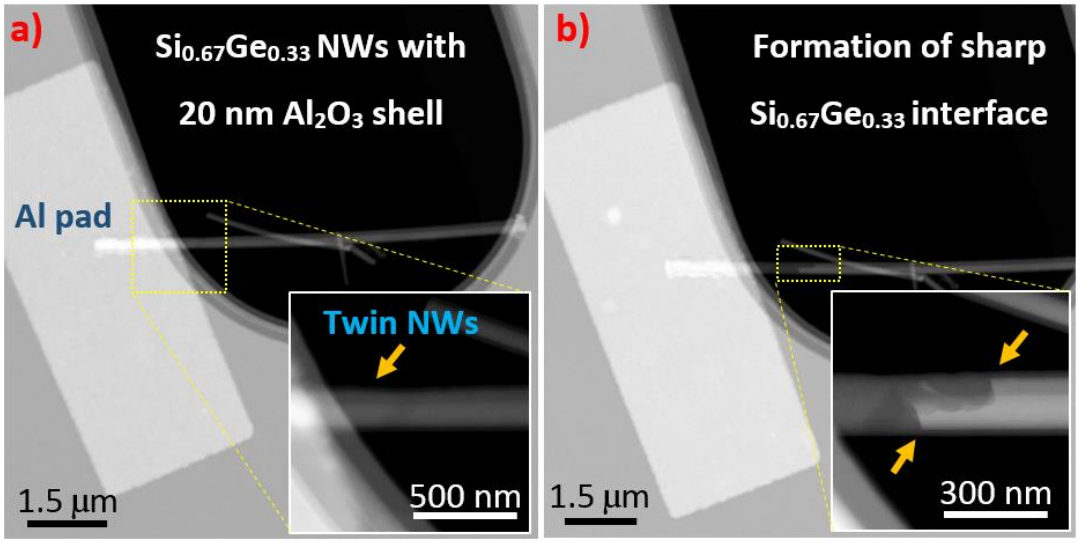

Figure 6.12: HAADF STEM images of the Al contacted $Si_{0.67}Ge_{0.33}$ NW with 20 nm Al_2O_3 shell crossing over a hole on the SiN_x membrane before (**a**) and after (**b**) the thermal diffusion at 590 °C. The contacted NW is a double NW with two NWs side by side. The exchange reaction occurred in both NWs with different diffusion rates leading to the appearance of two reaction interfaces.

Shown by the zoomed image in figure 6.12a, the contacted NW is in fact two NWs side by side. The real time propagation of the contacted NW at 590 °C is presented in the supporting information SI M6.4. The exchange reaction occurred with different diffusion rates in both NWs, leading to the appearance of two reaction interfaces. As can be seen from the movie, the propagation is smoother than the step-wise propagation in the as-grown NW from the previous in-situ observation in section 6.3. Moreover, the interface shape appears very sharp with shorter Si-rich region. This can be a strong evidence confirming the important influence of surface quality on the reaction interface kinetics. Probably, the cleaning process has mostly removed the defect states on the NW surface, giving a smooth and uniform exchange reaction along the NW axial and radial direction. Again, the reaction interface has further advanced in the smaller diameter NW.

6.9 Thermal Exchange Reaction in Large NW Diameters (≥ 150 nm)

Based on above observations of the thermal diffusion behavior, we propose some hypotheses to interpret the diffusion kinetics of the thermal exchange reaction for the formation of the Al/Si/$Si_{0.67}Ge_{0.33}$ heterostructure. Turning back to the in-situ heating results presented in section 6.3, we specify that the 1st interface is the interface between the Al reacted part and Si-rich region (we call it the "Si-rich interface"). The 2nd interface is the one between the Si-rich region and the unreacted $Si_{0.67}Ge_{0.33}$ part (or the $Si_{0.67}Ge_{0.33}$ interface).

6.9.1 During the Heating Process

From the SI M6.1, the two interfaces move forward catching up with each other after a certain time, and then the $Si_{0.67}Ge_{0.33}$ interface suddenly stops while the Si-rich interface moves backward to generate a new Si-rich region. Firstly, the step-wise propagation of the $Si_{0.67}Ge_{0.33}$ interface may be explained due to defect states on the NW surface that trap the interface. The result of quantitative EDX analysis has shown the presence of about 1 – 2 nm of SiO_2 shell covered around the NW. Since the as-grown NW was exposed to air, the NW surface was strongly oxidized resulting in the formation of surface defects. The trapping and de-trapping of the reaction interface at these states may cause the discontinuous propagation of the $Si_{0.67}Ge_{0.33}$ interface. This hypothesis was corroborated by the formation of a clean and sharp $Si_{0.67}Ge_{0.33}$ interface when passivating the NWs by a 20 nm Al_2O_3 shell.

Then, the Si-rich interface shows a backward diffusion after the $Si_{0.67}Ge_{0.33}$ interface had stopped. Since the $Si_{0.67}Ge_{0.33}$ interface stopped moving and the interface shape didn't change

during the backward diffusion of the Si-rich interface, clearly Si atoms came from the Al reacted side. From the statistics presented in table 6.1, the diffusion coefficient of Ge in Al is higher than Si in Al at the annealing temperature. Therefore, Ge atoms from the unreacted $Si_{0.67}Ge_{0.33}$ part move through the surface channel on the Al reacted part and incorporate at surfaces and grain boundaries in the Al reservoir faster than Si atoms, leaving a diffusion channel (on the surface or in the volume of the Al reacted part) with high Si concentration. From the EDX analysis, we observed about 4% of Si content in the Al reacted part (higher than the solubility limit of Si in Al, 1.64%), this part may be saturated by Si atoms. The saturation of Si content in the diffusion channel results in the precipitation of Si at the $Si_{0.67}Ge_{0.33}$ interface, forming the Si-rich region in an in-equilibrium state. It was observed that the Si-rich interface always tries to maintain a sharp interface. This can be due to the low solubility limit of Si in Al forcing Si atoms to move out of the Al core and surface and "pile up" at the $Si_{0.67}Ge_{0.33}$ interface. The Si-rich region then acts as a barrier layer preventing Ge atoms from further diffusion toward the Al reservoir and hence the $Si_{0.67}Ge_{0.33}$ interface remains unchanged during the presence of the Si-rich region. When the Si content in the diffusion channel drops below the solubility limit after a certain time, the Si-rich segment gradually disappears and the $Si_{0.67}Ge_{0.33}$ interface again starts a new cycle of propagation. It is also observed that there is a gradient of Ge content in the Si-rich region with a maximum at the Al/Si-rich interface. This can be due to the low solubility limit of Ge in Al, pushing Ge atoms toward the Al/Si-rich interface and into the structure defects on the new-formed Si-rich segment. An alternative hypothesis can be that forming an interface between monocrystalline Al and Si is energetically not allowed at the experimentally accessible temperature. Therefore, to decrease the energy of the interface, the Ge content must increase at the Al interface. This would also explain why the exchange reaction was never observed in the Al/Si binary couple.

6.9.2 During the Cooling Process

From the SI M6.2, when the temperature was slowly reduced, the Si-rich interface was observed to move in the reversed direction toward the Al contact pad, consequently extending the Si-rich region. This phenomenon is similar to the previous diffusion behavior of the Si-rich interface during the heating process. Since the $Si_{0.67}Ge_{0.33}$ interface didn't show any change during extension of the Si-rich region, it is expected that Si atoms that previously moved out of the NW and into a grain boundary or surface of the Al reservoir are now coming back and reconstitute the NW cross-section. The Si-rich segment length extends as a linear function during the cooling and while kept at constant temperature, indicating that the rate limiting step in the reaction is an interface. From literature, this phenomenon can be explained by the solidification process of Al/Si binary system. The lowering of the temperature leads to a considerable drop of the Si solubility in the Al reservoir, resulting in the precipitation of Si atoms. The unreacted $Si_{0.67}Ge_{0.33}$ part can be a reasonable nucleation point for the precipitation due to the high Si content. During the elongation of the Si-rich region, we have observed the shrinkage of the NW diameter and the formation of structure defects. These phenomena occur due to the replacement of Ge atoms by Si atoms with smaller radius, making the crystal structure become more compact. Reduction of the NW diameter could also partly be explained by the fact that the NW volume does not necessarily have to be filled with Al or Si (and Ge) atoms exactly to the level it was prior to any reaction.

After the backward diffusion of the Si atoms, we observed the increase of HAADF signal intensity evidencing returning Ge atoms, also demonstrated by the formation of a Ge crystal on the Al pad when the retreating reaction interface reached the Al pad (shown by the EDX mapping in figure 6.5). Si signal at the Ge island appears very weak, which implies for an exhaustion of Si content in the Al contact reservoir. The backward diffusion of Ge atoms after the exhaustion of Si atoms is explained by the lower Al/Ge eutectic temperature (420 ^{o}C) compared to Al/Si (577 ^{o}C). The separation of the Si and Ge phase is a remarkably interesting phenomenon, which up to now, hasn't been reported in literature.

6.10 Mechanism of the Exchange Reaction in Small NW Diameters (≤ 100 nm)

Unlike the diffusion behavior in large NW diameters (≥ 150 nm) resulting in the formation of a high roughness $Si_{0.67}Ge_{0.33}$ interface, the created $Si_{0.67}Ge_{0.33}$ interface in small diameter NWs (≤ 100 nm) is typically clean with a convex shape. Figure 6.13 shows the HAADF-STEM images of a propagated $Si_{0.67}Ge_{0.33}$ NW lying over a hole on the Si_3N_4 membrane (**a**) and a zoomed image on the top part of the reaction interface (**b**). The investigated NW has a diameter of 83 nm. The specimen was annealed by RTA at 400 °C for 20 s, 400 to 300 °C for 30 s and cooled down to room temperature during 4 min to generate the thermal diffusion. Looking closer to the reaction interface shown in figure 6.13b, we can see a straight interface at the center and a bending shape when it comes to the interface edge. Typically, elucidating the interface shape in some propagated NWs, the reaction didn't seem to start from the surface, as observed in larger diameter $Si_{0.67}Ge_{0.33}$ NWs, but nucleated in the core of the NW and extended to the surface as shown in figure 6.14 (see also Fig. 6.6, 6.9 center images and 6.13). This can be the reason why the created interfaces are mostly abrupt and clean without any facet.

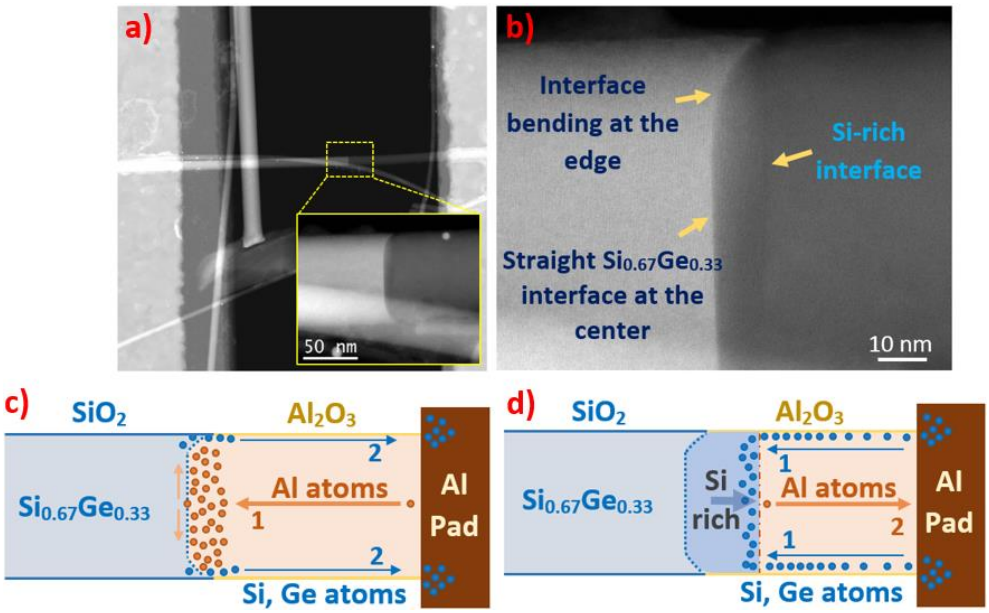

Figure 6.13: **a**) HAADF-STEM image of Al contacted $Si_{0.67}Ge_{0.33}$ NW (83 nm in diameter) after being annealed at 400 °C for 20 s, 400 to 300 °C for 30 s and cooled down to room temperature during 4 min. The inset figure shows the zoom on the reaction interface having a convex shape. (**b**) The magnified image on the top part of the reaction interface showing a straight interface at the center and a bending shape at the NW edge. **c-d**) Schematic illustrations of Al, Si and Ge diffusion direction during the forward propagation of the $Si_{0.67}Ge_{0.33}$ interface and backward diffusion of the Si-rich interface, respectively.

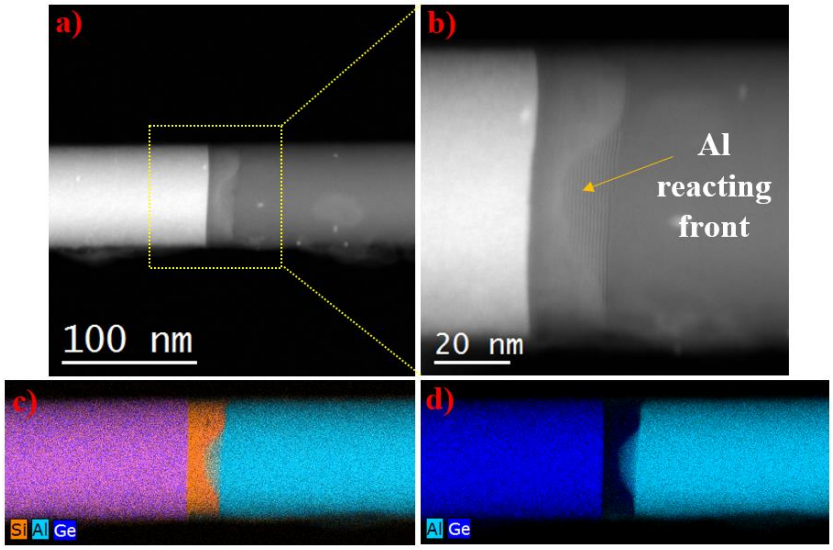

Figure 6.14: (**a-b**) HAADF STEM images of a propagated $Si_{0.67}Ge_{0.33}$ NW showing an Al reacting front at the center of the reaction interface. (**c**) EDX mapping of the reaction interface showing the presence of Si, Ge and Al in the reacted and unreacted NW part. (**d**) EDX mapping for Ge and Al elements, showing the leading front of Al in the center of the reacted part.

Figure 6.13c-d presents the schematic illustrations of Al, Si and Ge diffusion direction during the heating and cooling process. During the forward diffusion of the $Si_{0.67}Ge_{0.33}$ interface, Al atoms from the contact pad will move through the converted Al region to exchange with the Si and Ge atoms at the interface (**path 1**), starting from the center and spreading out toward the interface edge. From the results of the quantitative EDX analysis in section 6.5, in the unreacted $Si_{0.67}Ge_{0.33}$ part, Si and Ge surface atoms make bonds with oxygen atoms forming the stable SiO_2 shell (with a small fraction of GeO_2 shell since the Si/Ge ratio is ~0.67/0.33). Whereas the freshly created Al part is oxidized creating the Al_2O_3 shell. We speculate that the $SiO_2/Si_{0.67}Ge_{0.33}$ interface is more stable than the Al_2O_3/Al interface. Therefore, when approaching the NW surface, the exchange reaction is deaccelerated at the interface edge causing the formation of a convex interface. A similar argument has been reported in the paper of Chou et al [35], where they interpreted the formation of a convex interface between Si and Co. Turning back to figure 6.13c, after being replaced by Al atoms, Si and Ge atoms from the reaction interface pass through the surface diffusion channel toward the Al contact pad (**path 2**) where they diffuse on surfaces and grain boundaries of the large Al reservoir.

When the temperature is reduced, due to the solidification process, Si atoms from the Al reservoir now return and precipitate at the $Si_{0.67}Ge_{0.33}$ interface, pushing the Si-rich interface in the reversed direction (**path 1**). Al atoms at the reaction interface are replaced by Si and Ge atoms, forcing the Al atoms back to the Al contact pad (**path 2**). Previously, kinetic experiments in thin Ge NWs with Al contacts indicated that the reaction rate is limited by self-diffusion of Al (volume diffusion through the created segment), while Ge can diffuse back to the reservoir by surface diffusion (El Hajraoui et al [13]). The concave interface shape we observe in thin $Si_{0.67}Ge_{0.33}$ NWs appears well in agreement with this hypothesis.

6.11 Mechanism of the Exchange Reaction in Passivated NWs

As presented in section 6.8, when as-grown NWs are passivated by a 20 nm Al_2O_3 shell, the reaction interface becomes very abrupt without any facet. This phenomenon was attributed to the absence of surface defects due to the HI etching process and surface protection by the Al_2O_3 shell. Figure 6.15 shows the reaction interfaces on the two propagated NWs with different diameters (30 and 108 nm) after being annealed by RTA at 450 ^oC for 20 s, 450 to 300 ^oC in 20 s and cooled down to room temperature during 4 min. Firstly, we can see that the $Si_{0.67}Ge_{0.33}$ interfaces on the small **NW1** and the large **NW2** are very sharp. It is clear that with the presence of the passivation shell, the NW size has no more influence on the formation of the interface shape compared to the unpassivated NWs. This phenomenon is attributed to the improvement of NW surface quality by removing the native surface oxidation layer. We still observe the presence of the double interface region; however, the Si-rich segments in the two NWs are extremely thin. This ex-situ heating result is coherent with the in-situ observation presented in figure 6.12 (also see the supporting information SI M6.4**)**. Potentially, the interfacial energy difference between two sides of the reaction interface has been reduced by the presence of a pre-deposited Al_2O_3 shell. Therefore, the reaction rate is equal on the lateral direction resulting in the formation of a sharp $Si_{0.67}Ge_{0.33}$ interface.

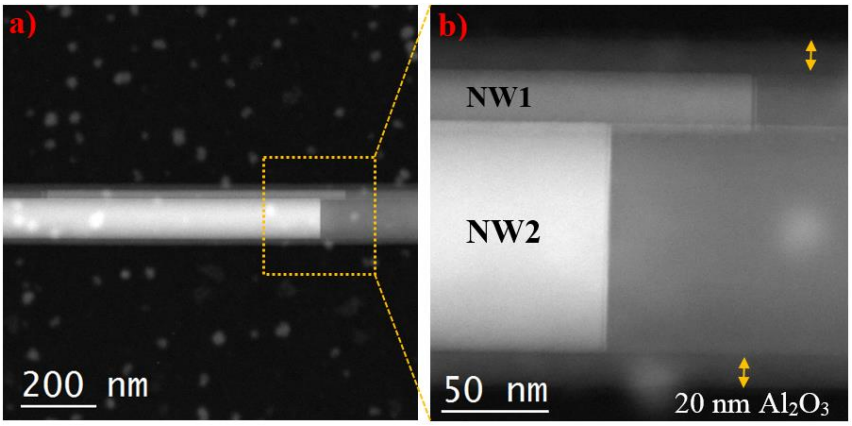

Figure 6.15: (**a**) HAADF STEM image of two propagated NWs with different diameters (30 and 108 nm) and (**b**) a zoom on the reaction interfaces showing the presence of sharp $Si_{0.67}Ge_{0.33}$ interfaces.

6.12 The Electrical Transport Characteristics of Al/Si/$Si_{0.67}Ge_{0.33}$ Heterostructures

For device applications, it is of crucial importance to investigate the electrical transport property of the created Al/Si/$Si_{0.67}Ge_{0.33}$ heterostructures. We have therefore performed electrical measurements on the $Si_{0.67}Ge_{0.33}$ NWs before and after the thermal diffusion. Before the metal deposition process, the as-grown NWs were cleaned by HI acid and Ar plasma cleaning to remove the oxide layer for a good contact. Figure 6.16a shows the BF STEM image of a contacted NW after the thermal reaction via RTA at 430 ºC for 20 s, 430 to 300 ºC for 30 s and cooled down to room temperature during 4 min. The exchange reaction has taken place from two sides of the contacted NW (190 nm in diameter), leaving a remaining unreacted $Si_{0.67}Ge_{0.33}$ segment of about 1.75 µm. The plot in figure 6.16b shows the IV characteristics of the contacted NW before and after the thermal propagation. Firstly, we can see that the current passing through the un-doped $Si_{0.67}Ge_{0.33}$ NW is very low, in the order of 10^{-10} A for a biasing voltage of 1 V. After the metal intrusion, the contact resistance had increased significantly so that the measured current dropped two orders of magnitude. Potentially with the presence of the Si-rich region between the reacted and unreacted part, which has a large bandgap energy, the flowing current is blocked by the band offset at the Si/$Si_{0.67}Ge_{0.33}$ interface, causing the drop of the measured current. In another experiment, we have tried to measure the photocurrent through an Al/Si/$Si_{0.67}Ge_{0.33}$/Si/Al heterostructures. However, the contact resistance is so high that the induced photocurrent is below the detection limit of the detection setup. Therefore, with respect to applications, it is necessary to dope the NWs before further electrical investigation.

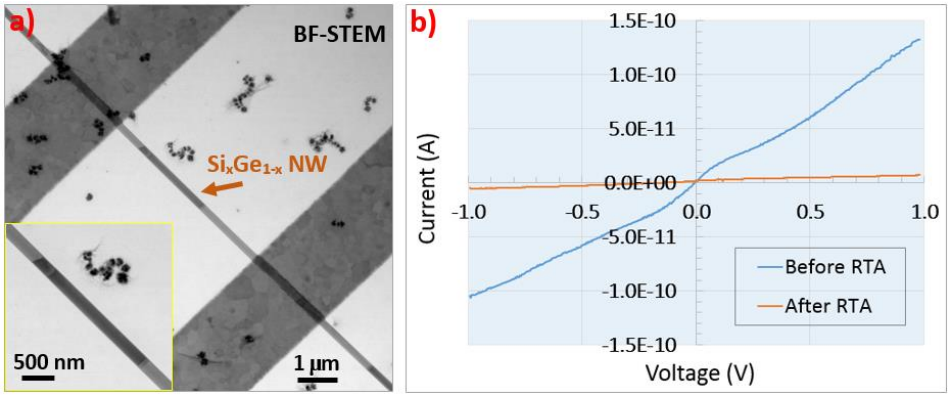

Figure 6.16: a) BF-STEM image of the Al contacted $Si_{0.67}Ge_{0.33}$ NW after the thermal reaction via RTA at 430 °C for 20 s, 430 to 300 °C for 30 s and cooled down to room temperature during 4 min. The insert figure shows a zoom on the contacted NW with the presence of the unreacted $Si_{0.67}Ge_{0.33}$ segment of about 1.75 µm. **b**) The plot shows the IV characteristics measured on the contacted NW before and after the thermal propagation.

6.13 Conclusion

Al- (Si, Ge) NW thermal exchange reaction was fully investigated via ex-situ and in-situ heating techniques. The incorporation of Al metal in $Si_{0.67}Ge_{0.33}$ NWs results in the formation of Al/Si-rich/$Si_{0.67}Ge_{0.33}$ heterostructures. Scanning transmission electron microscopy (STEM), Geometric phase analysis (GPA) and Qualitative Energy-dispersive X-ray spectroscopy (EDX) combined with 3D reconstruction were performed on the reacted and unreacted NW segments, providing a complete understanding of the structure and composition of the created heterostructures. Moreover, we show clear evidence for the influence of the NW diameter, surface passivation and annealing conditions on the diffusion behavior of the reaction interface. Based on these observations, we have proposed some hypotheses to interpret the kinetics of the thermal diffusion. Finally, we present electrical measurements on the Al/Si/$Si_{0.67}Ge_{0.33}$ heterostructures, which demonstrate a significant increase of the contact resistance after the metal incorporation in un-passivated large diameter NWs. While the NW diameter and surface quality may also affect this result, an increased doping of the NW appears necessary to increase the NW conductivity for device applications.

Chapter 7 :

Conclusions and Perspectives

7.1 Conclusions

7.1.1 On the thermally activated solid-state reaction in the Al/Ge binary system

In this study, the diffusion behavior of the Al-Ge thermal exchange reaction was fully described from the earliest stage to the end of the exchange process using real-time observations, providing a method to deterministically create a semiconductor region with near atomic scale precision. Firstly, we present in-situ direct joule heating experiments showing how the heating electrode could be damaged due to the formation of Al crystals and voids in the vicinity of the metal/NW contact, likely related with electro-migration phenomena. We show that the contact quality can be preserved by including an additional ex-situ RTA step prior to the in-situ heating. The in-situ observations also show in real-time how the exchange reaction initiates simultaneously from several locations underneath the Al contact pad, and the Al crystal grows gradually inside the initial Ge NW with the growth interface along a Ge (111) lattice plane. Once the reaction front moves out from underneath the contact metal, two factors jeopardize an atomically accurate control of the Al/Ge reaction interface. We observed that at magnifications where lattice planes are visible, the electron beam influences the propagation locally at such a high magnification. It is therefore better to work at a slightly lower magnification, with the additional benefit of having the entire reaction interface within the field of view. Importantly, we have demonstrated the influence of the NW surface quality on the diffusion behavior of Al in a Ge NW. Without the presence of a protecting layer, the Al protruding length shows stepwise growth dependence as a function of time while a much smoother linear time dependence is observed when the NW is covered by a 5 nm Al_2O_3 shell in these relatively large diameter NWs ($120 \leq d \leq 162$). Carefully controlling all aspects of the exchange reaction, we demonstrate a fabrication process combining ex-situ and in-situ heating techniques to precisely control and produce axial Al/Ge/Al NW heterostructures with an ultra-short Ge segment down to 7 nanometers. From literature, this is the smallest Ge segment length that has been obtained in the Al/Ge binary system, and among the smallest segments in other semiconductor NW metal systems. These nm-scale observations are extremely useful to understand

the reaction behavior of metals with respect to Ge NWs or other semiconductors and observe potential differences with respect to bulk materials

Then, we elucidate the transport property of the fabricated short Ge segments in the range of 200 to 550 nm segment lengths (with 50 nm NW diameter), which show a maximum current of about 100 μA, corresponding to current densities of 5 x 10^{10} A.m^2 and the ability to withstand a high current (80 μA) for more than one hour. Moreover, the contact quality of the fabricated Al/Ge junctions has been investigated via the calculation of the contact resistance before and after the metal incorporation into the Ge NW, demonstrating an important improvement in quality and reliability after the exchange reaction.

Finally, we verify the dopant "pile up" hypothesis, which expects an enrichment of dopant concentration in the vicinity of the reaction interface between the Al reacted region and unreacted Ge NW. The hypothesis was proposed due to the formation of a monocrystalline Al core when Al exchanges and incorporation into a Ge NW. However, from quantitative SEM - EDX analyses, it was observed that there wasn't a considerable redistribution of the dopant within the propagated structure.

7.1.2 On the thermally activated solid-state reaction in the Al- (Si, Ge) ternary system

In this study, the thermal diffusion of Al- (Si, Ge) ternary system has been described in detail. The investigated solid state reaction initiates from 350 °C where the Al metal starts to enter the $Si_{0.67}Ge_{0.33}$ NW through the NW surface underneath the Al contact pad. While slowly raising the heating temperature, the Al reaction front advances progressively in the initial $Si_{0.67}Ge_{0.33}$ NW and a Si rich segment (>=90%) is formed, sandwiched between the reacted and unreacted part of the NW. As the reaction proceeds, the two interfaces advance in the NW with sub- 50 nm sized steps, and the first interface (between the created Al and the Si rich region, called "**Si-rich interface**") can move back and forth, while the interface between the Si rich region and the initial NW (the "**$Si_{0.67}Ge_{0.33}$ interface**") only advances. The metal protruding in as-grown NWs with large diameters (≥ 150 nm) results in the formation of a rough $Si_{0.67}Ge_{0.33}$ interface with several facets while a convex - clean interface is formed on NWs with small diameters (≤ 100 nm). When the reaction temperature is slowly lowered, a linear extension of the Si-rich segment length in the reverse direction towards the Al reservoir has been observed without modification of the interface

with the initial $Si_{0.67}Ge_{0.33}$ alloy NW. During this reverse reaction the freshly created Al NW part is again consumed by the growing Si rich segment, where progressively also more Ge is incorporated.

From the in-situ and ex-situ observations, we propose some hypotheses to interpret the kinetics of the thermal exchange reactions in small ($\leq$ 100 nm) and large ($\geq$ 150 nm) NW diameters:

❖ *During the heating process*:

- In large NW diameters, the step-wise propagation of the $Si_{0.67}Ge_{0.33}$ interface is explained by the presence of defect states on the NW surface. The non-uniform reaction in the radial direction leads to the formation of several facets at the $Si_{0.67}Ge_{0.33}$ interface. The backward diffusion of the Si–rich interface during the heating process is attributed to the saturation of the Si content in the Al diffusion channel (constituted of the surfaces and grain boundaries of the Al metal contact and created NW region), causing the precipitation of Si at the $Si_{0.67}Ge_{0.33}$ interface.
- In small NW diameters, the exchange reaction nucleates from the center of the reaction interface and spreads out to the interface edge with a slower diffusion rate, resulting in a clean, often convex interface shape. We speculate that may be attributed to the energy difference between the $SiO_2/Si_{0.67}Ge_{0.33}$ interface and Al_2O_3/Al interface. Meanwhile, Si and Ge atoms from the reaction interface pass through the surface diffusion channel toward the Al contact pad where they diffuse on surfaces and grain boundaries of the large Al reservoir.
- For both small and large diameter NWs, with the presence of a passivated Al_2O_3 shell, the reaction interface becomes very sharp without any facet. Indeed, the NWs with this treatment demonstrate a very sharp and smooth propagation of the second interface, and the Si rich region becomes shorter or even vanishes. This phenomenon is attributed to the improvement of NW surface quality by removing the native surface oxidation layer and passivating the NW surface by a 20 nm thick Al_2O_3 shell. Moreover, the presence of the passivated Al_2O_3 shell helps to balance the interfacial energy (between the NW core and passivation shell) on the two sides of the reaction interface, which consequently results in the creation of a sharp $Si_{0.67}Ge_{0.33}$ interface.

❖ *During the cooling process:*

- There is a reversible propagation of diffusive species where Si atoms, and later followed by Ge atoms, return to the NW cross-section while Al atoms diffuse back to the reservoir. This interesting diffusion phenomenon is explained by the solidification process of the Al- (Si, Ge) ternary system

when the heating temperature falls down below the eutectic temperature of the (Al-Si) and (Al-Ge) couples.

Finally, we present electrical measurements on the Al/Si/$Si_{0.67}Ge_{0.33}$ heterostructures, which demonstrate a significant increase of the contact resistance after the metal incorporation in un-passivated large diameter NWs.

7.2 Perspectives

7.2.1 For Al/Ge NW binary

The thermal reaction of Al metal/Ge as-grown NWs has shown a step-wise diffusion behavior which has been attributed to the presence of surface defects on the NW, probably present at the Ge/GeO_2 interface. However, practically investigating these defects using TEM imaging is difficult as TEM is not a very suitable technique to analyze point defects. For further analysis, electron-beam-induced current (EBIC) technique can be applied to analyze these surface defects. By evaluating the current passing though the as grown and passivated NWs under the radiation of the scanning electron beam, the quality of the NW surface may be further elucidated.

From the ex-situ and in-situ studies of the thermal reaction, we have established a reliable process to control the diffusion process with atomic scale precision. It has been pointed out that the electron beam radiation at high acceleration voltage (200 kV) can locally accelerate the diffusion speed when focusing on the reaction interface with a high magnification. Moreover, using large diameter Ge NWs ($\geq$100 nm) and preparing the specimens on a thick Si_3N_4 membrane (200 nm) can be a bottleneck for obtaining high resolution images. It is therefore necessary to conduct the in-situ TEM experiments at low acceleration voltage (e.g., 80 kV) with TEM mode to reduce the beam dose, and moreover working with smaller NW diameters ($\leq$50 nm).

7.2.2 For Al- (Si, Ge) NW Ternary

Similar to Al/Ge couple, the exchange reaction on the $Al/Si_{0.67}Ge_{0.33}$ interface is not homogeneous in the radial direction causing the formation of facets on the reaction interface. It is noted that the surface quality strongly influences the diffusion behavior of the reaction interface. Therefore, the surface quality of the as-grown NWs should be further investigated to have a better understanding of the diffusion behavior and kinetics.

From EDX quantification, we have found about 4% of Si content in the Al converted NW region and 2% of Al in the Si-rich region. In literature, the maximum solubility limit of Si in Al is about 2% and that of Al in Si is negligible, about 1.15×10^{-2} at. % at 997 ^{o}C. Therefore, these results can be an artifact caused by the scattered signals of Si and Al from the Si_3N_4 membrane and Al contact pads. Besides, there is a possibility that Al atoms diffuse into the structure defects present in the Si-rich segment. To improve the precision, specimens should be prepared on a Si-free substrate. FIB lamella preparation can be applied to make NW cross-section specimens on the reacted part of the NW and attach these to a Cu TEM grid.

The final goal of this study is to fabricate $Si/Si_xGe_{1-x}/Si$ heterostructures for near infra-red photo-detection. We have tested a propagated NW with an exciting laser for measuring the induced photocurrent. However, due to a significant increase of the contact resistance, the measured photocurrent falls below the noise limit. Therefore, to improve the conductivity, it can be interesting to investigate the photocurrent on propagated p-i-n junction Si_xGe_{1-x} NWs.

7.2.3 Thermal Exchange Reaction in Core-Shell NW Systems

As presented in the chapter 5, the diffusion process of Al metal in Ge NWs can be controlled with atomic precision, giving a possibility to fabricate sub- 10 nm Ge segments. Meanwhile, there is no report of Al metal diffusion in pure Si NWs. Therefore, it can be interesting to perform the intrusion of Al in Ge-Si or Si-Ge core-shell NWs, expecting the formation of axial and radial metal−semiconductor nanowire heterostructures. Since the surface quality is what mainly influences how well the reaction ‘behaves’, the shell is important, and additionally can be a way to add more properties to the structure. In the frame of this PhD work, we have also demonstrated that propagation can occur in Ge-Si core shell NWs (see ref [137]). In such NWs transport occurs by a hole gas at the Ge-Si interface [138]. Moreover, propagation in structures with a Ge shell may also be very interesting, since it may be a way to obtain a very high quality abrupt interface between a

semiconducting core and a super conducting material, which is of particular interest in the study of Majorana Fermions [139,140].

The results of the thermal incorporation of Al in Ge-Si and Si-Ge core shell NWs are presented in the Appendix A. For the Si-Ge core-shell NW system, however, these experiments were not conclusive either because the shell was not continuous but rather broken up in islands, or because the final NWs were alloyed rather than well-defined core-shell NWs. This may be a promising topic if better control of thin shell growth can be obtained.

APPENDIX A

Fabrication of Radial Metal−Semiconductor Nanowire Heterostructures

A1. Al Thermal Diffusion in Ge - Si Core - Shell NWs

A1.1. Experimental

For this experiment, the sample fabrication process was performed by Dr. Masiar Sistani, TU-Wien, Austria. Particularly, the Ge/Si core shell NWs were grown by VLS method, producing a Ge NW core diameter of about 50 nm and a Si shell thickness of about 3 nm (covered by a thin native SiO_2 shell). The NWs were grown in the group of Charles Lieber [138]. Prior to the NW contacting process via electron beam lithography, the Si shell of as-grown NWs was selectively removed by wet chemical etching for 10 s in buffered HF (7:1) to remove the SiO_2 layer and then 15 s in KOH (30%) to remove the 3 nm Si shell. The NWs were then dispersed on the 200 nm thick Si_3N_4 membranes with holes in the shape of slits and contacted by 100 nm Al pads via the sputtering technique. To conduct the thermal exchange reaction, specimens were consecutively annealed at 674 K in forming gas and checked by SEM imaging to follow the diffusion length of Al. The described characterization was conducted on suspended NWs lying over a hole in the Si_3N_4 membrane. These results were published in [137].

A1.2. Structural and Compositional Analysis

Figure A.1a-b shows the HAADF-STEM images of an Al contacted Ge-Si core-shell NW after the ex-situ heating (RTA). The propagated NW has a diameter of about 71 nm and 7.2 μm in length. Since the diameter of the reacted and unreacted parts of the propagated NW didn't change noticeably, the dark and bight contrast parts in figure A.1a demonstrate the positions of the Al reacted and Ge unreacted part. Firstly, on the Al reacted part, we can observe the presence of several bight features. These features can be the Ge remaining after the exchange reaction. The zoomed image in figure A.1b shows the formation of a sharp Al/Ge interface. Besides, we can see the presence of a Ge remaining shell closed to the Al/Ge interface.

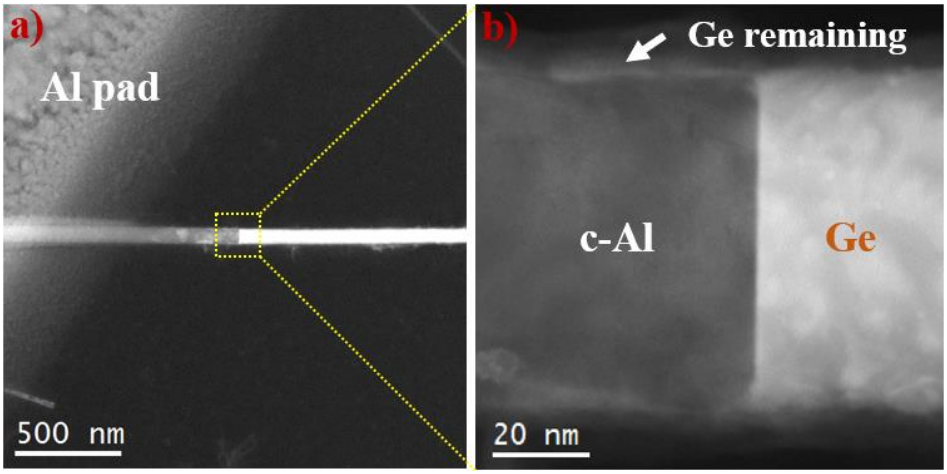

Figure A.1: (**a**) HAADF-STEM image of an Al contacted Ge-Si core-shell NW after the consecutive heating at 674 K in forming gas. The NW diameter is about 71 nm with 7.1 μm length. (**b**) a zoom on the reaction interface showing the presence of a sharp Al/Ge interface and a remaining part on the NW shell that may be attributed to remaining Ge.

To study the structure property of the reaction interface, HR-HAADF-STEM images were taken at the Al-Ge interface, shown in figure A.2a-c. The NW was oriented along the [11-2] direction of the Ge unreacted part. The inset of figure A.2c shows the corresponding Fourier transformation (FT) of the HR image with indexed reflections in the Ge crystal, indicating the (111) reflection both in the Ge and c-Al part. Both the image and the FT show the (111) growth plane in the Ge diamond cubic structure with a lattice spacing of 0.33 nm, in good agreement with tabulated values [141]. In addition, the extra peak indicated by the left arrow on the inset FT shows the presence of a family of planes with smaller lattice spacing of around 0.23 nm, which is in good agreement with the theoretical interplanar spacing of Al face centered cubic (fcc) for {111} planes [142]. The Al (111) plane is observed to be parallel to the Ge (111) growth plane, while the perpendicular reflection (2-20) is only visible in the Ge crystal, indicating that the Al crystal is not viewed along the same direction. Indeed, the Al crystal is rotated by ~6° around the NW axis with respect to the Ge crystal in this NW heterostructure. The interface appears to be very abrupt regardless of the large lattice mismatch between Al (a = 0.404 nm) and Ge (a = 0.565 nm) and no crystal defects are observed at the interface. In figure A.2c the reaction interface is shown along the [10-1] direction of observation, as confirmed by the FFT indexed for the Ge crystal shown in the inset. At the NW surface on the Al part, we see first a bright layer, surrounded by a darker layer, both of which share the lattice of the Ge part (atomic planes are visible). These layers are attributed respectively to a thin crystalline layer containing Ge as indicated by the arrow, surrounded by the Si shell outlined

by dash-dotted lines. An amorphous layer is also observed around the crystalline Si shell, most likely consisting of SiO_2.

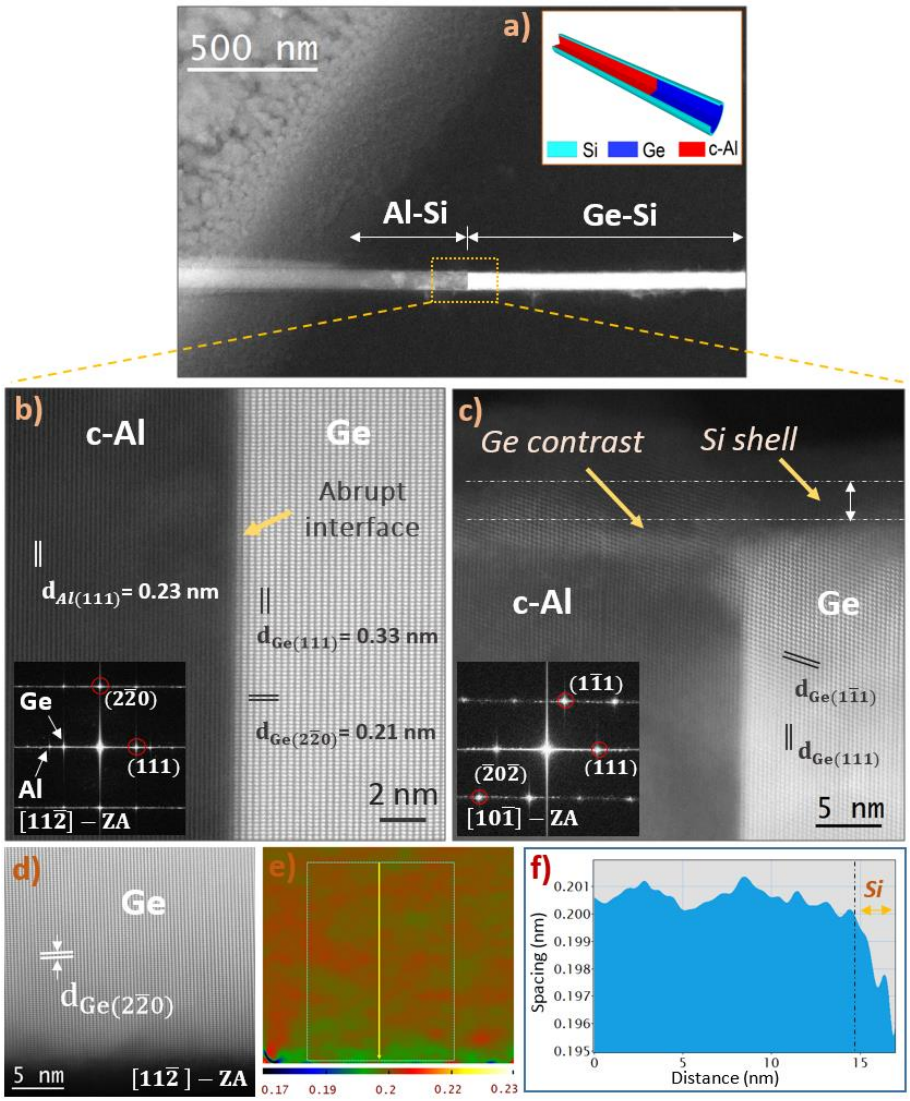

Figure A.2: (**a**) HAADF STEM image of investigated NW with inserted schematic illustration of the Al−Ge heterostructure with a Si shell. (**b**) HR HAADF STEM at the Al−Ge interface with the corresponding Fourier transformation (FFT) in the inset showing (111) planes in both Al and Ge parts with spacings of 0.23 and 0.33 nm, respectively. (**c**) Zoom-in at the Al−Ge interface along another direction of observation with the corresponding FFT in the inset indexed in the Ge part. The HAADF STEM contrast at the sidewall reveals the presence of an epitaxial shell wrapped around both the Ge as well as the c-Al core. (**d−f**) Geometrical phase analysis (GPA) along (2−20) planes in the unreacted Ge region shows a decrease in lattice spacing at the sidewall, which is coherent with the smaller lattice spacing in Si.

Moreover, the geometrical phase analysis (GPA) on the Ge (2-20) reflection of the unreacted part of the NW oriented on the [11-2] direction, figure A.2d-f, shows a decrease in lattice spacing at the sidewall, which is coherent with the smaller lattice spacing of Si (d_{220} = 0.192 nm). Clearly, the HRSTEM characterization confirms the presence of a uniform crystalline Si shell wrapped around the c-Al core NW.

To investigate the accurate composition of the NW heterostructure, energy dispersive X-ray spectroscopy (EDX) maps were acquired in STEM mode on the same sample, after the propagation of the c-Al phase inside the Ge-Si core-shell NW. Quantitative concentration profiles were extracted from the elemental maps allowing the reconstruction of the chemical nanostructure of both the unreacted and reacted parts of the NW.

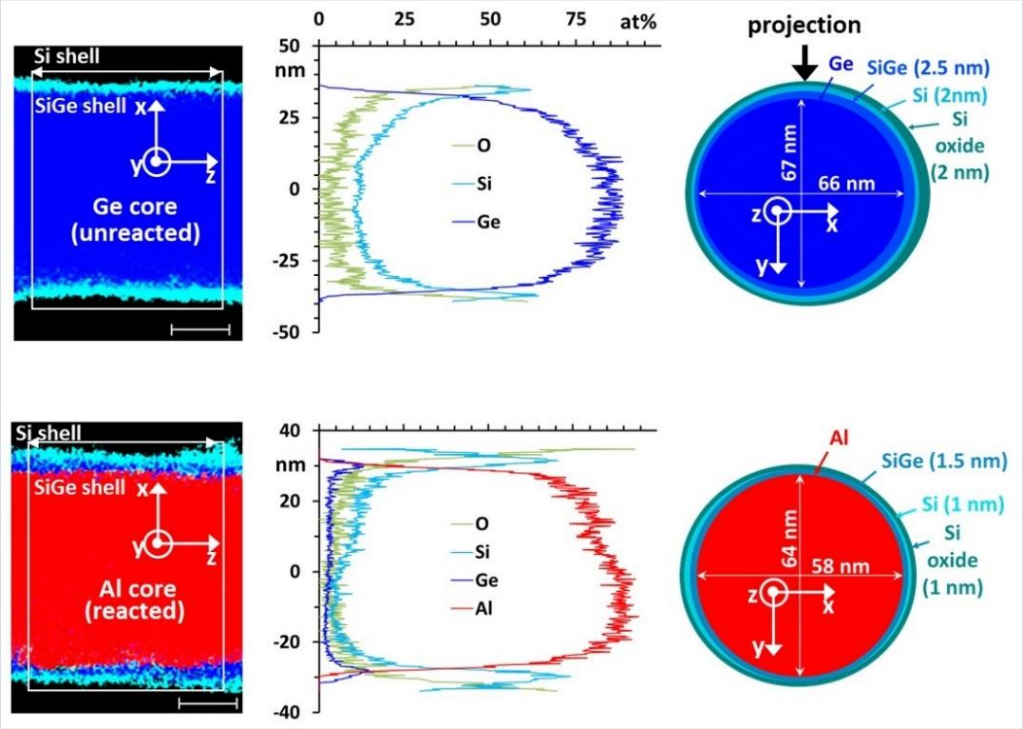

Figure A.3: Distribution of O, Al, Si and Ge measured by STEM/EDX in the reacted and unreacted Ge-Si core-shell NW heterostructure with partially substituted Ge core by c-Al. For each region we show from left to right the chemical map, the chemical profile in at. % obtained at the indicated location, as well as a model of the NW constructed by comparing the experimental quantified X-ray signal with a model, respectively. The vertical arrow indicates the projection direction of the model. The scale bars are 20 nm.

The chemical reconstruction of the unreacted segment i.e. Ge-Si core-shell NW shows the presence of a 4 nm thick shell wrapped around the Ge core. The outer part of the shell is partly oxidized over 2 nm. A sharp SiGe interface of less than 2.5 nm is observed between the Si shell and the Ge core. The chemical reconstruction of the reacted segment also shows the presence of a Si shell, twice as thin as the previous one, whose outer part is also oxidized over 1 nm. It also reveals the presence of a 1.5 nm thick SiGe shell sandwiched between the Al core and the Si shell. One should also mention that prolonged thermal Ge-Al exchange leads finally to a complete exchange of the Ge by Al and thus to a uniform radial metal-semiconductor NW heterostructure. The diameter of the Al core NW and the thickness of the wrapped around semiconducting shell are inherited from the initial Ge-Si core-shell NW.

A2. Al Thermal Diffusion in Si – Ge Core - Shell NWs

A2.1. Experimental

For these experiments, we had used two different sets of Si-Ge core shell NWs due to the failure of the NW shell quality (discontinuous Ge shell in the first sample, sample 1). Firstly, the specimens (from sample 1) shown in figure A.4 and A.5 were prepared by Dr. Masiar Sistani, TU-Wien, Austria. Particularly, the as-grown Si-Ge core shell NWs had a Si core of about 50 nm and maximum Ge shell of 8 nm. The NWs were dispersed on the Si_3N_4 membranes and contacted with sputtered Al pads (100 nm thick). The specimens were then annealed at 674 K in forming gas to initiate the exchange reaction.

Because we found that the Ge shell was discontinuous in sample 1, a second sample was grown and send to us. The growth process of these two NW samples was explained in the ref [143]. The specimens presented in figure A.6 and A.7 were prepared with NWs from sample 2. The NWs were contacted by 200 nm Al pads (deposited by electron beam evaporation) on the Si_3N_4 membranes. Prior to the metal deposition, the specimens were cleaned by HI acid (5 s) and plasma (15 s) to remove the native oxide. To perform the exchange reaction, specimens were annealed by RTA in N_2 gas at 300 ^oC for 20 s and cooled down to room temperature in 4 min.

A2.2. Structural and Compositional Analysis

Figure A.4a-b shows HAADF STEM images of an as-grown Si-Ge core shell NW without the Al contacts from sample 1. As indicated by the yellow arrows, the NW shell was not continuous, but had a strong variation in the shell thickness. A zoomed image of the NW shell (taken in the orange box) is presented in figure A.4b, showing the presence of a crystalline shell with the maximum shell thickness of about 8 nm. EDX mapping of present elements is shown in figure A.4c, demonstrating the presence of a Si core and discontinuous Ge shell.

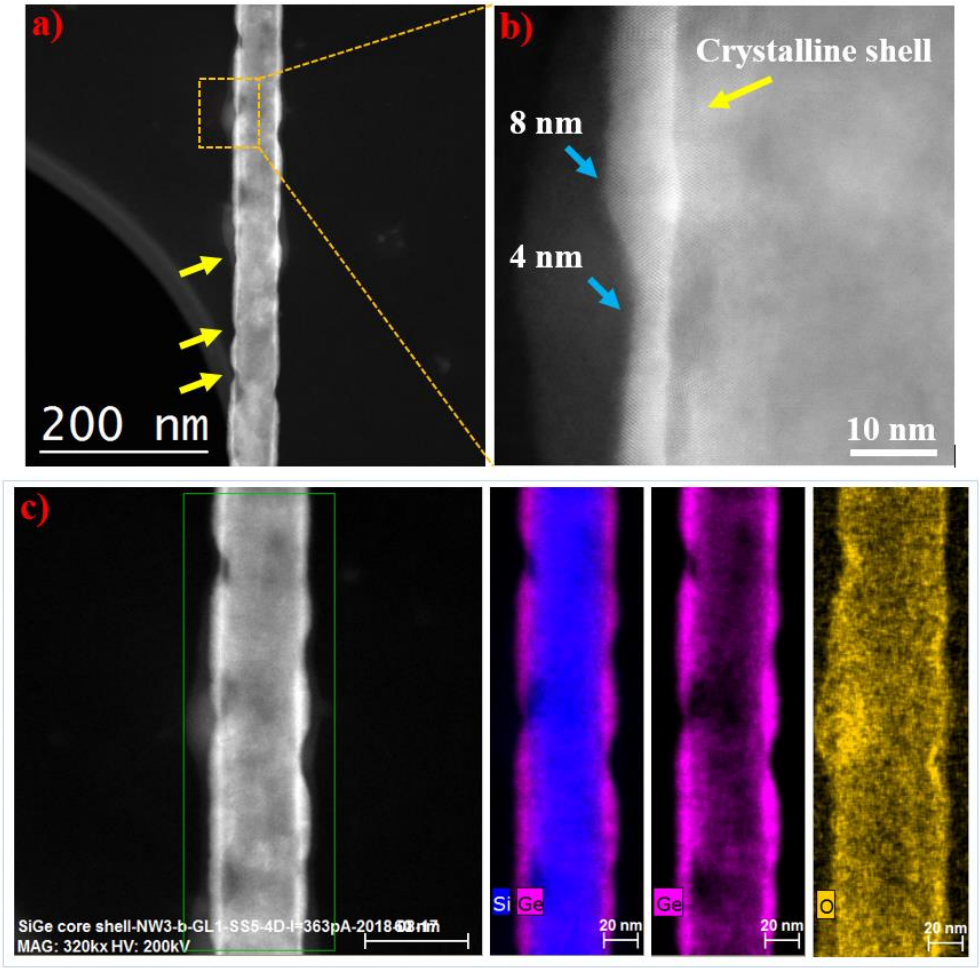

Figure A.4: (**a-b**) HAADF STEM images of an as-grown Si-Ge core shell NW of sample 1 before being treated by RTA. The yellow arrows indicate the missing shell at different positions. The zoomed image of the NW shell (taken in the orange box) shows the presence of a crystalline shell with the maximum shell thickness of about 8 nm. (**c**) EDX mapping for present elements, demonstrating the presence of a Si core and discontinuous Ge shell.

Figure A.5 shows the results of EDX mapping on a propagated Si-Ge core shell NW. Indicated by the white arrow, the exchange reaction had taken place from the bottom of the NW having a reaction length of about 700 nm. The chemical maps presented on the right side show the non-homogeneous distribution of both Ge and Al within the unreacted and reacted part, respectively. The reaction interface was not obvious from the EDX maps. However, it was clear that the Si core didn't react with Al at the annealing temperature.

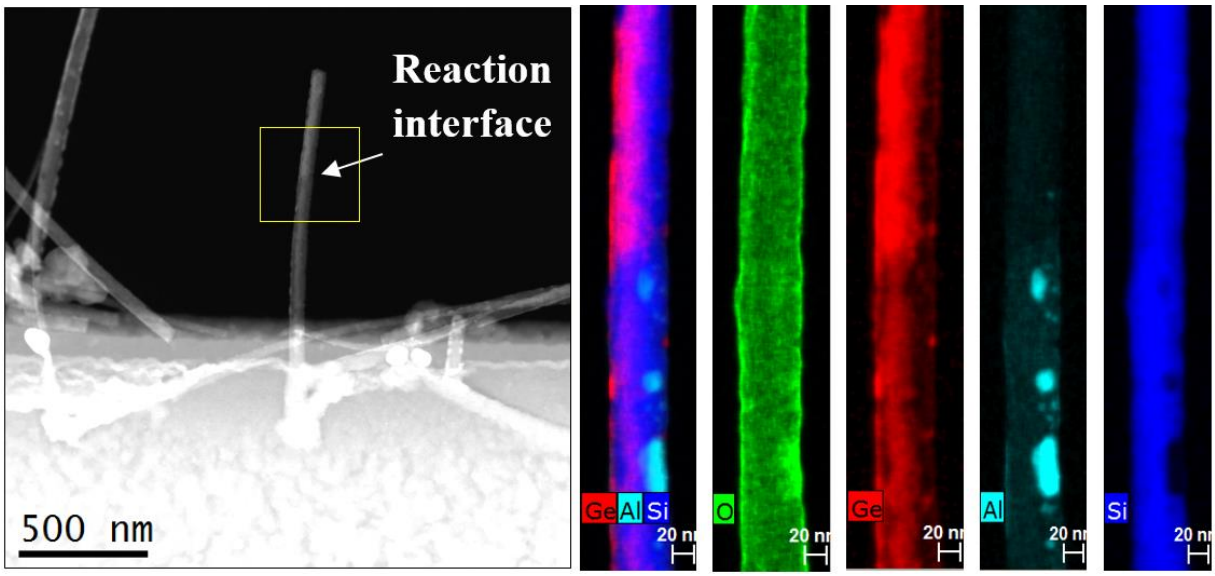

Figure A.5: EDX mapping for present elements on a propagated Si-Ge core shell NW of sample 1. The NW diameter is about 61 nm with a length of 1.5 μm. The reaction interface was not clear on either the HAADF STEM image or EDX maps. The chemical maps show the non-homogeneous distribution of both Ge and Al within the unreacted and reacted part, and unreacted Si core.

Since the Ge shell of the NWs from sample 1 was not continuous, we obtained a second Si-Ge core shell NW sample (sample 2) expecting a better Ge shell quality. Figure A.6a shows a HAADF STEM image of a Si-Ge core shell NW of sample 2 before the thermal annealing. This time, the shell thickness was quite uniform and about 35 nm. However, from the HAADF image and EDX maps shown in figure A.6a-c, we can see the mixing of Si and Ge in both the core and the shell, becoming an alloy NW.

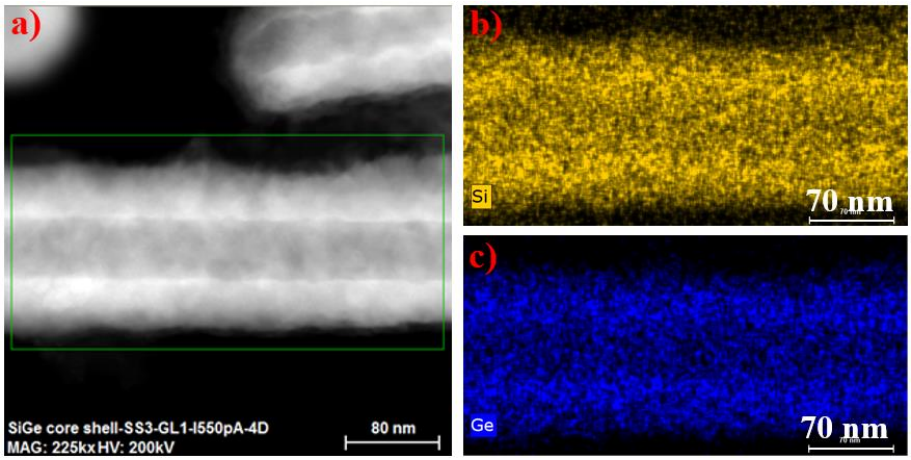

Figure A.6: (**a**) HAADF STEM image of a Si-Ge core shell NW before the thermal treatment of sample 2. The shell thickness is quite uniform with about 35 nm. (**b-c**) EDX mapping of the distribution of Si and Ge, showing the intermixing of both Si and Ge in the core and shell of the NW.

The results of the thermal exchange reaction of Al in NWs from sample 2 are presented in figure A.7. Based on the HAADF contrast, we can observe that the exchange reaction had taken place in both the core and the shell of the NWs. The diffusion behavior is probably similar to the case of Si_xGe_{1-x} alloy NWs presented in chapter 6. As shown in the images, the reaction front is not sharp, and there are remaining Ge islands on the shell. The growth of the Si-Ge core shell NWs should be improved before performing further investigation.

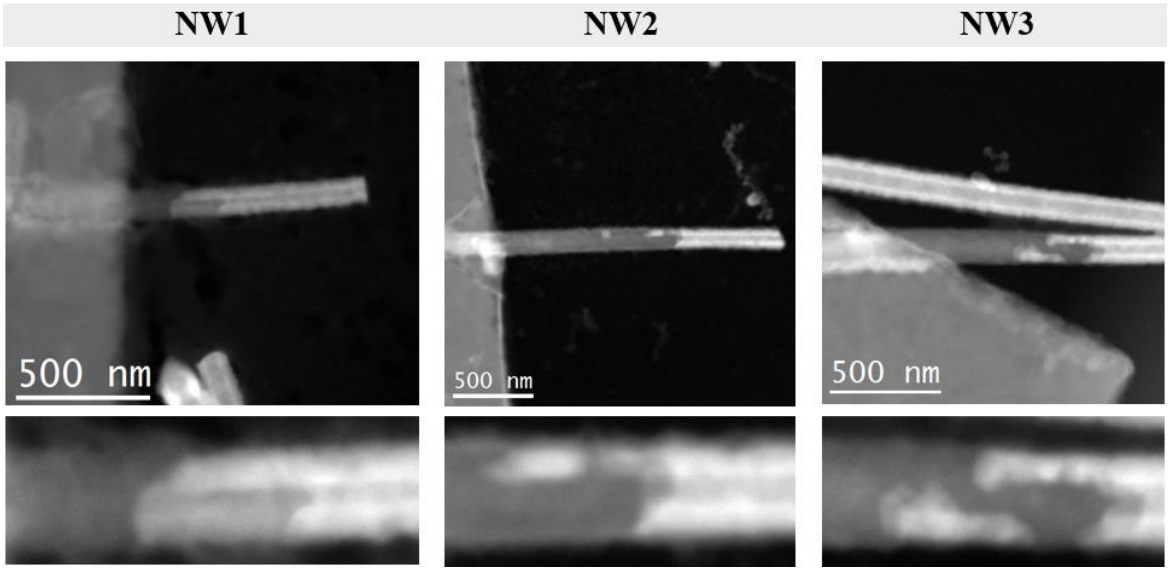

Figure A.7: HAADF STEM images of three different propagated Si-Ge core shell NWs of sample 2.

Supporting Information

1. **SI M5.1**:
   https://pubs.acs.org/doi/suppl/10.1021/acsanm.9b02564/suppl_file/an9b02564_si_002.mp4

2. **SI M5.2**:
   https://pubs.acs.org/doi/suppl/10.1021/acsanm.9b02564/suppl_file/an9b02564_si_003.mp4

3. **SI M5.3**:
   https://pubs.acs.org/doi/suppl/10.1021/acsanm.9b02564/suppl_file/an9b02564_si_004.mp4

4. **SI M5.4**:
   https://pubs.acs.org/doi/suppl/10.1021/acsanm.9b02564/suppl_file/an9b02564_si_005.mp4

5. **SI M5.5**:
   https://drive.google.com/open?id=1Lzry1FleIu_Uc9kcFON68JRHtcDRU0G7

6. **SI M5.6**:
   https://pubs.acs.org/doi/suppl/10.1021/acsanm.9b02564/suppl_file/an9b02564_si_006.mp4

7. **SI M5.7**:
   https://drive.google.com/open?id=1Uo_VFo8ZIF6gWy558P4jgd3lW0d2V2q6

8. **SI M5.8**:
   https://pubs.acs.org/doi/suppl/10.1021/acsanm.9b02564/suppl_file/an9b02564_si_007.mp4

9. **SI M6.1**:
   https://drive.google.com/open?id=1zqE5ToYMKW-ivFT-7oi5EvIpG_JNBsx0

10. **SI M6.2**:
    https://drive.google.com/open?id=1WcbnkpiCX11j3X20fEEXv4IqtWNFUkHu

11. **SI M6.3**:
    https://drive.google.com/open?id=1Y1vHyGjQ9CAypJyFfzovtz9Y8_FbAkZE

12. **SI M6.4**:
    https://drive.google.com/open?id=1LLVrRFqhspgdHkaB0CwCSYsO6inMaJcd

REFERENCES

[1] Field Effect Semiconductor Device Concepts Patented | The Silicon Engine | Computer History Museum. https://www.computerhistory.org/siliconengine/field-effect-semiconductor-device-concepts-patented/

[2] M.M. Irvine, Early digital computers at Bell Telephone Laboratories, IEEE Ann. Hist. Comput. 23 (2001) 22–42. doi:10.1109/85.948904.

[3] G.E. Moore, Cramming more components onto integrated circuits, Reprinted from Electronics, volume 38, number 8, April 19, 1965, pp.114 ff., IEEE Solid-State Circuits Soc. Newsl. 11 (2006) 33–35. doi:10.1109/N-SSC.2006.4785860.

[4] Samsung Says New 7-Nanometer Chip Production Starting This Year, Bloomberg.Com. (2018). https://www.bloomberg.com/news/articles/2018-05-22/samsung-says-new-7-nanometer-chip-production-starting-this-year

[5] Intel Supports American Innovation with $7 Billion Investment in Next-Generation Semiconductor Factory in Arizona, Intel Newsroom. https://newsroom.intel.com/news-releases/intel-supports-american-innovation-7-billion-investment-next-generation-semiconductor-factory-arizona/

[6] R. Zafar, Apple's A12X Has 10 Billion Transistors, 90% Speed Boost & 7-Core GPU, Wccftech. (2018). https://wccftech.com/apple-a12x-10-billion-transistors-performance/

[7] G. Roy, A.R. Brown, F. Adamu-Lema, S. Roy, A. Asenov, Simulation Study of Individual and Combined Sources of Intrinsic Parameter Fluctuations in Conventional Nano-MOSFETs, IEEE Trans. Electron Devices. 53 (2006) 3063–3070. doi:10.1109/TED.2006.885683.

[8] "There's Plenty of Room at the Bottom" (Richard Feynman, Pasadena, 29 December 1959) — Metamodern. http://metamodern.com/2009/12/29/theres-plenty-of-room-at-the-bottom%E2%80%9D-feynman-1959/

[9] M. El Kurdi, G. Fishman, S. Sauvage, P. Boucaud, Band structure and optical gain of tensile-strained germanium based on a 30 band k·p formalism, J. Appl. Phys. 107 (2010) 013710. doi:10.1063/1.3279307.

[10] R. Camacho-Aguilera, Z. Han, Y. Cai, L.C. Kimerling, J. Michel, Direct band gap narrowing in highly doped Ge, Appl. Phys. Lett. 102 (2013) 152106. doi:10.1063/1.4802199.

[11] P.S. Menon, S.K. Tasirin, I. Ahmad, S.F. Abdullah, High performance of a SOI-based lateral PIN photodiode using SiGe/Si multilayer quantum well, in: 2012 10th IEEE Int. Conf. Semicond. Electron. ICSE, 2012: pp. 403–406. doi:10.1109/SMElec.2012.6417172.

[12] F. Vigneau, R. Mizokuchi, D.C. Zanuz, X. Huang, S. Tan, R. Maurand, S. Frolov, A. Sammak, G. Scappucci, F. Lefloch, S. De Franceschi, Germanium Quantum-Well Josephson Field-Effect Transistors and Interferometers, Nano Lett. 19 (2019) 1023–1027. doi:10.1021/acs.nanolett.8b04275.

[13] K. El hajraoui, M.A. Luong, E. Robin, F. Brunbauer, C. Zeiner, A. Lugstein, P. Gentile, J.-L. Rouvière, M. Den Hertog, In Situ Transmission Electron Microscopy Analysis of Aluminum–Germanium Nanowire Solid-State Reaction, Nano Lett. 19 (2019) 2897–2904. doi:10.1021/acs.nanolett.8b05171.

[14] A. G., Design of High Quantum Efficiency and High Resolution, Si/SiGe Avalanche Photodiode Focal Plane Arrays Using Novel, Back-Illuminated, Silicon-on-Sapphire Substrates, in: J.W. Park (Ed.), Photodiodes - World Act. 2011, InTech, 2011. doi:10.5772/18516.

[15] M. Sistani, P. Staudinger, J. Greil, M. Holzbauer, H. Detz, E. Bertagnolli, A. Lugstein, Room-Temperature Quantum Ballistic Transport in Monolithic Ultrascaled Al–Ge–Al Nanowire Heterostructures, Nano Lett. 17 (2017) 4556–4561. doi:10.1021/acs.nanolett.7b00425.

[16] P. Staudinger, M. Sistani, J. Greil, E. Bertagnolli, A. Lugstein, Ultrascaled Germanium Nanowires for Highly Sensitive Photodetection at the Quantum Ballistic Limit, Nano Lett. 18 (2018) 5030–5035. doi:10.1021/acs.nanolett.8b01845.

[17] P. Gorai, Y.V. Kondratenko, E.G. Seebauer, Mechanism and kinetics of near-surface dopant pile-up during post-implant annealing, J. Appl. Phys. 111 (2012) 094510. doi:10.1063/1.4714556.

[18] G.J. van Gurp, Diffusion-limited Si precipitation in evaporated Al/Si films, J. Appl. Phys. 44 (1973) 2040–2050. doi:10.1063/1.1662511.

[19] A. Thürer, G. Rummel, Th. Zumkley, K. Freitag, H. Mehrer, Temperature and pressure dependence of Ge diffusion in aluminium, Phys. Status Solidi A. 149 (1995) 535–547. doi:10.1002/pssa.2211490204.

[20] H. Song, A. Hellawell, Solidification in the system Al-Ge-Si: The phase diagram, coring patterns, eutectic growth, and modification, Metall. Trans. A. 21 (1990) 733–740. doi:10.1007/BF02671944.

[21] Aluminum-Silicon Alloys. http://www.totalmateria.com/Article80.htm

[22] Wildfire Nano-Chip. DENSsolutions. https://DENSsolutions.com/products/wildfire/nano-chip/

[23] M. Mongillo, P. Spathis, G. Katsaros, P. Gentile, M. Sanquer, S. De Franceschi, Joule-Assisted Silicidation for Short-Channel Silicon Nanowire Devices, ACS Nano. 5 (2011) 7117–7123. doi:10.1021/nn202524j.

[24] A. Paul, T. Laurila, V. Vuorinen, S.V. Divinski, Fick's Laws of Diffusion, in: Thermodyn. Diffus. Kirkendall Eff. Solids, Springer International Publishing, Cham, 2014: pp. 115–139. doi:10.1007/978-3-319-07461-0_3.

[25] S. Arrhenius, Über die Dissociationswärme und den Einfluss der Temperatur auf den Dissociationsgrad der Elektrolyte, Z. Für Phys. Chem. 4U (1889). doi:10.1515/zpch-1889-0408.

[26] Y.-T. Wu, C.-W. Huang, C.-H. Chiu, C.-F. Chang, J.-Y. Chen, T.-Y. Lin, Y.-T. Huang, K.-C. Lu, P.-H. Yeh, W.-W. Wu, Nickel/Platinum Dual Silicide Axial Nanowire Heterostructures with Excellent Photosensor Applications, Nano Lett. 16 (2016) 1086–1091. doi:10.1021/acs.nanolett.5b04309.

[27] Y.-C. Lin, K.-C. Lu, W.-W. Wu, J. Bai, L.J. Chen, K.N. Tu, Y. Huang, Single Crystalline PtSi Nanowires, PtSi/Si/PtSi Nanowire Heterostructures, and Nanodevices, Nano Lett. 8 (2008) 913–918. doi:10.1021/nl073279r.

[28] J. Tang, C.-Y. Wang, F. Xiu, Y. Zhou, L.-J. Chen, K.L. Wang, Formation and Device Application of Ge Nanowire Heterostructures via Rapid Thermal Annealing, Adv. Mater. Sci. Eng. 2011 (2011) 1–16. doi:10.1155/2011/316513.

[29] K. Ogata, E. Sutter, X. Zhu, S. Hofmann, Ni-silicide growth kinetics in Si and Si/SiO_2 core/shell nanowires, Nanotechnology. 22 (2011) 365305. doi:10.1088/0957-4484/22/36/365305.

[30] K.-C. Lu, W.-W. Wu, H. Ouyang, Y.-C. Lin, Y. Huang, C.-W. Wang, Z.-W. Wu, C.-W. Huang, L.J. Chen, K.N. Tu, The Influence of Surface Oxide on the Growth of Metal/Semiconductor Nanowires, Nano Lett. 11 (2011) 2753–2758. doi:10.1021/nl201037m.

[31] K.E. Hajraoui, In-situ transmission electron microscopy studies of metal-Ge nanowire solid-state reactions, (2017). https://tel.archives-ouvertes.fr/tel-01645553

[32] C.-H. Chiu, C.-W. Huang, J.-Y. Chen, Y.-T. Huang, J.-C. Hu, L.-T. Chen, C.-L. Hsin, W.-W. Wu, Copper silicide/silicon nanowire heterostructures: in situ TEM observation of growth behaviors and electron transport properties, Nanoscale. 5 (2013) 5086. doi:10.1039/c3nr33302g.

[33] K. Seo, N. Bagkar, S. Kim, J. In, H. Yoon, Y. Jo, B. Kim, Diffusion-Driven Crystal Structure Transformation: Synthesis of Heusler Alloy Fe_3Si Nanowires, Nano Lett. 10 (2010) 3643–3647. doi:10.1021/nl102093e.

[34] J. Tang, C.-Y. Wang, L.-T. Chang, Y. Fan, T. Nie, M. Chan, W. Jiang, Y.-T. Chen, H.-J. Yang, H.-Y. Tuan, L.-J. Chen, K.L. Wang, Electrical Spin Injection and Detection in Mn_5Ge_3/Ge/Mn_5Ge_3 Nanowire Transistors, Nano Lett. 13 (2013) 4036–4043. doi:10.1021/nl401238p.

[35] Y.-C. Chou, W.-W. Wu, L.-J. Chen, K.-N. Tu, Homogeneous Nucleation of Epitaxial $CoSi_2$ and NiSi in Si Nanowires, Nano Lett. 9 (2009) 2337–2342. doi:10.1021/nl900779j.

[36] B. Xiang, Q.X. Wang, Z. Wang, X.Z. Zhang, L.Q. Liu, J. Xu, D.P. Yu, Synthesis and field emission properties of TiSi2 nanowires, Appl. Phys. Lett. 86 (2005) 243103. doi:10.1063/1.1948515.

[37] F. Zhou, J. Szczech, M.T. Pettes, A.L. Moore, S. Jin, L. Shi, Determination of Transport Properties in Chromium Disilicide Nanowires via Combined Thermoelectric and Structural Characterizations, Nano Lett. 7 (2007) 1649–1654. doi:10.1021/nl0706143.

[38] A. Katsman, Y. Yaish, E. Rabkin, M. Beregovsky, Surface Diffusion Controlled Formation of Nickel Silicides in Silicon Nanowires, J. Electron. Mater. 39 (2010) 365–370. doi:10.1007/s11664-009-1071-1.

[39] Y.E. Yaish, A. Katsman, G.M. Cohen, M. Beregovsky, Kinetics of nickel silicide growth in silicon nanowires: From linear to square root growth, J. Appl. Phys. 109 (2011) 094303. doi:10.1063/1.3574650.

[40] C. Perrin, D. Mangelinck, F. Nemouchi, J. Labar, C. Lavoie, C. Bergman, P. Gas, Nickel silicides and germanides: Phases formation, kinetics and thermal expansion, Mater. Sci. Eng. B. 154–155 (2008) 163–167. doi:10.1016/j.mseb.2008.09.042.

[41] N.S. Dellas, S. Minassian, J.M. Redwing, S.E. Mohney, Formation of nickel germanide contacts to Ge nanowires, Appl. Phys. Lett. 97 (2010) 263116. doi:10.1063/1.3533808.

[42] Y.-C. Lin, Y. Chen, A. Shailos, Y. Huang, Detection of Spin Polarized Carrier in Silicon Nanowire with Single Crystal MnSi as Magnetic Contacts, Nano Lett. 10 (2010) 2281–2287. doi:10.1021/nl101477q.

[43] K. Ogata, E. Sutter, X. Zhu, S. Hofmann, Ni-silicide growth kinetics in Si and Si/SiO_2 core/shell nanowires, Nanotechnology. 22 (2011) 365305. doi:10.1088/0957-4484/22/36/365305.

[44] S. Kral, C. Zeiner, M. Stöger-Pollach, E. Bertagnolli, M.I. Den Hertog, M. Lopez-Haro, E. Robin, K. El Hajraoui, A. Lugstein, Abrupt Schottky Junctions in Al/Ge Nanowire Heterostructures, Nano Lett. 15 (2015) 4783–4787. doi:10.1021/acs.nanolett.5b01748.

[45] H. Ibach, H. Lüth, Solid-State Physics, Springer Berlin Heidelberg, Berlin, Heidelberg, 2009. doi:10.1007/978-3-540-93804-0.

[46] O. Monfort, G. Plesch, Bismuth vanadate-based semiconductor photocatalysts: a short critical review on the efficiency and the mechanism of photodegradation of organic pollutants, Environ. Sci. Pollut. Res. 25 (2018) 19362–19379. doi:10.1007/s11356-018-2437-9.

[47] J. Hölzl, F.K. Schulte, Work function of metals, in: J. Hölzl, F.K. Schulte, H. Wagner (Eds.), Solid Surf. Phys., Springer Berlin Heidelberg, Berlin, Heidelberg, 1979: pp. 1–150. doi:10.1007/BFb0048919.

[48] M. Nič, J. Jirát, B. Košata, A. Jenkins, A. McNaught, eds., electron affinity, Eea, in: IUPAC Compend. Chem. Terminol., 2.1.0, IUPAC, Research Triagle Park, NC, 2009. doi:10.1351/goldbook.E01977.

[49] Prof. Jasprit Singh's Web Page. http://www.eecs.umich.edu/courses/eecs320/

[50] D.D.D. Ma, Small-Diameter Silicon Nanowire Surfaces, Science. 299 (2003) 1874–1877. doi:10.1126/science.1080313.

[51] C.M. Natarajan, M.G. Tanner, R.H. Hadfield, Superconducting nanowire single-photon detectors: physics and applications, Supercond. Sci. Technol. 25 (2012) 063001. doi:10.1088/0953-2048/25/6/063001.

[52] J. Jiu, K. Suganuma, Metallic Nanowires and Their Application, IEEE Trans. Compon. Packag. Manuf. Technol. 6 (2016) 1733–1751. doi:10.1109/TCPMT.2016.2581829.

[53] H. Zhu, Semiconductor Nanowire MOSFETs and Applications, in: K. Maaz (Ed.), Nanowires - New Insights, InTech, 2017. doi:10.5772/67446.

[54] C. Ouyang, K. Hashimoto, H. Tsuji, E. Nakamura, Y. Majima, Coherent Resonant Electron Tunneling at 9 and 300 K through a 4.5 nm Long, Rigid, Planar Organic Molecular Wire, ACS Omega. 3 (2018) 5125–5130. doi:10.1021/acsomega.8b00559.

[55] S.D. Dabhi, P.K. Jha, Ab initio study of strained wurtzite InAs nanowires: engineering an indirect–direct band gap transition through size and uniaxial strain, RSC Adv. 5 (2015) 89993–90000. doi:10.1039/C5RA16512A.

[56] R. Könenkamp, R.C. Word, C. Schlegel, Vertical nanowire light-emitting diode, Appl. Phys. Lett. 85 (2004) 6004–6006. doi:10.1063/1.1836873.

[57] H. Kang, J. Park, T. Choi, H. Jung, K.H. Lee, S. Im, H. Kim, n-ZnO:N/p-Si nanowire photodiode prepared by atomic layer deposition, Appl. Phys. Lett. 100 (2012) 041117. doi:10.1063/1.3679078.

[58] R. Röder, C. Ronning, Review on the dynamics of semiconductor nanowire lasers, Semicond. Sci. Technol. 33 (2018) 033001. doi:10.1088/1361-6641/aaa7be.

[59] N.P. Dasgupta, P. Yang, Semiconductor nanowires for photovoltaic and photoelectrochemical energy conversion, Front. Phys. 9 (2014) 289–302. doi:10.1007/s11467-013-0305-0.

[60] S.L. Tan, X. Zhao, K. Chen, K.B. Crozier, Y. Dan, High-performance silicon nanowire bipolar phototransistors, Appl. Phys. Lett. 109 (2016) 033505. doi:10.1063/1.4959264.

[61] E. Barrigón, O. Hultin, D. Lindgren, F. Yadegari, M.H. Magnusson, L. Samuelson, L.I.M. Johansson, M.T. Björk, GaAs Nanowire pn-Junctions Produced by Low-Cost and High-Throughput Aerotaxy, Nano Lett. 18 (2018) 1088–1092. doi:10.1021/acs.nanolett.7b04609.

[62] R.S. Wagner, W.C. Ellis, Vapor-Liquid-Solid Mechanism of Single Crystal Growth, Appl. Phys. Lett. 4 (1964) 89–90. doi:10.1063/1.1753975.

[63] L.C. Campos, M. Tonezzer, A.S. Ferlauto, V. Grillo, R. Magalhães-Paniago, S. Oliveira, L.O. Ladeira, R.G. Lacerda, Vapor–Solid–Solid Growth Mechanism Driven by Epitaxial Match between Solid AuZn Alloy Catalyst Particles and ZnO Nanowires at Low Temperatures, Adv. Mater. 20 (2008) 1499–1504. doi:10.1002/adma.200701612.

[64] M. Friedl, K. Cerveny, P. Weigele, G. Tütüncüoglu, S. Martí-Sánchez, C. Huang, T. Patlatiuk, H. Potts, Z. Sun, M.O. Hill, L. Güniat, W. Kim, M. Zamani, V.G. Dubrovskii, J. Arbiol, L.J. Lauhon, D.M. Zumbühl, A. Fontcuberta i Morral, Template-Assisted Scalable Nanowire Networks, Nano Lett. 18 (2018) 2666–2671. doi:10.1021/acs.nanolett.8b00554.

[65] B. Ressel, K.C. Prince, S. Heun, Y. Homma, Wetting of Si surfaces by Au–Si liquid alloys, J. Appl. Phys. 93 (2003) 3886–3892. doi:10.1063/1.1558996.

[66] P. Gentile, A. Solanki, N. Pauc, F. Oehler, B. Salem, G. Rosaz, T. Baron, M. Den Hertog, V. Calvo, Effect of HCl on the doping and shape control of silicon nanowires, Nanotechnology. 23 (2012) 215702. doi:10.1088/0957-4484/23/21/215702.

[67] F.S. Minaye Hashemi, S. Thombare, A.F. i Morral, M.L. Brongersma, P.C. McIntyre, Effects of surface oxide formation on germanium nanowire band-edge photoluminescence, Appl. Phys. Lett. 102 (2013) 251122. doi:10.1063/1.4812334.

[68] D.E. Perea, E.R. Hemesath, E.J. Schwalbach, J.L. Lensch-Falk, P.W. Voorhees, L.J. Lauhon, Direct measurement of dopant distribution in an individual vapour–liquid–solid nanowire, Nat. Nanotechnol. 4 (2009) 315–319. doi:10.1038/nnano.2009.51.

[69] K. Guilloy, N. Pauc, A. Gassenq, P. Gentile, S. Tardif, F. Rieutord, V. Calvo, Tensile Strained Germanium Nanowires Measured by Photocurrent Spectroscopy and X-ray Microdiffraction, Nano Lett. 15 (2015) 2429–2433. doi:10.1021/nl5048219.

[70] Hydrogen peroxide solution H1009, Sigma-Aldrich. https://www.sigmaaldrich.com/catalog/product/sigma/h1009

[71] B. Onsia, T. Conard, S. De Gendt, M.M. Heyns, I. Hoflijk, P.W. Mertens, M. Meuris, G. Raskin, S. Sioncke, I. Teerlinck, A. Theuwis, J. Van Steenbergen, C. Vinckier, A Study of the Influence of Typical Wet Chemical Treatments on the Germanium Wafer Surface, Solid State Phenom. 103–104 (2005) 27–30. doi:10.4028/www.scientific.net/SSP.103-104.27.

[72] Hydriodic acid, HI. https://www.sigmaaldrich.com/catalog/product/sigald/210021

[73] J. Maula, Atomic layer deposition (ALD) for optical nanofabrication, in: W.V. Schoenfeld, J.J. Wang, M. Loncar, T.J. Suleski (Eds.), San Francisco, California, 2010: p. 75910S. doi:10.1117/12.841343.

[74] M. Putkonen, P. Sippola, L. Svärd, T. Sajavaara, J. Vartiainen, I. Buchanan, U. Forsström, P. Simell, T. Tammelin, Low-temperature atomic layer deposition of SiO_2 /Al_2O_3 multilayer structures constructed on self-standing films of cellulose nanofibrils, Philos. Trans. R. Soc. Math. Phys. Eng. Sci. 376 (2018) 20170037. doi:10.1098/rsta.2017.0037.

[75] R. Clark, Emerging Applications for High K Materials in VLSI Technology, Materials. 7 (2014) 2913–2944. doi:10.3390/ma7042913.

[76] M.I. Den Hertog, F. González-Posada, R. Songmuang, J.L. Rouviere, T. Fournier, B. Fernandez, E. Monroy, Correlation of Polarity and Crystal Structure with Optoelectronic and Transport Properties of GaN/AlN/GaN Nanowire Sensors, Nano Lett. 12 (2012) 5691–5696. doi:10.1021/nl302890f.

[77] M. den Hertog, F. Donatini, R. McLeod, E. Monroy, C. Sartel, V. Sallet, J. Pernot, *In situ* biasing and off-axis electron holography of a ZnO nanowire, Nanotechnology. 29 (2018) 025710. doi:10.1088/1361-6528/aa923c.

[78] KLayout Layout Viewer And Editor. https://www.klayout.de/staging/gallery.html

[79] P. Stevic, BOE / HF – Silicon dioxide Etching Standard Operating Procedure. https://d1rkab7tlqy5f1.cloudfront.net/TNW/Afdelingen/Quantum%20Nanoscience/Kavli%20Nanolab%20Delft/Equipment/BOE-HF%20SOP%20Silicon%20Etching.pdf.

[80] Buffered Oxide Etch, Etching Mixtures. https://www.microchemicals.com/products/etching_mixtures/boe_buffered_hf.html

[81] Y. Wang, L. Zhou, B. Jia, D. Bai, X. Yang, X. Gao, B. Bo, The effect of argon plasma cleaning on the surface characteristics of GaAs substrate, in: 2012 Int. Conf. Optoelectron. Microelectron., IEEE, Changchun, Jilin, China, 2012: pp. 16–20. doi:10.1109/ICoOM.2012.6316205.

[82] P.J. Kelly, R.D. Arnell, Magnetron sputtering: a review of recent developments and applications, Vacuum. 56 (2000) 159–172. doi:10.1016/S0042-207X(99)00189-X.

[83] K. Wasa, M. Kitabatake, H. Adachi, Deposition of Compound Thin Films, in: Thin Film Mater. Technol., Elsevier, 2004: pp. 191–403. doi:10.1016/B978-081551483-1.50006-X.

[84] Application of Rapid Thermal Annealing Systems | Allwin21 Corp. https://allwin21.com/semiconductor-process-equipment/application-of-rapid-thermal-annealing-systems/

[85] Jipelec™ Jetfirst: Compact & Robust RTP Furnace. http://www.ecm-usa.com/products/rtp-furnaces/jetfirst

[86] R.L. Steere, Electron Microscopy of Structural Detail In Frozen Biological Specimens, J. Cell Biol. 3 (1957) 45–60. doi:10.1083/jcb.3.1.45.

[87] Dr Saurabh Bhargava, Scanning Electron Microscopy (SEM) lecture. https://www.slideshare.net/drbhargava5745/scanning-electron-microscopy-sem-lecture

[88] H. Busch, Berechnung der Bahn von Kathodenstrahlen im axialsymmetrischen elektromagnetischen Felde, Ann. Phys. 386 (1926) 974–993. doi:10.1002/andp.19263862507.

[89] E. Ruska, The Development of the Electron Microscope and of Electron Microscopy(Nobel Lecture), Angew. Chem. Int. Ed. Engl. 26 (1987) 595–605. doi:10.1002/anie.198705953.

[90] H.G. Rudenberg, P.G. Rudenberg, Origin and Background of the Invention of the Electron Microscope, in: Adv. Imaging Electron Phys., Elsevier, 2010: pp. 207–286. doi:10.1016/S1076-5670(10)60006-7.

[91] A.D.G. Stewart, The origins and development of scanning electron microscopy, J. Microsc. 139 (1985) 121–127. doi:10.1111/j.1365-2818.1985.tb02629.x.

[92] The Influence of Laser Biotechnology on Energetic Value and Chemical Parameters of Rose Multiflora Biomass and Role of Catalysts for bio-energy production from Biomass: Case Study in Krakow-Poland. https://www.researchgate.net/publication/279955847_The_Influence_of_Laser_Biotechnology_on_Energetic_Value_and_Chemical_Parameters_of_Rose_Multiflora_Biomass_and_Role_of_Catalysts_for_bio-energy_production_from_Biomass_Case_Study_in_Krakow-Poland

[93] D.B. Williams, C.B. Carter, Transmission Electron Microscopy, Springer US, Boston, MA, 2009. doi:10.1007/978-0-387-76501-3.

[94] Gringer, Diagram outlining the internal components of a basic TEM system, 2009. https://commons.wikimedia.org/wiki/File:Scheme_TEM_en.svg

[95] Looking through the fish-eye the Electron Ronchigram. Duncan T.L. Alexander CIME seminar May 24, PDF. https://docplayer.net/21479966-Looking-through-the-fish-eye-the-electron-ronchigram-duncan-t-l-alexander-cime-seminar-may-24-2012.html

[96] S. Kondo, K. Ogasawara, K. Hinode, Thermographic analysis of electromigration phenomena in aluminum metallization, J. Appl. Phys. 79 (1996) 736. doi:10.1063/1.360819.

[97] M.J. Hÿtch, E. Snoeck, R. Kilaas, Quantitative measurement of displacement and strain fields from HREM micrographs, Ultramicroscopy. 74 (1998) 131–146. doi:10.1016/S0304-3991(98)00035-7.

[98] J.L. Rouvière, E. Sarigiannidou, Theoretical discussions on the geometrical phase analysis, Ultramicroscopy. 106 (2005) 1–17. doi:10.1016/j.ultramic.2005.06.001.

[99] E.B. Podgoršak, Rutherford–Bohr Model of the Atom, in: Radiat. Phys. Med. Phys., Springer International Publishing, Cham, 2016: pp. 143–180. doi:10.1007/978-3-319-25382-4_3.

[100] The Bohr Model of the Atom. https://slideplayer.com/slide/8933879/

[101] R. Castaing, Application des sondes electroniques a une methode d'analyse ponctuelle chimique et cristallographique, 1951. https://www.worldcat.org/title/application-of-electron-probes-to-local-chemical-and-crystallographic-analysis/oclc/437050734?referer=di&ht=edition

[102] R. Monte Albee, John Armstrong, Goldstein, Philibert, Ziebold, Ogilvie, Castaing, McMorrow, Quantitative Analysis: Intensities to Concentrations. https://slideplayer.com/slide/5086602/

[103] A. Boekestein, A.M. Stadhouders, A.L.H. Stols, G.M. Roomans, A comparison of ZAF-correction methods in quantitative X-ray microanalysis of light-element specimens, Ultramicroscopy. 12 (1983) 65–68. doi:10.1016/0304-3991(83)90306-6.

[104] A. Parisini, S. Frabboni, G.C. Gazzadi, R. Rosa, A. Armigliato, Comparison of Cliff–Lorimer-Based Methods of Scanning Transmission Electron Microscopy (STEM) Quantitative X-Ray Microanalysis for

Application to Silicon Oxycarbides Thin Films, Microsc. Microanal. 24 (2018) 193–206. doi:10.1017/S1431927618000259.

[105] M. Watanabe, D.B. Williams, The quantitative analysis of thin specimens: a review of progress from the Cliff-Lorimer to the new zeta-factor methods, J. Microsc. 221 (2006) 89–109. doi:10.1111/j.1365-2818.2006.01549.x.

[106] P. Rueda-Fonseca, E. Robin, E. Bellet-Amalric, M. Lopez-Haro, M. Den Hertog, Y. Genuist, R. André, A. Artioli, S. Tatarenko, D. Ferrand, J. Cibert, Quantitative Reconstructions of 3D Chemical Nanostructures in Nanowires, Nano Lett. 16 (2016) 1637–1642. doi:10.1021/acs.nanolett.5b04489.

[107] T. Burchhart, A. Lugstein, Y.J. Hyun, G. Hochleitner, E. Bertagnolli, Atomic Scale Alignment of Copper-Germanide Contacts for Ge Nanowire Metal Oxide Field Effect Transistors, Nano Lett. 9 (2009) 3739–3742. doi:10.1021/nl9019243.

[108] S.-I. Fujikawa, Y.-I. Izeki, Measurement of solid solubility of germanium in aluminum, Metall. Trans. A. 24 (1993) 277–282. doi:10.1007/BF02657314.

[109] K. Chattopadhyay, X.-M. Wang, K. Aoki, T. Masumoto, Metastable phase formation during mechanical alloying of Al/Ge and Al/Si alloys, J. Alloys Compd. 232 (1996) 224–231. doi:10.1016/0925-8388(95)02002-0.

[110] H.-M. Kagaya, K. Imazawa, M. Sato, Toshinobu Soma, Phase diagrams of Al–Si and Al–Ge systems, Phys. B Condens. Matter. 245 (1998) 252–255. doi:10.1016/S0921-4526(97)00677-7.

[111] F.M. Brunbauer, E. Bertagnolli, J. Majer, A. Lugstein, Electrical transport properties of single-crystal Al nanowires, Nanotechnology. 27 (2016) 385704. doi:10.1088/0957-4484/27/38/385704.

[112] M. Wittmer, K.N. Tu, Low-temperature diffusion of dopant atoms in silicon during interfacial silicide formation, Phys. Rev. B. 29 (1984) 2010–2020. doi:10.1103/PhysRevB.29.2010.

[113] J.J. Loferski, P. Rappaport, Radiation Damage in Ge and Si Detected by Carrier Lifetime Changes: Damage Thresholds, Phys. Rev. 111 (1958) 432–439. doi:10.1103/PhysRev.111.432.

[114] V.T. Fauske, J. Huh, G. Divitini, D.L. Dheeraj, A.M. Munshi, C. Ducati, H. Weman, B.-O. Fimland, A.T.J. van Helvoort, In Situ Heat-Induced Replacement of GaAs Nanowires by Au, Nano Lett. 16 (2016) 3051–3057. doi:10.1021/acs.nanolett.6b00109.

[115] V.C. Holmberg, K.A. Collier, B.A. Korgel, Real-Time Observation of Impurity Diffusion in Silicon Nanowires, Nano Lett. 11 (2011) 3803–3808. doi:10.1021/nl201879u.

[116] P.W. Loscutoff, S.F. Bent, Reactivity of The Germanium Surface: Chemical Passivation and Functionalization, Annu. Rev. Phys. Chem. 57 (2006) 467–495. doi:10.1146/annurev.physchem.56.092503.141307.

[117] BENNING MM P3 - BENNING. https://www.benning.de/products-en/testing-measuring-and-safety-equipment/digital-multimeter/benning-mm-p3.html

[118] TLM_measurements.pdf. http://tuttle.merc.iastate.edu/ee432/topics/metals/tlm_measurements.pdf

[119] N. Duan, J. Luo, G. Wang, J. Liu, E. Simoen, S. Mao, H. Radamson, X. Wang, J. Li, W. Wang, C. Zhao, T. Ye, Reduction of NiGe/n- and p-Ge Specific Contact Resistivity by Enhanced Dopant Segregation in the Presence of Carbon During Nickel Germanidation, IEEE Trans. Electron Devices. 63 (2016) 4546–4549. doi:10.1109/TED.2016.2610461.

[120] L. Yang, J.R. Watling, R.C.W. Wilkins, M. Boriçi, J.R. Barker, A. Asenov, S. Roy, Si/SiGe heterostructure parameters for device simulations, Semicond. Sci. Technol. 19 (2004) 1174–1182. doi:10.1088/0268-1242/19/10/002.

[121] K. Majumder, N.R. Das, Effects of alloy composition on gain and bandwidth of Si/SiGe and Si/GeSn avalanche photodiodes, Optik. 127 (2016) 3059–3064. doi:10.1016/j.ijleo.2015.11.174.

[122] J.W. Zeller, Y.R. Puri, A.K. Sood, S. McMahon, H. Efsthadiatis, P. Haldar, N.K. Dhar, Design and development of SiGe based near-infrared photodetectors, in: P.D. LeVan, A.K. Sood, P. Wijewarnasuriya, A.I. D'Souza (Eds.), San Diego, California, United States, 2014: p. 922006. doi:10.1117/12.2083538.

[123] B. Bindu, N. DasGupta, A. DasGupta, Analytical model of drain current of Si/SiGe heterostructure p-channel MOSFETs for circuit simulation, IEEE Trans. Electron Devices. 53 (2006) 1411–1419. doi:10.1109/TED.2006.874242.

[124] J.-Y. Wei, S. Maikap, M.H. Lee, C.C. Lee, C.W. Liu, Hole confinement at Si/SiGe heterojunction of strained-Si N and PMOS devices, Solid-State Electron. 50 (2006) 109–113. doi:10.1016/j.sse.2005.10.032.

[125] G. Isella, D. Chrastina, B. Rössner, T. Hackbarth, H.-J. Herzog, U. König, H. von Känel, Low-energy plasma-enhanced chemical vapor deposition for strained Si and Ge heterostructures and devices, Solid-State Electron. 48 (2004) 1317–1323. doi:10.1016/j.sse.2004.01.013.

[126] T. Hackbarth, H.-J. Herzog, M. Zeuner, G. Höck, E.A. Fitzgerald, M. Bulsara, C. Rosenblad, H. von Känel, Alternatives to thick MBE-grown relaxed SiGe buffers, Thin Solid Films. 369 (2000) 148–151. doi:10.1016/S0040-6090(00)00795-1.

[127] G.K. Sigworth, Fundamentals of Solidification in Aluminum Castings, Int. J. Met. 8 (2014) 7–20. doi:10.1007/BF03355567.

[128] A. Mostafa, M. Medraj, Binary Phase Diagrams and Thermodynamic Properties of Silicon and Essential Doping Elements (Al, As, B, Bi, Ga, In, N, P, Sb and Tl), Materials. 10 (2017) 676. doi:10.3390/ma10060676.

[129] Z. Liu, M. Wang, Y. Weng, T. Song, Y. Huo, J. Xie, Effect of Silicon on Grain Refinement of Aluminum Produced by Electrolysis, Mater. Trans. 44 (2003) 2157–2162. doi:10.2320/matertrans.44.2157.

[130] R.-G. Guan, D. Tie, A Review on Grain Refinement of Aluminum Alloys: Progresses, Challenges and Prospects, Acta Metall. Sin. Engl. Lett. 30 (2017) 409–432. doi:10.1007/s40195-017-0565-8.

[131] W.S. Miller, L. Zhuang, J. Bottema, A.J. Wittebrood, P. De Smet, A. Haszler, A. Vieregge, Recent development in aluminium alloys for the automotive industry, Mater. Sci. Eng. A. 280 (2000) 37–49. doi:10.1016/S0921-5093(99)00653-X.

[132] G.F. Vander Voort, ed., Solidification Structures of Aluminum Alloys, in: Metallogr. Microstruct. ASM International, 2004: pp. 107–115. doi:10.31399/asm.hb.v09.a0003727.

[133] S. Fujikawa, K. Hirano, Y. Fukushima, Diffusion of silicon in aluminum, Metall. Trans. A. 9 (1978) 1811–1815. doi:10.1007/BF02663412.

[134] E.N. Mgbenu, Accelerated aging of Al/Ge and Al/Si thin film couples, Thin Solid Films. 65 (1980) 267–274. doi:10.1016/0040-6090(80)90236-9.

[135] Diffusion in Silicon.pdf. https://pdfs.semanticscholar.org/3aaf/2274fbae9bb01aebc94faec63100f8d30e60.pdf

[136] P. Rueda-Fonseca, E. Robin, E. Bellet-Amalric, M. Lopez-Haro, M. Den Hertog, Y. Genuist, R. André, A. Artioli, S. Tatarenko, D. Ferrand, J. Cibert, Quantitative Reconstructions of 3D Chemical Nanostructures in Nanowires, Nano Lett. 16 (2016) 1637–1642. doi:10.1021/acs.nanolett.5b04489.

[137] M. Sistani, M.A. Luong, M.I. den Hertog, E. Robin, M. Spies, B. Fernandez, J. Yao, E. Bertagnolli, A. Lugstein, Monolithic Axial and Radial Metal–Semiconductor Nanowire Heterostructures, Nano Lett. 18 (2018) 7692–7697. doi:10.1021/acs.nanolett.8b03366.

[138] W. Lu, J. Xiang, B.P. Timko, Y. Wu, C.M. Lieber, One-dimensional hole gas in germanium/silicon nanowire heterostructures, Proc. Natl. Acad. Sci. 102 (2005) 10046–10051. doi:10.1073/pnas.0504581102.

[139] S. Gazibegovic, D. Car, H. Zhang, S.C. Balk, J.A. Logan, M.W.A. de Moor, M.C. Cassidy, R. Schmits, D. Xu, G. Wang, P. Krogstrup, R.L.M. Op het Veld, K. Zuo, Y. Vos, J. Shen, D. Bouman, B. Shojaei, D. Pennachio, J.S. Lee, P.J. van Veldhoven, S. Koelling, M.A. Verheijen, L.P. Kouwenhoven, C.J. Palmstrom, E.P.A.M. Bakkers, Epitaxy of advanced nanowire quantum devices, Nature. 548 (2017) 434–438. doi:10.1038/nature23468.

[140] M.W.A. de Moor, J.D.S. Bommer, D. Xu, G.W. Winkler, A.E. Antipov, A. Bargerbos, G. Wang, N. van Loo, R.L.M. Op het Veld, S. Gazibegovic, D. Car, J.A. Logan, M. Pendharkar, J.S. Lee, E.P.A. M Bakkers, C.J. Palmstrøm, R.M. Lutchyn, L.P. Kouwenhoven, H. Zhang, Electric field tunable superconductor-semiconductor coupling in Majorana nanowires, New J. Phys. 20 (2018) 103049. doi:10.1088/1367-2630/aae61d.

[141] K. Schäfer, C. Synowietz, D'Ans-Lax Taschenbuch für Chemiker und Physiker, Springer Berlin Heidelberg, Berlin, Heidelberg, 1998. doi:10.1007/978-3-662-01008-2.

[142] E.R. Jette, F. Foote, Precision Determination of Lattice Constants, J. Chem. Phys. 3 (1935) 605–616. doi:10.1063/1.1749562.

[143] L.J. Lauhon, M.S. Gudiksen, D. Wang, C.M. Lieber, Epitaxial core–shell and core–multishell nanowire heterostructures, Nature. 420 (2002) 57–61. doi:10.1038/nature01141.

Résumé

Les nanofils semi-conducteurs suscitent un intérêt croissant en raison de leur potentiel pour de nouvelles applications dans les transistors à effet de champ, les photodétecteurs et les biocapteurs. En particulier, la géométrie des nanofils offre la possibilité de fabriquer des hétérostructures axiales auxquelles il est facile d'accéder électriquement par des contacts pris aux extrémités. Selon les dimensions et la composition des hétérostructures, les porteurs peuvent subir des effets de confinement quantique, permettant de fabriquer des boites ou des disques quantiques connectés électriquement. Ainsi, la formation de contacts en silicide ou en germanide, via une réaction à l'état solide activée thermiquement entre un métal et un nanofil de Si ou de Ge, a suscité beaucoup d'intérêt en raison de son avantage pour la fabrication de dispositifs à canal court à partir de nanofils fait par croissance 'bottom up', qui parait plus aisé et moins couteux qu'une approche par lithographie et gravure du style 'top down'. L'avantage de cette approche est que lors du chauffage, le métal pénètre dans le nanofil semi-conducteur aux deux extrémités, créant une région (inter) métallique. Si le processus est bien contrôlé et arrêté au bon moment, il ne reste qu'une mince section de semi-conducteur entre les contacts métalliques, ce qui permet de fabriquer des boites ou des disques quantiques mis en contact électriquement dans des structures filaires en une seule étape de fabrication.

La diffusion à l'état solide induite thermiquement de l'Al dans un nanofil de Ge est un système prometteur car, contrairement à d'autres combinaisons métal-semi-conducteur ou une phase intermétallique est formée, une phase monocristalline d'Al pur est créée dont l'interface avec le nanofil de Ge est nette. De plus, la combinaison du couplage spin-orbite intrinsèquement fort du Ge et les propriétés supraconductrices de l'Al font de ce système une plate-forme prometteuse pour l'étude de dispositifs semi-conducteurs hybrides supraconducteurs qui pourraient être un des éléments constitutifs potentiels des dispositifs d'interférence quantique supraconducteurs (SQUID). Le défi abordé dans cette thèse est d'étudier la réaction d'échange de l'aluminium induit thermiquement à la fois dans les nanofils pur de Ge et d'alliage Si_xGe_{1-x} en utilisant les techniques de microscopie électronique à transmission (TEM) in situ, afin de permettre une meilleure compréhension et un meilleur contrôle des mécanismes impliqués dans la réaction.

Mots-clés: nanofils, microscopie électronique à transmission in situ, réaction d'échange de l'induit thermiquement, solidification

Abstract

Semiconductor nanowires are receiving widespread interests for their novel applications in field-effect transistors, photodetectors and biosensors. The nanowire geometry provides an interesting possibility to fabricate axial heterostructures that can be easily accessed electrically by contacting the NW edges. Depending on the size, material and composition of the heterostructure, carriers can experience quantum confinement effects, allowing to fabricate quantum dots or quantum disks inside the NW. Recently, the formation of Silicide or Germanide contacts via a thermally activated solid state reaction between the metal and Si or Ge NW has drawn significant attention because of its great advantages for fabricating short channel devices from bottom up grown NWs rather than complex and high-cost photolithography top-down approaches. The advantage of this approach is that upon heating a metal enters a semiconducting NW at both ends, creating an (inter)metallic region in the NW. If the process is well controlled and stopped at the right moment, only a thin section of semiconductor is left between metallic contacts, allowing to fabricate electrically contacted quantum-dot in a wire structures in a single fabrication step.

Al/Ge NW thermal induced solid-state diffusion is a promising system since, in contrast to other metal-semiconductor combinations, no intermetallic phase is formed and a pure monocrystalline Al NW is created with a very sharp interface with the remaining Ge NW. Moreover, the combination of the intrinsically strong spin−orbit coupling in Ge and the superconducting properties of Al, make this system a promising platform to study hybrid superconductor-semiconductor devices that could be potential building blocks for superconducting quantum interference devices (SQUIDs). The challenge addressed in this PhD is to study the thermally induced exchange reaction of Al in both pure Ge as well as Si_xGe_{1-x} alloy NWs using in-situ observations in a transmission electron microscope (TEM), to allow better understanding and control of the mechanisms involved in the reaction.

Keywords: nanowires, in situ transmission electron microscopy, solid state exchange reaction, solidification